

Wave Feedforward and Multivariable Feedback Control Architectures and Design Methods for Floating Wind Turbines

Hegazy, A.R.M.

DOI

[10.4233/uuid:3b70abfc-5a48-4816-9531-d5b11b8827b8](https://doi.org/10.4233/uuid:3b70abfc-5a48-4816-9531-d5b11b8827b8)

Publication date

2025

Document Version

Final published version

Citation (APA)

Hegazy, A. R. M. (2025). *Wave Feedforward and Multivariable Feedback Control Architectures and Design Methods for Floating Wind Turbines*. [Dissertation (TU Delft), Delft University of Technology]. <https://doi.org/10.4233/uuid:3b70abfc-5a48-4816-9531-d5b11b8827b8>

Important note

To cite this publication, please use the final published version (if applicable).
Please check the document version above.

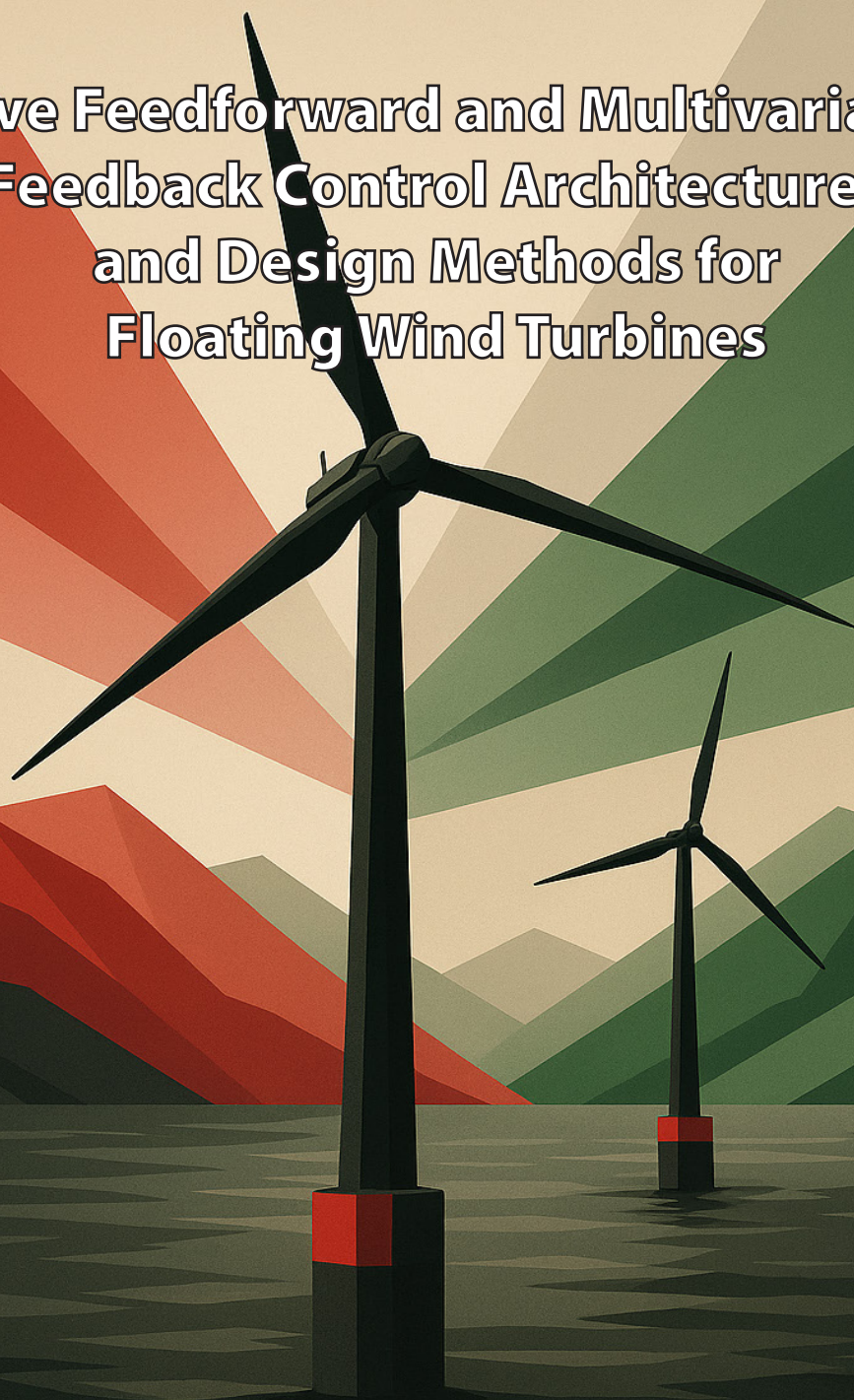
Copyright

Other than for strictly personal use, it is not permitted to download, forward or distribute the text or part of it, without the consent of the author(s) and/or copyright holder(s), unless the work is under an open content license such as Creative Commons.

Takedown policy

Please contact us and provide details if you believe this document breaches copyrights.
We will remove access to the work immediately and investigate your claim.

Wave Feedforward and Multivariable Feedback Control Architectures and Design Methods for Floating Wind Turbines



Amr Hegazy

Wave Feedforward and Multivariable Feedback Control Architectures and Design Methods for Floating Wind Turbines

Wave Feedforward and Multivariable Feedback Control Architectures and Design Methods for Floating Wind Turbines

Dissertation

for the purpose of obtaining the degree of doctor
at Delft University of Technology,
by the authority of the Rector Magnificus prof. dr. ir. T.H.J.J. van der Hagen,
chair of the Board for Doctorates,
to be defended publicly on
Wednesday, 29 October 2025 at 10:00 o'clock

by

Amr Raafat Mohamed HEGAZY

Master of Science in Marine Technology,
École Centrale de Nantes, France,
born in Alexandria, Egypt.

This dissertation has been approved by the promotor.

Composition of the doctoral committee:

Rector Magnificus	Chairperson
Prof. dr. ir. J.W. van Wingerden	Delft University of Technology, promotor
Dr. ir. P. Naaijen	Delft University of Technology, copromotor

Independent members:

Prof. dr. ir. A.C. Viré	Delft University of Technology
Prof. dr. S. Aubrun	École Centrale de Nantes, France
Prof. dr. ir. T.A.E. Oomen	Delft University of Technology/ TU Eindhoven
Dr. S.H. Hossein Nia Kani	Delft University of Technology
Dr. S. Raach	sowento GmbH, Germany



Keywords: Offshore energy, floating wind turbines control, wave prediction, feed-forward control, feedback control, robust control, optimisation

Printed by: Ipskamp Printing, The Netherlands

Cover:

Funding: This work is part of the FLOATECH project. A European Union's Horizon 2020 research and innovation programme funded under the Energy programme (LC-SC3-RES-31-2020 - Offshore wind basic science and balance of plant) under grant agreement number 101007142.

Copyright ©2025 by A.R.M. Hegazy

ISBN: 978-94-6518-141-7

An electronic version of this dissertation is available at
<http://repository.tudelft.nl/>.

Contents

Summary	vii
Samenvatting	ix
Acknowledgments	xi
1 Introduction	1
1.1 Why wind energy?	2
1.2 Offshore wind energy	3
1.3 Wind turbine control.	8
1.4 Floating wind turbine control challenges	14
1.5 Thesis objective and outline	17
2 Wave Feedforward Control for Large Floating Wind Turbines	21
2.1 Introduction	22
2.2 Floating Wind Turbine Description.	23
2.2.1 Floating Wind turbine Model.	24
2.2.2 Spectral Estimation and Identification	25
2.3 Controller Design	26
2.4 Results	29
2.5 Conclusions	33
3 The Potential of Wave Feedforward Control For Floating Wind Turbines:	
A Wave Tank Experiment	35
3.1 Introduction	36
3.2 Experimental Setup	39
3.2.1 Floating wind turbine model	39
3.2.2 Measurements	41
3.2.3 Software-In-the-Loop system.	42
3.2.4 Wave loads prediction	42
3.3 Synthesis of the wave feedforward controller	43
3.3.1 Data-driven approach	44
3.4 Results	47
3.4.1 Control objective.	47
3.4.2 Effect of turbulence intensity variation	50
3.4.3 Effect of significant wave height variation	53
3.4.4 Effect of wave directional spreading	55
3.4.5 Controller performance at different wind speeds	57
3.5 Conclusions	58

4	A Novel Control Architecture for Floating Wind Turbines	61
4.1	Introduction	62
4.2	Floating Wind Turbine description	63
4.2.1	Floating Wind Turbine Model	63
4.3	Conventional Control Design	66
4.3.1	Detuning.	66
4.3.2	Parallel Compensation (MISO & MIMO)	66
4.4	SIMO Control	68
4.5	Results	70
4.6	Conclusion.	72
5	Control Design for Floating Wind Turbines	73
5.1	Introduction	74
5.2	Problem background	76
5.2.1	Floating wind turbine model	78
5.2.2	Effect of RHP zeros.	84
5.3	Control of floating wind turbines.	85
5.3.1	Detuning.	85
5.3.2	Robust scheduled tuning	85
5.3.3	Multi-loop control	90
5.4	Results	98
5.5	Conclusion.	102
6	Conclusions and Recommendations	105
	Bibliography	111
	Curriculum Vitæ	123
	List of Publications	125

Summary

The EU aims for a 45% share of renewable energy by 2030, with wind energy playing a crucial role in its efforts to combat global warming. Offshore wind power has a vast potential and can significantly contribute to achieving this climate-neutrality target. Europe possesses an extensive offshore wind resource that is mostly located in deep waters, necessitating the installation of turbines farther from shore. Since conventional fixed-bottom foundations become impractical beyond depths of 50 meters, floating wind technology has emerged as a viable alternative. Although the cost of floating wind energy remains higher than bottom-fixed alternatives, continuous advancements are expected to make it more economically competitive. A key factor in reducing costs will be the improvement of turbine control systems, which will enhance energy efficiency while mitigating structural stress, ultimately prolonging the lifespan of these systems.

Floating wind turbines operate in challenging environments as they are constantly subjected to the dynamic forces of wind and waves. From a control perspective, these environmental factors act as external disturbances, introducing disruptions that drive the system away from its ideal operating state. Conventionally, wind turbines operate blindly without any real-time awareness of the surrounding environment of operation and, therefore, depend on reactive feedback control mechanisms to manage these disturbances. A promising approach for improving floating wind technology involves incorporating environmental data into turbine control systems and developing advanced control strategies based on this information. Recent advancements in LiDAR technology have enabled the detection and exploitation of upstream wind previews in advanced control algorithms to improve operation over conventional control algorithms, reducing the reliance on conventional feedback control to tackle wind disturbances. A comparable approach based on RADAR technology for wave detection holds significant potential, as waves contribute heavily to structural fatigue in floating wind turbines. Despite its potential, the application of wave sensing in control strategies remains largely unexplored. This thesis addresses this gap by investigating the feasibility and benefits of incorporating wave measurements into the control design for floating wind turbines.

A key contribution of this thesis is the development of a control approach aimed at mitigating wave-induced loads on floating wind turbines. Upon the wave-platform interaction, undesirable dynamic responses affecting the stability and performance of the turbine are generated. Should the incoming waves be anticipated before reaching the platform, a proactive control strategy can be implemented to alleviate the wave effects. However, instead of applying the more commonly used model-based control, data-driven control synthesis is adopted to further explore the potential of wave feedforward technology. A data-driven control method that takes into account the uncaptured dynamics in model-based is used. As part of this development, two distinct controllers have been designed: one aimed at reducing generator speed fluctuations and another focused on decreasing the platform pitching motion. These control strategies are integrated into a floating wind

turbine, working in conjunction with the conventional feedback controller responsible for generator speed regulation. To assess their effectiveness, extensive numerical simulations in a mid-fidelity simulation suite were conducted under realistic operational conditions, confirming that the proposed feedforward control successfully reduces the adverse effects on the generator speed caused by wave action. The controller is able to dampen the platform's pitching motion within the frequency range where linear wave effects are most prominent.

Furthermore, scaled-model wave tank experiments were conducted using a hybrid approach, with the platform's hydrodynamic response physically reproduced at scale and the turbine aerodynamics and control numerically simulated in real time. This setup enabled a comprehensive evaluation of wave feedforward controllers, previously developed and tested numerically, under varying environmental conditions, demonstrating their effectiveness.

The traditional feedback control of the floating wind turbines has its own challenges. While the feedback control of onshore wind turbines is well-established, applying the same controllers to floating offshore wind turbines causes the turbines to become unstable. Such instability is attributed to the coupling between the fore-aft motion and the wind turbine controller, which makes the wind turbine negatively damped. The non-minimum phase zeros existing in the transfer function from the blade pitch to the generator speed impose a fundamental limitation on the closed-loop bandwidth. The negative damping instability posing a challenge to the operation of the floating turbines. To address this problem, different solutions were proposed with varying control structures. In this thesis, a new control architecture that can lift the bandwidth limitation and alleviate the adverse effects of negative damping is proposed. Contrary to the other controllers requiring extra measurements in the literature, the proposed controller is more robust since it does not require additional measurements while preserving the industry standards.

To summarise, this thesis advances the state-of-the-art on floating wind turbine control technology through two contributions. First, integrating real-time wave data into novel control strategies to enhance both the turbine's power production and fatigue life. Second, delving deeper into the famous negative damping instability limiting the controller from a better performance. Ultimately, these advancements hold the potential to reduce the costs of floating wind energy, helping accelerate the global shift toward renewable resources.

Samenvatting

De EU streeft naar een aandeel van 45% hernieuwbare energie in 2030, waarbij windenergie een cruciale rol speelt in de strijd tegen de opwarming van de aarde. Offshore windenergie heeft een enorm potentieel en kan aanzienlijk bijdragen aan het behalen van de klimaat-neutraliteitsdoelstellingen. Europa beschikt over uitgebreide offshore windbronnen, die zich grotendeels in diep water bevinden. Daardoor moeten windturbines verder uit de kust worden geplaatst. Omdat conventionele vaste funderingen onpraktisch worden bij dieptes groter dan 50 meter, is drijvende windtechnologie naar voren gekomen als een haalbaar alternatief. Hoewel de kosten van drijvende windturbines momenteel hoger liggen dan die van turbines met vaste funderingen, wordt verwacht dat voortdurende technologische vooruitgang de economische concurrentiekracht zal vergroten. Een sleutelfactor in het terugdringen van de kosten is de verbetering van de besturingssystemen van turbines, die niet alleen de energie-efficiëntie verhogen maar ook de belasting verminderen, wat uiteindelijk de levensduur van de systemen verlengt.

Drijvende windturbines opereren in uitdagende omgevingen waarin ze voortdurend worden blootgesteld aan dynamische belastingen van wind en golven. Vanuit het oogpunt van regeltechniek werken deze omgevingsfactoren als externe verstoringen die het systeem uit zijn ideale werktoestand duwen. Traditioneel werken windturbines zonder directe informatie over hun omgeving en vertrouwen ze volledig op reactieve terugkoppelingsmechanismen om verstoringen te beheersen. Een veelbelovende benadering om drijvende windtechnologie te verbeteren, is het integreren van omgevingsdata in de turbinebesturing en het ontwikkelen van geavanceerde regelstrategieën op basis hiervan. Recente vooruitgang in LiDAR-technologie maakt het mogelijk om windsnelheden vóór het bereiken de turbine te detecteren en deze informatie te benutten in geavanceerde algoritmes, waardoor de afhankelijkheid van conventionele terugkoppeling wordt vermindert. Een vergelijkbare aanpak met RADAR-technologie voor golfdetectie biedt eveneens veel potentie, aangezien golven in sterke mate bijdragen aan vermoeiingsbelasting van drijvende windturbines. Ondanks dit potentieel is de toepassing van golfmetingen in besturingsstrategieën nog nauwelijks onderzocht. Dit proefschrift verkent deze leemte door de haalbaarheid en voordelen van het opnemen van golfmetingen in de regeltechniek voor drijvende windturbines te onderzoeken.

Een belangrijke bijdrage van dit proefschrift is de ontwikkeling van een regelsysteem dat gericht is op het verminderen van door golven veroorzaakte belastingen op drijvende windturbines. De interactie tussen platform en golven wekt ongewenste dynamische respons op die de stabiliteit en prestaties beïnvloeden. Door inkomende golven vooraf te voorspellen, kan een proactieve ('feedforward') regeltechniek worden toegepast om deze effecten te beperken. In plaats van het meer gebruikelijke 'model-based control', is hier gekozen voor een 'data-driven control' benadering om het potentieel van wave feed-forward technologie beter te benutten. Een data-driven methode maakt het mogelijk dynamica mee te nemen die door modellen niet volledig worden beschreven. Binnen dit onderzoek

zijn twee verschillende regelaars ontworpen: één gericht op het beperken van fluctuaties in generatorsnelheid en één op het reduceren van de stampbeweging van het platform. Deze regelstrategieën zijn geïntegreerd in een model van een drijvende windturbine en zijn gelinkt aan de conventionele terugkoppelingsregeling voor de generatorsnelheid. Uit uitgebreide numerieke simulaties in een ‘mid-fidelity’ simulatieomgeving onder realistische omstandigheden blijkt dat de voorgestelde feed-forward regeling effectief de negatieve golfinvloeden op de generatorsnelheid vermindert en de platformbewegingen dempt binnen het frequentiebereik waar lineaire golfeffecten het sterkst zijn.

Daarnaast zijn schaalmodelproeven uitgevoerd in een golfbassin met een hybride aanpak: de hydrodynamische respons van het platform werd fysiek op schaal nagebootst, terwijl de aerodynamica van de turbine en de besturing in real time softwarematig werden gesimuleerd. Deze opstelling maakte een grondige evaluatie mogelijk van de eerder ontworpen feedforward regelaars, onder uiteenlopende omgevingscondities, en toonde hun effectiviteit aan.

Het toepassen van conventionele terugkoppelingsregelaars op drijvende windturbines kent eigen uitdagingen. Waar terugkoppeling bij onshore windturbines goed werkt, kan dezelfde regeling bij drijvende offshore turbines leiden tot instabiliteit. Deze instabiliteit wordt veroorzaakt door de koppeling tussen de voor-achterwaartse beweging van het platform en de windturbinebesturing, wat resulteert in negatieve demping. Bovendien leggen de ‘non-minimal phase zeros’ in de overdrachtsfunctie van bladpitch naar generatorsnelheid een fundamentele beperking op aan de regelbandbreedte. Deze negatieve demping vormt een belangrijk obstakel voor stabiliteit. In dit proefschrift wordt een nieuwe architectuur voor de regelaar voorgesteld die deze beperkingen doorbreekt en de negatieve demping vermindert. In tegenstelling tot andere voorgestelde oplossingen in de literatuur, vereist deze aanpak geen extra input van sensoren en sluit hij goed aan bij industriële standaarden, waardoor de robuustheid toeneemt.

Samenvattend levert dit proefschrift twee bijdragen aan de ontwikkeling van besturingstechnologie voor drijvende windturbines. Ten eerste: het integreren van real-time golfdata in nieuwe regelstrategieën om zowel de energieproductie als de vermoeiingslevensduur te verbeteren. Ten tweede: een diepere analyse en oplossing voor het bekende probleem van negatieve demping die de prestaties van conventionele regelaars beperkt. Uiteindelijk hebben deze verbeteringen het potentieel om de kosten van drijvende windenergie te verlagen en zo de wereldwijde transitie naar duurzame energie te versnellen.

Acknowledgments

"I hate control! I never want to come across that subject ever again!" Those were my exact words after barely surviving the automatic control course during my bachelor's in Egypt. How naive I was. Little did I know that a few years later, I'd be doing a PhD on the very subject I had vowed to avoid forever.

Fast forward to September 2020. Fresh off my master's thesis defense and riding the wave of academic freedom, I thought, "Let's ruin that by applying for a PhD!" While browsing PhD opportunities, I stumbled upon a position in — of all things — control of floating wind turbines. I laughed, hesitated, and then decided to ask my master's thesis supervisor, Prof. Sandrine Aubrun (now also on my PhD committee), for advice. Her response: "It's a great opportunity — but be careful. Their entire focus is control, and I know that's not exactly your background." "Exactly," I said. "I'll apply, get rejected, and move on with my life." As it happened, the outcome was quite the opposite. Shortly after, I received an invitation from Prof. Jan-Willem van Wingerden for a first-round interview. Naturally, I assumed they had sent the invitation to the wrong person, but I figured I'd give it a shot — I had nothing to lose. Then came the second interview. This time, I decided to be upfront: "All I know about control is Bode plots and poles and zeros," I told Jan-Willem. "So I wanted to be transparent about my lack of expertise in the field." Next thing I knew, I was officially a PhD candidate in control. Thrilled and mildly terrified, I embraced the opportunity, stepping into a field I barely knew. But Jan-Willem reassured me: "Take a few courses, and you'll be fine." And he was right. What once felt like dark magic gradually started to make sense. Looking back, I'm incredibly grateful I took that leap. It turns out that the subject I once ran from became the heart of my research, and a surprisingly fulfilling adventure.

I would like to begin by thanking my promotor and mentor, Jan-Willem. Dear Prof., no words can truly express how grateful I am for the opportunity and everything you've done for me. Your constant support, encouragement, and belief in me have meant the world. Your dedication to your work, your brilliance, your kindness, and the enthusiasm for research and science that you so effortlessly instill in your students are truly inspiring. I have always been amazed by the stream of ideas you generate for each of us in the group — may it never stop (and may the group keep growing!). On a personal note, your visit to Morocco meant more to me than I can put into words — it spoke volumes about your character and how much you care. And of course, I couldn't have asked for a better dance partner back in Glasgow! It has been an absolute honour to be part of your team.

To my co-promotor, Dr. Peter Naaijen — Dear Dr. P, thank you for your genuine curiosity about my research and the depth of your questions. Your thoughtful challenges continuously pushed me to sharpen my thinking, communicate more clearly, and broaden my perspective. I have always admired your brilliance and the clarity with which you approach complex problems, as well as your calm, kind nature that made working with you such a pleasure. You have played a pivotal role in shaping my journey — not only

through your academic guidance, but also by taking me under your wing at Next Ocean. Your patience, encouragement, and willingness to teach me something new every day have left a lasting impact on me. For all of this, and so much more, I am deeply and forever grateful.

At DCSC, I had the pleasure of meeting some truly amazing people. Within the wind energy group in particular, I've been lucky to share this journey with many of you. Mees — thank you, broertje, for the good times we've had and those still to come, for our discussions over a broodje shawarma, for being supportive and getting the same grade in the MPC course, and special thanks for always helping me practice my Dutch — your support has prepared me well for my Dutch exams. And of course, thank you for trying to teach me how to ski... even though I'm still terrible at it. Rogier — mijn kerel, thank you for doing the same, with your posh Dutch accent and that unmistakable Scottish flair. Thank you for sharing those hilariously bad surfing moments in Barbados, and for helping me wrap my head around the data-driven control stuff. Emanuel — my German brother, thank you for the great moments we've shared (and will continue to share), the long walks, our deep discussions about fluid dynamics and wind farm wakes, your genuine curiosity about every food I recommend, and most of all, for never saying no to konafa. Mi hermano y el grande jefe, Unai — thank you for always making time to meet whenever you're in the Netherlands. I've always looked forward to our hangouts (hopefully next time in Spain!), and I hope you'll keep visiting, even post-PhD. Marion — even though you joined our group later, it felt like you had always been part of it. It also gave me the chance to practice my long-forgotten French. Thank you for that! Malheureusement, tu as démenagé en France, mais bon courage avec ton boulot là-bas inshaa'Allah, et j'espère qu'on se reverra plus souvent, aux Pays-Bas ou en France. David — thank you for everything, brother. We started this PhD journey together without knowing a thing about control, and here we are, defending our PhDs just two weeks apart. And thank you for making it to Morocco, despite all the challenges you faced. Marcus — my second German brother and the visualisation wizard, thank you for always being ready to help and for inviting me to witness your ultimate frisbee skills in action. Jonas — my third German brother (yes, we had many Germans in the group — and there's still a fourth below!), thank you for the surfing lesson in Barbados, even if I was pretty hopeless at it. Sebas — thank you for always taking the time to explain things patiently, and for those little Dutch lessons here and there. A big thank you to the rest of the wind group: Daniel, Atin, Maarten, Daan, Yichao, Livia, Claudia, Jean, Guido, Matteo, Tim, Jesse, Alexandra, Tristan ... the list goes on! Thank you all for the amazing experience. Outside the wind energy group, I'd also like to thank Coen, Sander, Max, Tushar, Roger, and everyone else at DCSC — thank you for making it such a memorable time.

To my parents, Raafat and Hanaa — thank you for your endless prayers, love, and support. To my sister, Nouran — thank you for taking care of our parents while I being away. To my grandmother — your prayers have always been a guiding light in my life. To my late grandfather — I lost you during this journey, and I wish you were here to witness these steps I am taking; may you rest in peace. To my late uncle Ahmed — I know you would have loved to be with me on this special occasion. You supported me from the very beginning, and a large part of where I am today is thanks to your constant help and encouragement. May you rest in peace. Thank you to my uncles and aunts for keeping me

in your prayers. Thank you to my coach, Harry Dunlop, Ms. Alston Yacoubian, and Mr. Peter Yacoubian, who were the first to welcome me to Scotland when I left Egypt for my studies and have been my second family abroad. To my parents-in-law — thank you for your love, unwavering support and heartfelt encouragement throughout this time. Finally, to my wife, my love, Wassima—these past four years have been a whirlwind, and we have been through so much together. You left your life in France and selflessly followed me to the Netherlands, leaving everything behind. I thank god every day that you did, because I truly can not imagine my life without you. Thank you for always standing by my side, for your unwavering support, and for your love through every step of this journey. We've shared unforgettable adventures, and I am eternally grateful for each and every one of them—and for all those still to come. Je t'aime trop, mon cœur.

Amr
Amsterdam, October 2025

1

Introduction

The adverse repercussions of climate change demand urgent and significant action, with wind energy development playing a key role in the transition to renewable energy. In recent years, wind energy has emerged as one of the most cost-effective energy sources, driven by significant technological advancements. This is particularly evident following the introduction of floating offshore wind turbine concepts, which enable access to higher-quality wind resources and, consequently, greater power generation. However, due to its elevated cost of energy, floating wind energy is not yet economically attractive. As a result, advancing their control algorithms is critical to improving their cost-effectiveness and accelerating their large-scale adoption. To establish the context and rationale for this research, this chapter begins with introducing the recent trends in wind energy, followed by an overview of modern wind turbine control. It then summarises the current state-of-the-art methods and challenges in wind turbine control. Finally, the chapter presents the primary objectives and contributions of this thesis, concluding with an outline of the thesis structure.

1.1 Why wind energy?

Global warming has been decisively linked to human-driven activities, particularly the emission of greenhouse gases, which contributed to an estimated rise in global surface temperatures of 1.1°C above pre-industrial (1850–1900) levels during the 2011–2020 period. This brings the world alarmingly close to the 1.5°C threshold set by the Paris Agreement in 2015 [1], highlighting the urgency of intensified climate action. Emission levels continued to climb between 2010 and 2019 [2], shaped by longstanding disparities in responsibility and influenced by unsustainable practices in energy production, land management, consumption habits, and production systems. These contributions are unevenly distributed across regions, nations, and social groups. The ongoing alteration of the climate system by human influence has already intensified the frequency and severity of extreme weather events worldwide. This has triggered significant disruptions to essential resources such as food and water, compromised public health, strained economies, and caused ecological and societal losses on a global scale [2].

Addressing climate change necessitates limiting the release of greenhouse gases that trap heat within the Earth's atmosphere. This entails significantly lowering emissions from primary contributors such as industrial facilities, energy production, transportation systems, and agricultural activities. Achieving meaningful reductions requires a systemic transformation across all sectors of human activity, including how we produce energy. Wind power is anticipated to lead the clean energy transition, supplying at least 50% of the European Union's electricity needs [3].

Wind energy is a renewable energy source that harnesses the wind's kinetic energy via wind turbines to generate electricity, making it a pivotal player in the global transition toward sustainable energy solutions. Today, wind energy accounts for a notable portion of electricity generation in Europe, with an installed capacity surpassing 285 GW, which is expected to grow to 450 GW by 2030, and projections indicate continued growth as nations strive for ambitious climate targets, such as achieving net-zero emissions by 2050 [4, 5]. Environmentally, wind power offers substantial benefits, such as a low carbon footprint and reduced air pollution. Unlike fossil fuel-based power generation, wind energy does not emit greenhouse gases during operation. Its growing share in the energy mix has contributed to a significant reduction in net greenhouse gas emissions, with a reported 31% decrease in 2022 compared to 1990 levels [6]. Furthermore, wind farms contribute to cleaner air quality, which is associated with fewer health issues related to air pollution, thereby fostering public health improvements in surrounding communities. As the demand for clean energy grows, wind energy's capacity to address climate change, stimulate economies, and foster community engagement positions it as a vital component of the global energy transition.

Wind energy is commonly classified into two main categories: onshore and offshore. Onshore wind farms are typically sited in regions with consistent wind activity; however, terrestrial wind patterns are highly variable over daily cycles, which constrains the consistency of power output. Additionally, the most favourable sites for harnessing wind energy are frequently situated at considerable distances from urban centres, where electricity demand is concentrated—posing logistical and infrastructural challenges. Furthermore, residents near these installations may express concerns related to the visual impact and acoustic disturbances produced by the turbines.

In contrast, offshore wind energy is gaining momentum due to several key advantages

over onshore wind [7]. Open sea environments provide vast, unobstructed areas for energy extraction, free from constraints such as urban development or dense human activity. Additionally, wind conditions offshore tend to be more consistent and exhibit higher speeds with reduced turbulence. These sites also offer the benefit of minimising visual and acoustic disturbances for nearby populations.

1.2 Offshore wind energy

The European Union’s Offshore Renewable Energy Strategy outlines a goal of reaching a minimum of 300 GW in offshore wind capacity by 2050. Although this represents a significant increase from current levels, it still constitutes a small fraction of Europe’s overall offshore renewable potential, which is estimated at 4,673 GW across multiple sea basins as depicted in Fig. 1.1. Achieving the 300 GW target would, therefore, utilise only about 6% of this theoretical capacity. Of the total potential, approximately 1,542 GW is located in areas suitable for bottom-fixed offshore wind installations, while the remaining 3,131 GW lies in deeper waters—exceeding 75 meters in depth—requiring the deployment of floating wind technologies [8].

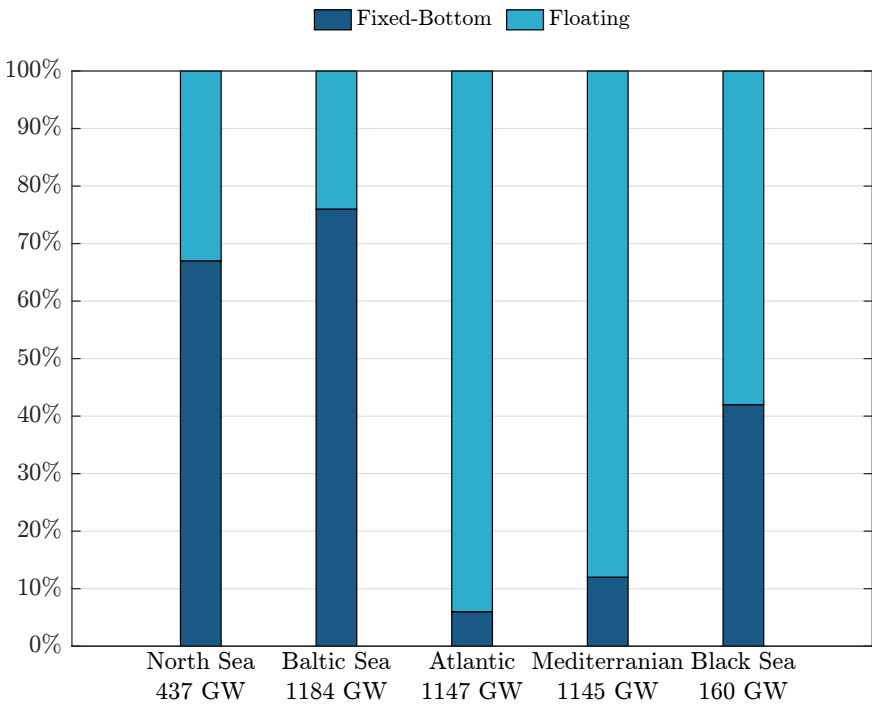


Figure 1.1: Europe’s offshore wind potential and its distribution per sea basin and technology. Data collected from [8].

Despite the benefits, offshore wind development presents several challenges [9]. These include elevated costs associated with permitting procedures and engineering require-

ments, greater consumption of raw materials, and the complexity and expense of installation—which necessitates highly skilled labour. Moreover, adequate port facilities are essential for transporting and assembling large components. For offshore sites located far from the coast, the need for costly subsea cabling becomes critical, and the system's reliability and accessibility tend to decline as the distance from shore increases.

Offshore wind turbines that are currently in operation predominantly utilise anchored foundations secured to the seabed, known as fixed-bottom offshore wind turbines. This approach, viable in coastal regions with depths below 50 meters, represents the conventional method for harnessing offshore wind power. Emerging from this foundation, floating platform technology has been developed, where turbines are mounted on floating structures. These systems enable deployment in deeper waters and offer operational benefits, such as partial assembly and maintenance in sheltered port facilities, away from the punishing conditions of open waters. Nevertheless, these benefits are accompanied by increased technical challenges, requiring advanced engineering solutions to improve economic viability. Despite current limitations, the versatility of floating wind turbines positions them for accelerated development in coming years, promising broader access to untapped offshore wind resources.

Bottom-fixed offshore wind energy

Bottom-fixed offshore wind turbines are secured directly to the seabed using rigid support structures. The most common foundation types include monopiles, gravity-based systems, and jacket structures. A transition piece typically serves as the interface between the foundation and the turbine tower, while the anchoring mechanism to the seabed may involve gravitational load, pile-driven penetration, or suction-based methods.

The offshore wind industry is currently evolving towards the deployment of larger turbines in progressively deeper marine environments. Monopile foundations are typically used at depths up to 35 meters, while jacket structures extend this capability to around 80 meters [10]. Ongoing technological advancements continue to expand these depth limits. Nevertheless, most of the world's oceanic regions lie at much greater depths, beyond the reach of fixed-bottom solutions. As a result, there is growing momentum toward adopting floating wind technologies.

Floating offshore wind energy

Floating offshore wind technology, atop floating platforms instead of fixed foundations, expands the possibilities for wind energy by enabling turbine installation in deeper and more distant ocean areas with stronger and more consistent wind speeds. This technology removes a major barrier to scaling up clean and renewable energy production in support of long-term sustainability goals.

In contrast to onshore and bottom-fixed offshore wind turbines, floating offshore wind turbines exhibit additional platform Degrees Of Freedom (DOFs) due to their moored, flexible connection to the seabed. As depicted in Fig. 1.2, these DOFs include translational motions—surge, sway, and heave—as well as rotational motions—roll, pitch, and yaw. The presence of these six dynamic modes introduces complex interactions between aerodynamic loading and wave-induced hydrodynamic forces [11].

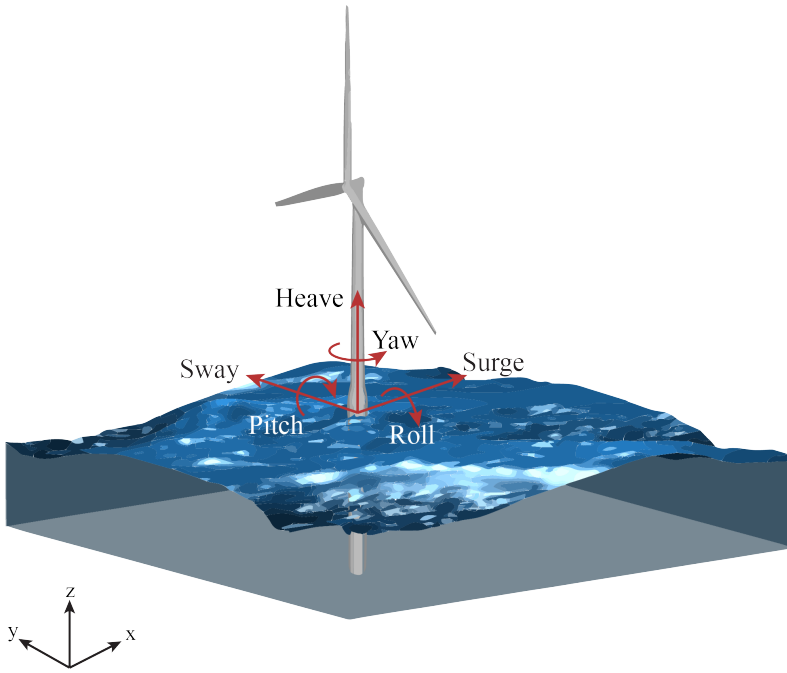


Figure 1.2: Illustration of the degrees of freedom of the floating platform of a floating wind turbine.

Floating offshore wind offers several notable advantages, including a potentially minimal environmental impact, lower visual and acoustic disturbance, and greater logistical flexibility in terms of construction and deployment. The ability to assemble turbines onshore and transport them to their offshore sites by towing helps reduce the need for specialised installation vessels. Additionally, deployment in deeper waters allows access to more powerful and stable wind conditions, leading to increased energy production and enhanced operational performance.

The deployment of floating offshore wind serves as a strategic extension to the bottom-fixed offshore wind industry by increasing supply chain capacity and introducing new technological solutions and market participants. This expansion is expected to enhance the maturity of the overall sector while accelerating innovation. As a result, increased research convergence is anticipated in key areas such as turbine architecture, subsea cable systems, electrical interconnections, and operation and maintenance practices, thereby driving forward the technological development of offshore wind energy as a whole.

The primary environmental disturbances acting on floating wind turbines are wind turbulence and sea waves. Wind is inherently variable across a wide range of spatial and temporal scales. From the perspective of wind turbine performance, fluctuations in wind speed on time-scales from minutes down to seconds are classified as turbulence. According to Van der Hoven's wind spectrum [12], turbulence typically occurs within the range of 10 minutes to a few seconds. In the case of waves, the most relevant are wind-generated surface gravity waves, which generally exhibit periods between 5 and 25 seconds [13]. Recognising these characteristic time scales is crucial for ensuring both the safe operation

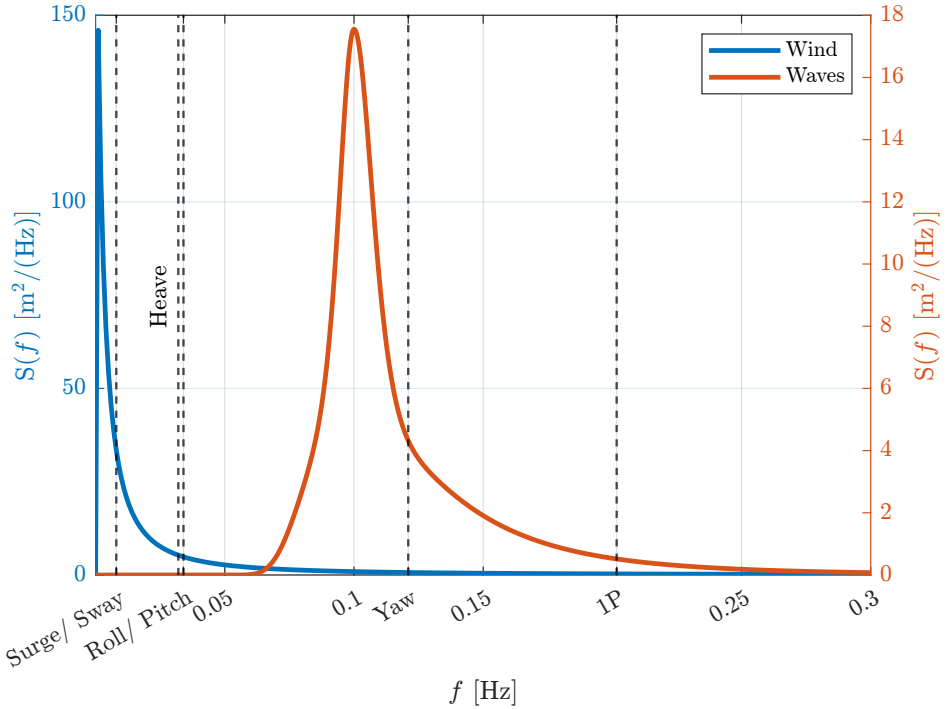


Figure 1.3: Kaimal wind spectrum [15] together with JONSWAP wave spectrum [16] showcasing the operating frequency range for the NREL 5 MW wind turbine [17] atop the OC3 floating platform [18], with the vertical dashed lines depicting the natural frequencies of the different modes [19].

and the long-term survivability of floating wind turbines [14]. Figure 1.3 illustrates a representative energy spectrum of wind and waves, where the Kaimal spectrum [15] is used for the wind and the JONSWAP spectrum [16] for the waves. The natural frequencies of selected DOFs of the NREL 5 MW reference turbine [17] mounted on the symmetric OC3 floating platform [18] are also indicated [19], providing insight into the dynamic environment in which the floating turbine operates. The key takeaway from Figure 1.3 is the importance of avoiding overlap between the turbine's natural frequencies and frequency bands with high spectral energy from wind or waves.

Floating offshore wind turbines must maintain adequate stability to minimise motion and ensure consistent operational performance. To meet this requirement, a range of platform configurations has been developed, as depicted in Fig. 1.4. Among the key factors influencing the selection of a floating platform concept, water depth is typically the most critical. Nonetheless, seabed conditions significantly affect the choice of mooring system, which in turn can influence the platform design. Moreover, the prevailing wave climate at a prospective deployment site plays a critical role in the selection and design of floating wind turbine platforms. It influences platform stability, structural loading, mooring requirements, and control system complexity, thereby constraining the suitability and cost-effectiveness of specific platform configurations. On a positive note, unlike fixed-bottom structures,

the cost of floating platforms is relatively insensitive to increasing water depths. This is because the main depth-related cost driver is the mooring system, while the cost of the platform itself remains largely unaffected by water depth variations [20].

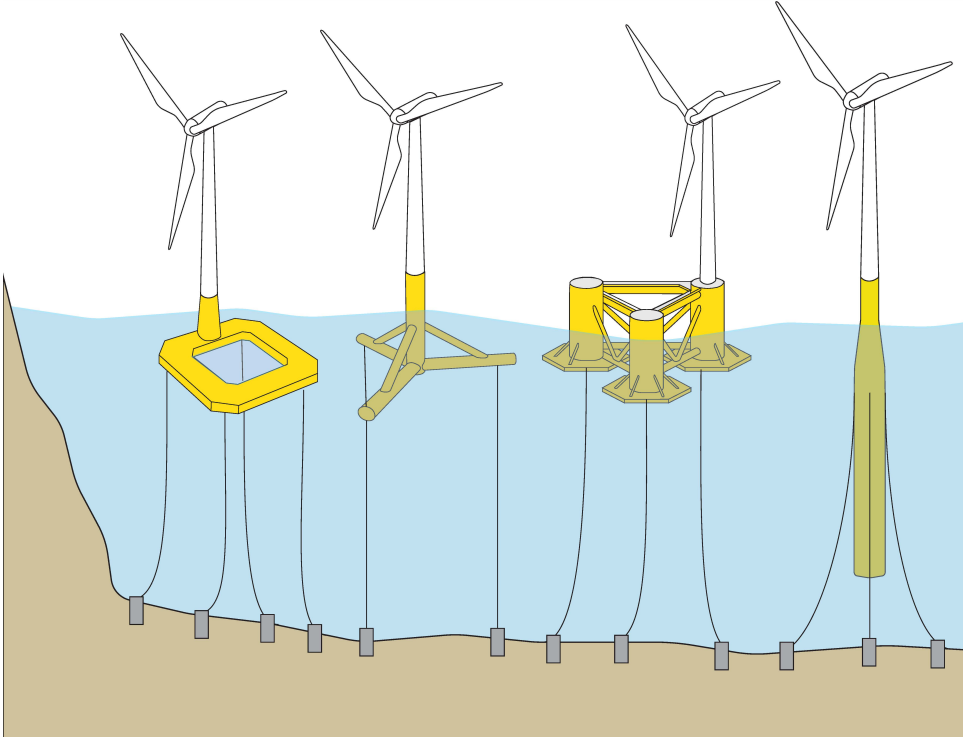


Figure 1.4: Illustration of the most common floating platform technologies in floating offshore wind energy. From left to right: Barge, Tension-Leg Platform (TLP), Semi-Submersible, and Spar buoy.

The cost of floating offshore wind energy is projected to decline dramatically by 2030 [21]. Given the shared components between floating and bottom-fixed wind turbines, cross-sector knowledge transfer is expected to accelerate the floating offshore wind development. Conversely, innovations in floating systems may also benefit conventional offshore technologies. As commercial deployment advances, FOWTs have reached ratings comparable to bottom-fixed turbines, with expectations of further scaling driven by stronger winds in deep waters. Improvements in technology and operations are anticipated to enhance capacity factors and reduce the Levelized Cost Of Energy (LCOE) [22].

To make floating offshore wind energy cost-competitive with other energy sources, large volumes of floaters need to be produced and installed, and next-generation wind turbines must be designed with reduced structural mass by adopting lighter and more flexible components, including the blades, drivetrain, and tower. However, as turbines grow in size and flexibility, they become more susceptible to dynamic interactions and fluctuating loads. If not properly managed, these effects can undermine overall system performance and stability. Consequently, advanced control strategies must be developed

to account for and mitigate the challenges posed by structural flexibility and dynamic behaviour [23, 24].

1.3 Wind turbine control

In the wind energy sector, large-scale wind turbines are primarily designed with an upwind, three-bladed, horizontal-axis configuration as depicted in Fig. 1.5. The tower serves as the main structural support, with the nacelle mounted on top. The rotor, composed of the blades and a central hub, harnesses wind energy to generate torque, which is subsequently transferred to a generator for electricity production [14, 25].

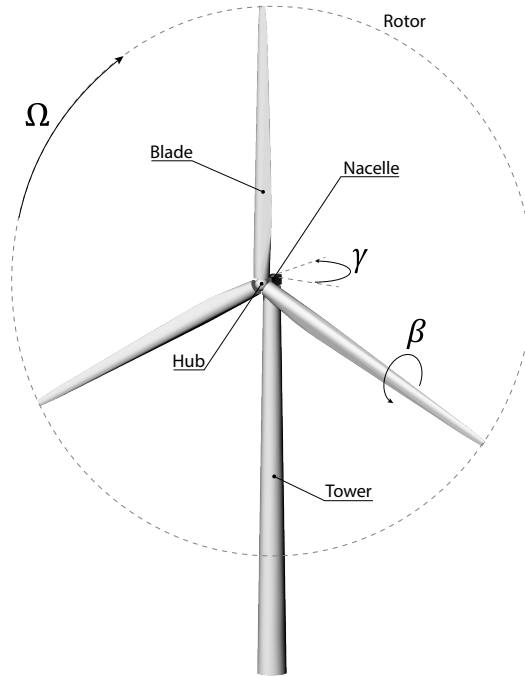


Figure 1.5: Illustration of a modern wind turbine with some of its main components. The figure illustrates the various actuated degrees of freedom available in the wind turbine system, namely, rotor speed control (Ω), blade pitch control (β), and yaw control (γ).

Some wind turbines have an integrated gearbox to adjust the mechanical output, converting the rotor's high torque and low rotational speed motion at the rotor's Low-Speed Shaft (LSS) into a lower torque and higher rotational speed at the generator's High-Speed Shaft (HSS). However, other turbine configurations eliminate the gearbox, opting for a direct-drive system where the rotor directly powers the generator without intermediary torque or speed adjustments [14, 26].

This collection of components—rotor, gearbox, generator, and shafts—is collectively termed the drivetrain, with the generator and gearbox enclosed within the nacelle. The Rotor-Nacelle Assembly (RNA) has the capability to yaw about the tower's axis, adjusting

the rotor's orientation to match the direction of the incoming wind. This alignment helps maintain optimal energy capture while minimising structural stress caused by yaw-induced forces. However, within a wind farm, deliberately introducing a slight misalignment of individual turbines relative to the prevailing wind can be advantageous. This strategic offset redirects the wake effect, reducing its impact on downstream turbines and ultimately enhancing the collective energy output of the entire farm [27–29].

The wind turbine control system includes multiple sensors, actuators, and a hardware-software system that processes sensor input signals and generates output signals for the actuators. The system responsible for processing inputs and producing outputs typically comprises a computer- or microprocessor-based controller that performs the essential control functions required for turbine operation. Additionally, a supervisory control system is included to manage transitions between different turbine operational states, such as standby, startup, power generation, shutdown, and emergency stops triggered by faults. The computer-based controller, together with the supervisory control system, form the main control system. The safety mechanism, on the other hand, operates independently from the main control system, serving as its back-up in case of critical conditions, and takes over if the main system appears to be failing to secure the turbine, thus overriding the main control system to bring the turbine to a safe state should a serious problem occur [14].

Wind turbine control objectives

Modern wind turbines are typically designed to operate for 20 years or more [14], during which they must generate as much power as possible to maximise electricity production and profitability. At the same time, they must withstand continuous and complex mechanical stresses to avoid premature decommissioning caused by damage from various and persistent wind-induced loads. These two goals are the primary focus of wind turbine control systems. In regions with abundant wind resources and high wind power integration, transmission system operators often impose additional requirements on wind turbines, such as the ability to support grid stability by balancing power generation and load. This is referred to as grid ancillary services [14]. Additionally, wind turbines, which consist of numerous moving and interacting parts, produce acoustic noise during operation. From an environmental perspective, excessive noise can be undesirable and may impact the public acceptance of wind turbines. Therefore, controlling noise levels, at least to some degree, is also desirable. These latter two requirements represent the secondary control objectives for wind turbines [14, 30–32].

Control strategies must be designed to match the wind turbine's operating regime, based on the available inputs and how they affect the system's dynamic behavior [30, 31, 33–35]. This classification hinges on whether the generator torque can be manipulated to enable rotor speed variation (i.e., fixed-speed versus variable-speed control) and whether the aerodynamic torque can be modulated via blade pitch actuation (fixed-pitch versus variable-pitch control) [14]. Modern large-scale wind turbines predominantly adopt a Variable-Speed, Variable-Pitch (VS-VP) configuration [30, 31], owing to its superior controllability and flexibility in achieving multi-objective performance criteria—namely, optimal power capture, closed-loop rotor speed regulation, and mechanical load attenuation. Within the context of the VS-VP framework and with an emphasis on the feedback control architectures and actuation strategies employed, those control objectives include:

1

I. Power regulation

The power existing in the wind at a certain speed is:

$$P_w = \frac{1}{2} \rho A v^3, \quad (1.1)$$

where ρ , A , and v are the air density (kg.m^3), rotor swept area (m^2), and free-stream wind speed (m/s), respectively. Wind turbine blades generate lift to drive the rotation of the wind turbine rotor, which drives the generator for the conversion of aerodynamic torque to electrical power. The aerodynamic power P_a extracted by a wind turbine, calculated as

$$P_a = P_w C_p(\beta, \lambda), \quad (1.2)$$

is limited by the power coefficient C_p , which is a function of the blade pitch angle β and the Tip-Speed Ratio (TSR), defined as $\lambda = \Omega R/v$, where Ω denotes the rotor's angular velocity. For a given wind turbine, the C_p can be computed numerically through Blade Element Momentum (BEM) theory, which accounts for both aerodynamic and momentum-based forces across the blade span. The Betz limit [36], expressed as $C_{p,Betz} = 16/27 \approx 0.59$, represents the upper theoretical efficiency bound for energy extraction from an idealised actuator disk model and, thus, a theoretical maximum for the power coefficient [14, 37].

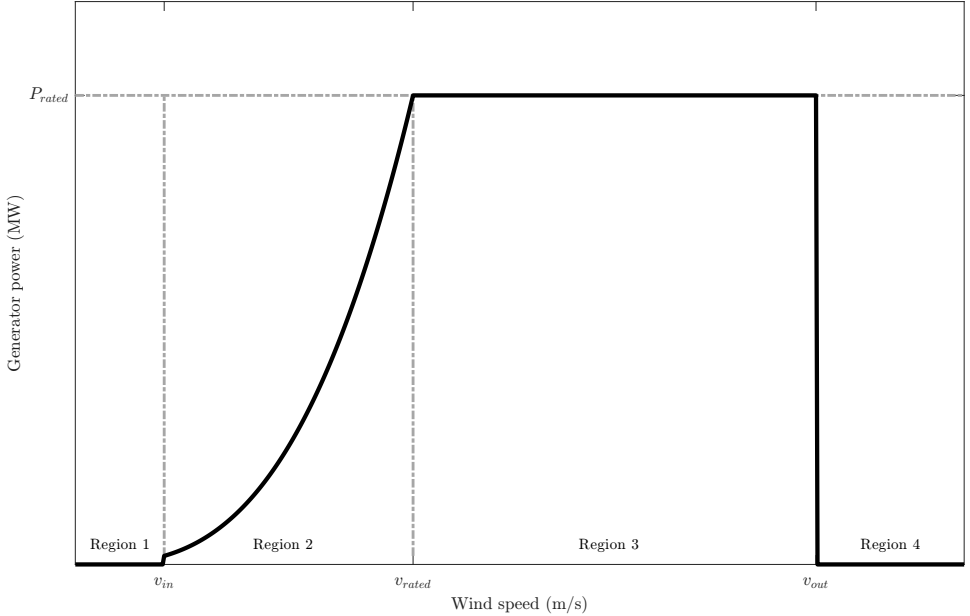


Figure 1.6: A simplified illustration of a standard wind turbine power curve, where the black line represents the variation in generator power across three distinct operating regions. These regions are defined by the cut-in wind speed v_{in} , the rated wind speed v_{rated} , and the cut-out wind speed v_{out} . In Region 2, the turbine operates to maximise power extraction from the wind. In Region 3, a power regulation strategy is implemented to maintain generator output at its rated power $P = P_{rated}$. Power generation does not occur in Region 1 or beyond Region 3, primarily due to economic and safety constraints.

A depiction of a wind turbine's operating regions is provided in the power curve shown in Fig. 1.6. The power curve of a wind turbine is composed of different operating regions, with each region having its own distinct wind speeds as follows:

- **Region 1 (idle)** - $v < v_{in}$: In this operational regime, the control objective shifts away from power generation, as low wind speeds render energy capture inefficient and economically non-viable. The turbine is, therefore, commanded into a standby mode, where active power extraction is suspended. To enforce this idle condition, the pitch actuator sets the blades to a fully feathered position—typically around $\beta = 90^\circ$ —in order to suppress aerodynamic torque. This control action effectively decouples the rotor from the wind input, ensuring that rotational motion is inhibited.
- **Region 2 (below-rated/ partial load)** - $v_{in} \leq v \leq v_{rated}$: This operational region corresponds to wind conditions where the turbine is capable of maintaining an optimal TSR, though the wind speed has not yet reached the rated threshold. During this phase, the objective of the torque control system is to extract maximum energy from the wind while the blade pitch remains constant. The generator torque can either be managed through a conventional quadratic torque-speed relationship [30] or via a PI-based controller designed to track a reference rotor speed derived from estimated wind speed and the desired TSR [35, 38]. In this mode, the blades are set to a specific pitch angle called fine pitch, which typically aligns with the configuration that yields peak aerodynamic performance [30, 31].
- **Region 3 (above-rated/ full load)** - $v_{rated} \leq v \leq v_{out}$: Above rated wind speed, v_{rated} , the turbine enters a power regulation regime, where the control system's objective shifts from maximising output to maintaining the generated power at its rated set-point. This transition is necessary to prevent generator overloading. To achieve this, a collective blade pitch control loop is activated, adjusting the aerodynamic input by increasing the blade pitch angle. This adjustment reduces aerodynamic torque, enabling the rotor speed—and consequently, generator power—to be regulated. Simultaneously, the reduction in rotor thrust contributes to lowering structural loads, highlighting the dual role of blade pitch as both a power-regulating and load-mitigating actuator. Given the non-linear sensitivity of aerodynamic forces to pitch angle across Region 3, a gain-scheduled control structure is typically implemented to ensure a uniform dynamic response. As for generator torque control, either a constant-torque or constant-power strategy may be used, with the former offering improved compatibility with floating wind turbine dynamics, while the latter is more prevalent in fixed-bottom onshore applications [30, 31, 39, 40].
- **Region 4 (shut down)** - $v > v_{out}$: Beyond Region 3, where wind speeds exceed the cut-out wind speed, v_{out} , in Fig. 1.6, the control system prioritises structural safety over power production. Due to the excessive mechanical loading associated with such high wind speeds and their infrequent occurrence, continued operation is neither safe nor economically justified. As a result, the turbine transitions to a shutdown mode, where a control command drives the blades to a fully feathered state. This action eliminates aerodynamic torque, effectively halting rotor motion and ensuring the system remains in a non-operational, zero-power-output condition.

It is worth mentioning that the transition between the different operating regions is governed by switching logic. To capture the system's transitional behaviour more accurately, intermediate zones—commonly referred to as Region 1.5 and Region 2.5—are introduced between Regions 1 and 2 and Regions 2 and 3, respectively. These additional bands are typically used to describe the turbine's dynamic response during region-switching [17, 30, 35, 41, 42].

II. Structural load alleviation

Beyond the primary objective of the closed-loop controller, which is regulating power output under high wind conditions—and potentially maximising it during low-wind operation—it is evident that control actions significantly influence the structural loading experienced by the turbine. Therefore, load implications must be carefully considered during controller synthesis to prevent the introduction of detrimental stress through the control strategy itself. In fact, load mitigation can be formulated as an auxiliary control objective alongside traditional performance targets.

In many instances, objectives such as load alleviation and power regulation are inherently aligned. For example, curtailing output power in high winds contributes to reducing torque transmitted through the drivetrain. However, in certain scenarios, competing demands emerge, necessitating trade-offs in the controller's design. Consequently, the final controller configuration reflects a compromise between multiple performance and reliability criteria. Several wind turbine key components considering the load mitigation aspect are:

- **Tower base loads:** One of the fundamental limitations in the development of the pitch control algorithm arises from its impact on tower dynamics, particularly with respect to structural vibrations. The tower fore-aft mode and side-side directions are characterised by inherently low damping and a pronounced resonance behaviour, which can be sustained by even minimal excitation from ambient wind fluctuations [30, 31]. The magnitude of this response is highly sensitive to the limited damping present—primarily contributed by aerodynamic effects from the rotor. As such, careful attention must be paid during controller design to ensure that the existing damping is not diminished further and, ideally, that the control action contributes positively to the suppression of this mode. To this end, an active load control method is designed by scaling the integrated tower-top acceleration measurements with a gain negatively proportional to the tower-top velocity. Since collective blade pitch actuation directly interacts with the tower fore-aft dynamics, its influence alters the system's effective damping. Consequently, it is possible to reduce tower loads significantly without adversely affecting the quality of speed or power regulation [30, 31]. However, in the case of the side-side tower motion, either generator torque [31, 43, 44] or individual pitching [45, 46] can be chosen as actuators instead. The former actuator is directly linked to power generation, making its impact on power quality unavoidable, whereas the latter imposes higher costs due to increased mechanical wear on the pitch system.
- **Drivetrain loads:** The drivetrain dynamics of a wind turbine can be abstracted using a two-inertia model, where the rotor and generator are treated as separate rotating bodies coupled via a flexible shaft characterised by torsional stiffness and damping

elements [25]. In a variable-speed turbine operating at constant generator torque, insufficient damping can lead to oscillatory behaviour in the drivetrain, particularly near the natural frequency of the torsional mode. Such oscillations can result in significant gearbox torque fluctuations and adversely impact power output stability. A widely adopted mitigation strategy involves augmenting the generator torque reference with a dynamic compensation term derived from band-pass filtering the generator speed signal around the resonant frequency of the torsional mode, thereby enhancing modal damping through active control [14, 30, 31].

- **Blade loads:** Variations in wind speed distribution throughout the rotor plane—caused by factors such as wind shear and localised turbulence—introduce cyclic loading on the blades, contributing to fatigue. To alleviate loading at the blade roots, individual pitch control can be employed. This approach relies on strain gauges or fiber-optic sensors [26] measuring the bending moments at each blade root. The collected data is then used to calculate a pitch command for each blade, intentionally inducing asymmetric aerodynamic loading that compensates for the non-uniform wind field across the rotor disc [14, 30, 31].

Advanced control techniques

After outlining the primary control objectives of wind turbines and the conventional control strategies used to achieve them, the focus now shifts to advanced control methodologies. Specifically, this includes preview sensing, which involves employing supplementary sensors to detect incoming disturbances and enable proactive control actions.

Although feedback control effectively attenuates disturbances, it inherently operates with a delay, as the disturbance must first affect a system variable—such as rotor speed—before a corrective action can be applied. This delay is further exacerbated by actuator response times in wind turbines. To overcome these limitations, considerable research over the past two decades has focused on feedforward control strategies, which leverage preview measurements to initiate control actions in anticipation of incoming disturbances [47–49]. Feedforward control relies on a disturbance input model that characterises how disturbances affect the system dynamics. This model is integrated into the controller design to generate proactive control inputs that counteract disturbances upon their arrival [50, 51].

Advancements in sensing technologies have opened the door to integrating external disturbance data into wind turbine control strategies. For instance, the emergence of Light Detection And Ranging (LiDAR) systems has enabled the creation of sophisticated control schemes that leverage measurements of upstream wind field measurements to enhance turbine performance [48, 52–54].

LiDAR systems, typically installed on the turbine nacelle or within the rotor hub, emit forward-facing laser beams that reflect off airborne particles upstream of the turbine. By analysing the frequency shift between the emitted and reflected beams—caused by the Doppler effect—the system estimates the incoming wind speed [48]. The use of LiDAR-based wind preview is well-established in the control of onshore and bottom-fixed offshore wind turbines [49] and has more recently been extended to FOWTs to enhance rotor speed regulation and mitigate platform motion [55–58].

1.4 Floating wind turbine control challenges

Beyond the challenges faced by onshore turbines, floating wind turbines are subject to additional complexities as they must operate reliably amid the demanding offshore environmental conditions, particularly the additional wave-induced hydrodynamic loads. The presence of a floating platform introduces additional low-frequency dynamics, particularly in surge, heave, and pitch motions, coupled with the turbine's aerodynamic and structural responses [59, 60]. A primary dynamic interaction, examined in this thesis, is the coupling between platform pitch motion and control dynamics—commonly referred to as negative damping—where attempts to regulate generator speed at its rated value trigger sustained pitch oscillations [39, 61]. Another example is the roll–yaw lock phenomenon [62], where specific thrust conditions cause cyclic oscillations between the platform's roll and yaw motions. These couplings increase system complexity and pose significant challenges for control design, particularly in achieving stability, reducing platform motions, and maintaining power quality under varying environmental conditions [40, 63].

Attributed to the additional floater low-frequency dynamics [11, 64], various forms of instabilities arise [61]. Among these, the most pronounced is the negative damping instability—one of the primary control challenges in floating offshore wind turbines [39, 40, 63]. Negative damping emerges in Region 3, where the conventional wind turbine feedback controller encounters fundamental limitations in above-rated wind speed conditions [39, 61]. Typically, modern wind turbines regulate power in this region using collective pitch-to-feather control [30, 31]. However, this method induces adverse coupling with the platform's low-frequency rigid-body dynamics, particularly the pitch mode, on floating offshore structures [30, 39, 61]. Such coupling can lead to a weakly damped—or in more severe cases, an unstable—dynamic response, particularly when blade pitch controllers originally designed for onshore turbines are applied [39, 40, 63]. This issue stems from the overlap between the controller bandwidth and the frequencies associated with Right-Half Plane Zeros (RHPZs) in the FOWTs dynamics [63, 65]. As a result, the controller bandwidth is fundamentally constrained and must remain below the RHPZs frequencies to preserve closed-loop stability [39, 40, 60, 66].

As illustrated in Fig. 1.7, this instability manifests as a negative gradient in the thrust force with increasing wind speed—a characteristic intrinsic to pitch-to-feather turbines [63]. When wind speed rises above the rated value, the control system increases the blade pitch angle to maintain a constant generator torque. This, in return, reduces the aerodynamic thrust and torque, allowing the platform to decelerate in the downwind direction [14]. This reversal leads to upwind movement, which increases the relative wind speed experienced by the rotor. As a result, aerodynamic torque rises again, triggering additional pitch action, a feedback loop that can exacerbate instability [40, 63].

Several control strategies have been proposed to mitigate the negative damping instability, ranging from reducing the controller bandwidth of the conventional baseline controller [39, 40], to incorporating additional feedback loops that leverage extra sensors, actuators [40, 63, 65], or both [67], thereby increasing the number of control variables. While each of these approaches offers distinct advantages and trade-offs, a notable gap remains in the development of systematic tuning methods specifically targeting this form of instability.

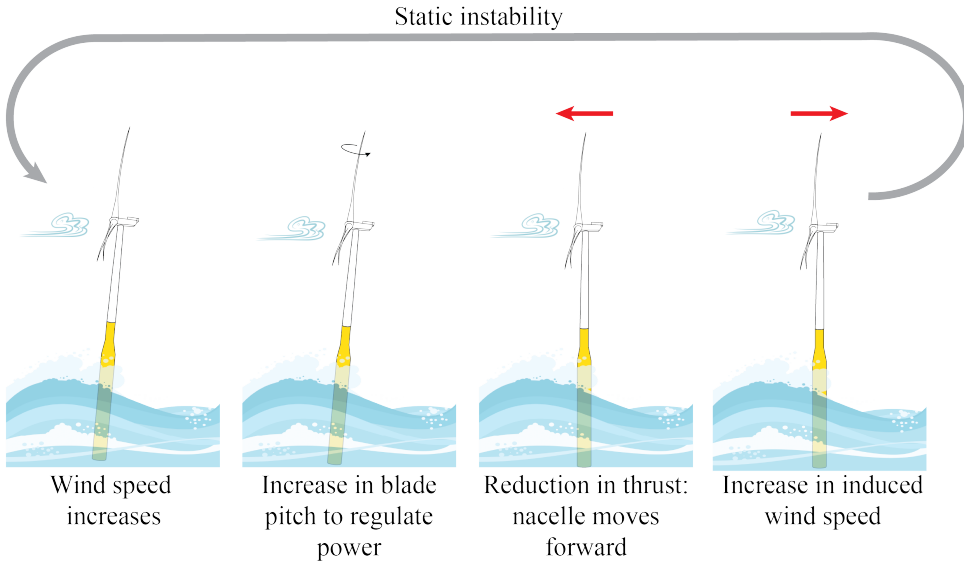


Figure 1.7: Illustration for the static instability caused by negative damping. Inspired from [63].

Apart from the instabilities that floating wind turbines encounter, they sustain additional wave-induced hydrodynamic loads. In control terminology, such environmental inputs are treated as exogenous disturbances. Current wind turbine control systems function in a reactive manner, with limited or no real-time awareness of the ambient flow and wave field. As a result, control actions are based solely on local measurements, without anticipation of upcoming disturbances [30, 31]. Enhancing the controller with preview capabilities or feedforward strategies informed by environmental sensing can significantly improve power regulation performance and mitigate fatigue loading, thereby enhancing overall system reliability and operational efficiency.

Analogous to LiDAR-based wind preview, wave-induced disturbances acting on floating wind turbines can be predicted using sensing technologies such as X-band radar, which provides insights on ocean wave characteristics before they reach the structure [70–72], as depicted in Fig. 1.8. Pioneered by the company Next Ocean [68], this technology has demonstrated a high level of operational maturity through several years of deployment in the maritime sector [73, 74]. Its proven reliability makes it a promising enabler for the implementation of wave feedforward control strategies in floating wind turbines. Figure 1.9 depicts the WavePredictor wave radar developed at Next Ocean [68] mounted on FLOATGEN floating wind turbine off the coast of Le Croisic in the offshore test site, SEM-REV, of École Centrale de Nantes in France [69].

Wave feedforward control is conceptually promising. However, it remains less mature than LiDAR feedforward control, mainly due to limited exploration in current literature. Some studies have explored the concept, including the development of a Nonlinear Model Predictive Control (NMPC) framework assuming perfect wind and wave previews, which showed promising improvements in blade load reduction relative to a standard feedback

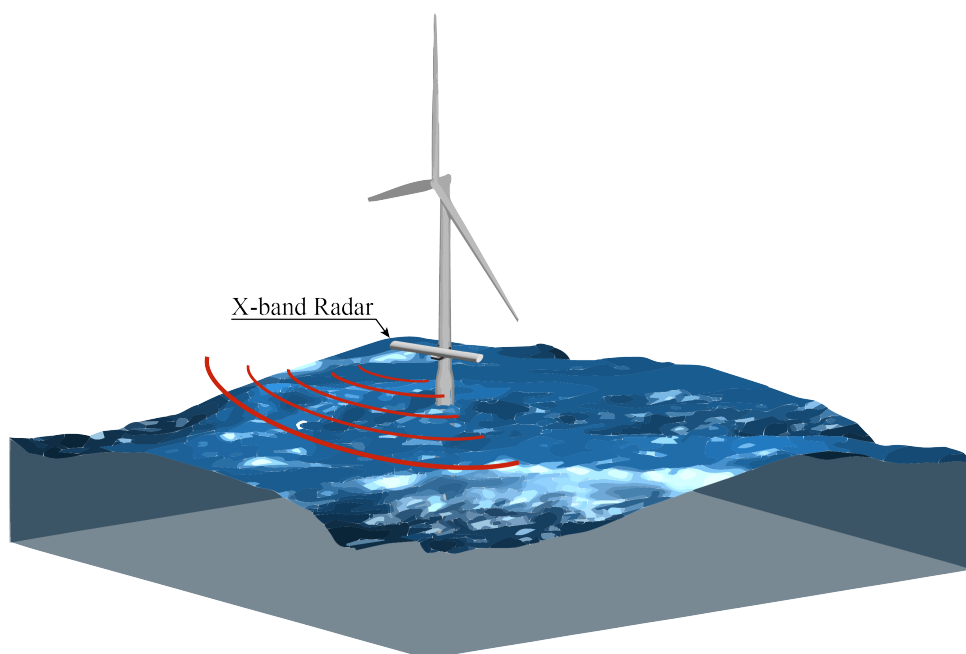


Figure 1.8: An illustration of the wave prediction technology for floating offshore wind turbines.

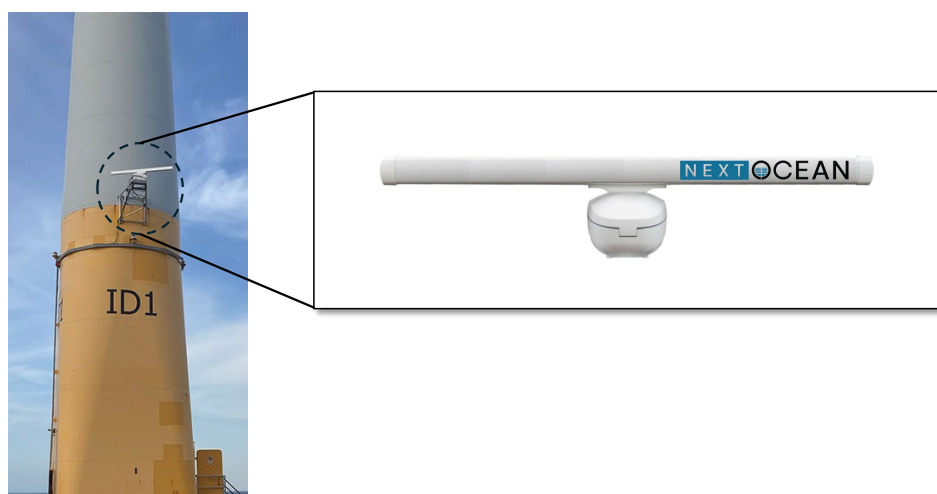


Figure 1.9: WavePredictor wave radar from Next Ocean [68] mounted on FLOATGEN floating wind turbine near Saint Nazaire in France [69].

controller, although the individual effects of the LiDAR and wave FF controllers were not isolated [55]. Another contribution presented a finite-horizon Linear Quadratic Regulator (LQR) exploiting real-time wave load forecasts to reduce tower base fore-aft bending moments, with varied results [51]. A model-inversion-based wave feedforward controller was also proposed using a preview of the incoming wave elevation to reduce rotor speed fluctuations. Integrated with a conventional feedback loop and focused on the dominant dynamics of the floating wind turbine, this strategy was shown to enhance power quality while simultaneously lowering fatigue loads in the low-speed shaft and blades [75, 76].

Nevertheless, the model-inversion-based feedforward control approaches are developed based on simplified representations of the Floating Offshore Wind Turbine (FOWT), accounting for only a limited number of degrees of freedom related to the system's global dynamics. Consequently, these methods overlook several critical aspects, including higher-order dynamic behaviour and the non-minimum phase characteristics introduced by the RHPZs in the plant. In contrast, data-driven control techniques offer the potential to capture these unmodelled dynamics that are typically neglected in model-based approaches. Among data-driven control techniques, direct data-driven control stands out by utilising input-output data collected from system sensors to generate future control commands without explicitly identifying a system model [77]. Recent studies have demonstrated the application of such methods in various contexts, including LiDAR feedforward control using Subspace Predictive Control (SPC) [78] and wave feedforward control using Data-Enabled Predictive Control (DeePC) [79].

While numerical simulations serve as a foundational tool for evaluating advanced control strategies, they are not sufficient on their own to elevate the associated Technology Readiness Level (TRL) [80]. Physical experiments play a crucial role in validating and complementing simulation results. In the domain of feedforward control technologies for wind turbines, full-scale field experiments have been successfully conducted to assess the performance of LiDAR feedforward control. These studies demonstrated its potential in improving power regulation and reducing structural loads [47, 52]. In contrast, although wave feedforward control shows similar conceptual promise, its experimental validation remains limited. The only reported experimental attempt did not yield conclusive results [81]. This highlights a clear gap in the empirical validation of wave feedforward control, underscoring the need for further investigation and robust experimental assessment.

1.5 Thesis objective and outline

Based on the challenges facing the control of floating wind turbines, outlined in the previous section, the main objective of this thesis is:

Thesis objective: The development of wave feedforward and multivariable feedback control architectures and design methodologies for floating wind turbines.

Achieving this objective entails addressing two distinct aspects. The first involves mitigating the additional loads imposed on the floating wind turbine by wave disturbances. When a preview of the incoming wave field is available, feedforward control strategies can be utilised to counteract these disturbances. The second part shifts focus to the feedback

control architecture for floating wind turbines, with particular emphasis on identifying and mitigating the fundamental limitations associated with controller performance in above-rated operating conditions (Region 3).

Starting with the first part, early research has predominantly employed model-based wave feedforward controllers developed from first-principles models. While effective in capturing the global dynamics of the system, these approaches often neglect important higher-order or localised dynamics. This limitation highlights the need for a complementary data-driven approach to improve model fidelity and control performance. Furthermore, existing implementations in the literature often utilise a single-point wave elevation preview, failing to represent the inherently multidirectional characteristics of real ocean waves. Consequently, the first contribution of this thesis is:

Contribution 1: Development of wave feedforward controllers for maximising power output and alleviating structural loads, relying on preview of wave excitation loads.

The first contribution of this work takes the form of a computational investigation conducted using a medium-fidelity simulation framework. While this provides valuable insight, the inherently nonlinear and intricate behavior of floating wind turbines places limitations on what such models can capture—particularly when compared to the richer dynamics observable in physical test environments like wave basins. To address this, the second contribution involves experimental validation through wave tank testing. These experiments not only confirm the numerical findings but also offer a more nuanced exploration of the capabilities and performance of the wave feedforward control technology. Accordingly, this second contribution is outlined as follows:

Contribution 2: Evaluation of wave feedforward control technology through conducting Software-In-the-Loop hybrid wave tank experiments.

Shifting to the second aspect, a fundamental limitation, set by non-minimum phase zeros, is holding the feedback collective pitch controller from reaching higher bandwidths during power regulation. Subsequently, the generator power signal experiences more oscillations in the process. Several research works reflected on this limitation, and different solutions addressing the problem were proposed as a result. However, most of the solutions required additional sensors in the system, which might reduce the robustness of the control framework in case of a faulty sensor. Therefore, this takes us to the third contribution:

Contribution 3: Introduction of a novel control architecture aimed at alleviating the bandwidth limitations inherent in feedback control of floating wind turbines, without the need for additional sensor instrumentation.

Expanding on the novel solution proposed to mitigate the negative damping instability in the third contribution, this work further establishes a dedicated control architecture along with a systematic tuning methodology tailored for the newly introduced feedback controller. Accordingly, the final contribution of this thesis is formulated as:

Contribution 4: Formulation of systematic tuning methodologies for several feedback control architectures tailored to floating wind turbines.

With these four contributions, this thesis aims to aid in developing the feedback and feedforward control for floating wind turbines, thereby achieving the goal of this thesis as specified at the beginning of this section.

Thesis Outline

This thesis comprises six chapters, with the first being the current introduction chapter. The subsequent four chapters are practically duplicates of scientific articles, and therefore, each contains its own introduction and conclusions. These chapters showcase the contributions of this work in the same order as mentioned in the previous chapter.

Chapter 2 presents the development of a wave feedforward control framework aimed at regulating generator speed and alleviating platform pitch motion. The effectiveness of the proposed control strategies is evaluated through non-linear time-domain simulations. This chapter builds upon the findings presented in the following publication:

A. Hegazy, P. Naaijen and J.W. van Wingerden. Wave Feedforward Control for Large Floating Wind Turbines. IEEE Conference on Control Technology and Applications (CCTA), Bridgetown, Barbados, 2023.

Chapter 3 explores the potential of wave feedforward control strategy experimentally, based on the wave feedforward controllers developed in Chapter 2, by conducting scaled-model testing in a wave tank. Moreover, it investigates the performance of the developed controllers under different environmental conditions. The chapter is based on the following publication:

A. Hegazy, P. Naaijen, V. Leroy, F. Bonnefoy, M.R. Mojallizadeh, Y. Pérignon, and J.W. van Wingerden. The potential of wave feedforward control for floating wind turbines: a wave tank experiment. *Wind Energy Science*, 9:1669–1688, 2024.

Chapter 4 shifts the focus to the feedback control of floating wind turbines, with particular emphasis on the challenges posed by negative damping instability and its impact on feedback controller performance in the above-rated wind speed regime. It introduces a novel control architecture tailored for this operational region. The content of this chapter is derived from the following publication:

A. Hegazy, P. Naaijen, J.W. van Wingerden. A novel control architecture for floating wind turbines. International Federation of Automatic Control (IFAC) World Congress, Yokohama, Japan, IFAC-PapersOnline, Volume 56, Issue 2, Pages 7644–7649, 2023.

Chapter 5 serves as a tutorial on the design of closed-loop control systems for floating wind turbines, presenting an overview of various control strategies proposed in the literature. The chapter critically evaluates the performance of these strategies, with a particular emphasis on their effectiveness in mitigating negative damping instability. Furthermore, the novel controller structure introduced in Chapter 4 is revisited, providing a detailed

explanation of its tuning procedure. The content of this chapter is based on the following publication:

A. Hegazy, P. Naaijen, and J.W. van Wingerden. Control design for floating wind turbines. *Wind Energy Science Discussions*, in review, 2025.


Chapter 6 consolidates the overarching conclusions drawn from the preceding chapters and offers recommendations for future research.

2

Wave Feedforward Control for Large Floating Wind Turbines

Floating wind energy has attracted substantial interest since it enables the deployment of renewable wind energy in deeper waters. However, floating wind turbines are subjected to disturbances, predominantly from turbulence in the wind and waves hitting the platform. Wave disturbances cause undesired oscillations in rotor speed and increase structural loading. This paper focuses on mitigating these disturbance effects with feedforward control using knowledge of the incoming wavefield. The control problem is formulated in an \mathcal{H}_∞ optimisation framework, designing two wave feedforward controllers: one to reduce rotor speed oscillations and the other one to minimise the platform pitch motion. Mid-fidelity time-domain simulations demonstrate the improved performance of the proposed control algorithm regarding wave disturbance mitigation at the cost of higher actuator duty.

This chapter is based on:

 A. Hegazy, P. Naaijen and J.W. van Wingerden, "Wave Feedforward Control for Large Floating Wind Turbines", 2023 IEEE Conference on Control Technology and Applications (CCTA), Bridgetown, Barbados, 2023, pp. 593-598, doi: 10.1109/CCTA54093.2023.10252529.

2.1 Introduction

Driven by the European Commission's ambition of becoming a climate-neutral continent by 2050, wind energy is the technology expected to provide the largest contribution to the EU renewable energy targets [82].

Despite the advantages offshore wind energy offers, it is more challenging due to the rough environmental operating conditions where offshore wind turbines operate. Especially with waves added to the disturbances affecting the wind turbine and exerting extra structural loading on top of the loads due to wind turbulence. Waves contribute to the fatigue loads experienced by the floating offshore wind turbines (FOWTs). From a control perspective, FOWTs are harder to control than their onshore counterpart. That is due to the extra dynamics introduced by the floating platform and the well-known negative damping instability forcing a reduction in the bandwidth of the feedback pitch controller below the platform pitch eigenfrequency [83]. Consequently, the control authority of the blade pitch feedback controller against errors occurring due to disturbances such as wind and waves becomes limited. Regarding wind turbulence, LiDAR FeedForward (FF) control, which is based on providing a preview of the upstream wind field to be included in the turbine controller, has been the main focus of feedforward control in wind turbines, as it proved to reduce fatigue loads and power excursions effectively [48, 53].

Wave FF control strategy resembles LiDAR FF control; as in the case of wave FF, a preview of the wave height/loads is also required to be exploited within the turbine controller. In this regard, several technologies are available to measure the surface wave elevation as wave buoys, radars, or satellites. The radar technology, in particular, is attractive because of its capability to scan large areas at further distances [76]. Radar images of the wave field can then be used to obtain predictions of the surface wave elevation as in [71]. Wave FF, however, is not discussed in the literature as thoroughly yet. Only a few studies investigated the subject as in [55], where a Non-linear Model Predictive Control (NMPC) strategy was developed, considering perfect wind/wave preview, demonstrating promising improvement over the baseline feedback controller with regard to blade loads. In [51], an effective deterministic finite-horizon LQR controller was designed, exploiting a real-time forecast of the wave loads to reduce tower-base fore-aft (FA) bending moment, and achieved assorted results. An inversion-based wave FF controller was developed in [75, 76] utilizing a preview of the incoming wave elevation, where the FF controller was added to the standard feedback (FB) controller to refine power quality by reducing the rotor speed fluctuations caused by waves. The controller effectively alleviates the effects of the wave disturbance, decreasing rotor speed excursions with a positive side-effect of lowering the fatigue loads for the Low-Speed Shaft (LSS) and blades. However, the model-based inverted FF controller in [75, 76] only considers a few degrees of freedom corresponding to the global dynamics of the FOWT, which means that it lacks extra modes, in addition to other missing elements, namely the non-minimum phase behaviour arising from the Right-Half Plane Zeros (RHPZs) in the plant model. In this paper, two wave FF controllers are developed; one for alleviating the rotor speed oscillations for power regulation (FF- ω), and the other for mitigating the platform pitch motion for load minimisation (FF- θ_p).

Unlike the model-based control used in [75, 76] for the control synthesis, the data-driven control approach can capture the unknown dynamics unconsidered in the model-based. Therefore, it was adopted in this paper using the Predictor-Based Subspace Identification

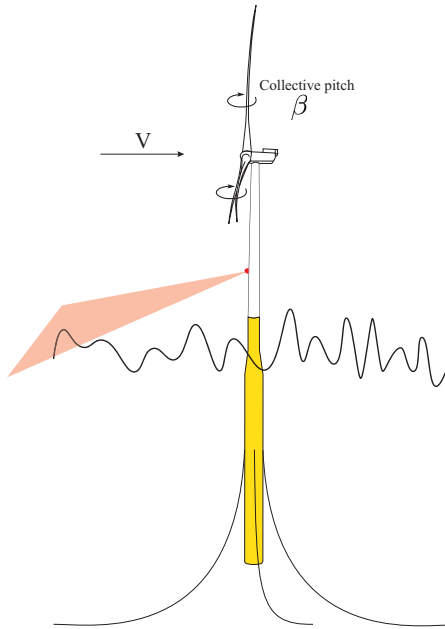


Figure 2.1: Schematic of the wave feedforward control strategy. The feedforward control action is based on the wave elevation measured by a radar upstream of the wind turbine. This measurement is used to obtain a preview of the wave excitation forces at the floating platform ahead of time, which is the input to the wave feedforward controller.

(PBSID_{opt}) algorithm [84]. The main contributions of this paper are threefold:

- A linear model of a FOWT, with blade pitch control input and wave excitation forces as disturbance input, is identified using PBSID_{opt} method.
- Two wave forward controllers are synthesized for the objectives of power regulation and load mitigation.
- The performance of the developed controllers is then assessed in the mid-fidelity time-domain simulation tool, QBlade [85].

This paper is structured as follows: Section 2.2 describes the problem, together with all the requirements for control synthesis. Afterwards, the control design procedure is discussed in Section 2.3. The developed controllers are then tested in a mid-fidelity simulation environment in Section 2.4. Finally, Section 2.5 will draw the conclusion.

2.2 Floating Wind Turbine Description

In this section, the FOWT model is given, and a description of the estimation and identification procedures used to obtain the linear model used for the control design is explained.

2.2.1 Floating Wind turbine Model

For this study, the DTU 10 MW Reference Wind Turbine (RWT) [86] atop a spar floating platform [87] within the context of the SOFTWIND project [88]. The parameters of both the DTU 10 MW RWT and the floating platform are shown in Table 2.1 and Table 2.2, respectively.

Table 2.1: Parameters of the DTU 10 MW RWT [86].

Parameter	Value
Cut-in wind speed	4 [m/s]
Cut-out wind speed	25 [m/s]
Rated wind speed	11.4 [m/s]
Rated power	10 [MW]
Peak power coefficient	0.48 [-]
Optimal tip speed ratio	7.55 [-]
Rotor diameter	178.3 [m]
Hub Height	119 [m]
Minimum rotor speed	6 [rpm]
Maximum rotor speed	9.6 [rpm]
Rotor mass	227,962 [kg]
Nacelle mass	446,036 [kg]
Tower mass	628,442 [kg]

Table 2.2: Parameters of the SOFTWIND spar platform [87].

Parameter	Value
Platform mass	$1.94 \times 10^7 [kg]$
Roll inertia about CoG FOWT	$10^{10} [kg.m^2]$
Pitch inertia about CoG FOWT	$10^{10} [kg.m^2]$
Yaw inertia about CoG FOWT	$6 \times 10^8 [kg.m^2]$
Draft	90 [m]
Platform diameter	18 [m]

Fig. 2.2 shows a block diagram of the FOWT model and control signals. Each block represents a linear Transfer Function (TF). The tilting wave moments are represented by M_w . G_{θ_p, M_w} is mapping from, M_w , to the platform pitch motion, θ_p , the effect of wave moments on the generator speed, ω_g . Similar to the wave moment, the effect of blade pitch on generator speed and platform pitch motion is described by the TFs $G_{\omega_g, \beta}$ and $G_{\theta_p, \beta}$, respectively.

To obtain these TFs, which are required for the control design, identification is conducted on the results obtained from QBlade [85]. QBlade is a fully coupled, non-linear, aero-hydro-servo-elastic wind turbine simulation suite that is capable of simulating wind

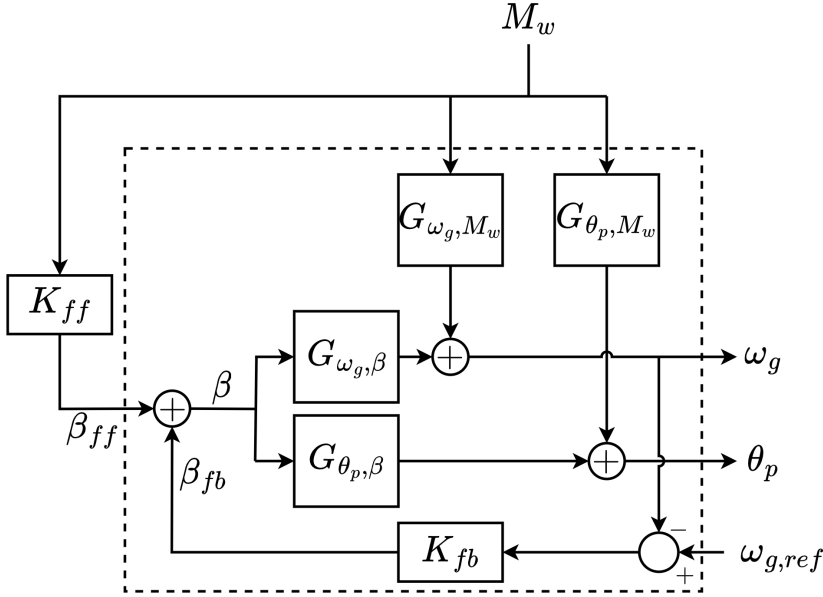


Figure 2.2: Block diagram of the closed-loop floating wind turbine model, where the FB controller is embedded within the model, with the relevant blocks and signals required for the identification.

turbines with a good level of accuracy. System identification is required when using QBlade for control design purposes, as it is not equipped with a linearization functionality, thus making it complicated to do model-based control.

2.2.2 Spectral Estimation and Identification

This work was done at an average wind speed of 16 [m/s] as an operating point. A similar procedure was used for both the estimation and the identification, where an experiment of a duration of 25000 [s] was held in QBlade.

To get the TFs $G_{\omega_g, \beta}(s)$ and $G_{\theta_p, \beta}(s)$, a chirp signal, logarithmically distributed over the experiment's duration, was used to excite β within a frequency band (0.02 to 0.3 Hz). As for $G_{\omega_g, M_w}(s)$ and $G_{\theta_p, M_w}(s)$, a JONSWAP spectrum was used.

From input-output data, spectral estimation can be employed to get the above-mentioned TFs in a non-parametric form. A frequency response function (FRF), assuming no correlation between the input and noise signals, can be achieved according to:

$$G_{y,u}(j\omega) = \frac{S_{yu}(j\omega)}{S_{uu}(j\omega)}, \quad (2.1)$$

where ω in (3.3) denotes the frequency, $j = \sqrt{-1}$, while $S_{yu}(j\omega)$ is the cross-spectral density of the output and input, $S_{uu}(j\omega)$ is the power spectral density of the input, and $G_{y,u}(j\omega)$ represents the estimated FRF. Based on the estimated frequency response functions and the feedforward structure given in Fig. 2.2 the optimal non-parametric feedforward controller

for generator speed control and tower top control can be estimated and are respectively given by:

$$\begin{aligned} K_{ff,\omega}(j\omega) &= -\frac{G_{\omega_g,M_w}(j\omega)}{G_{\omega_g,\beta}(j\omega)}, \\ K_{ff,\theta_p}(j\omega) &= -\frac{G_{\theta_p,M_w}(j\omega)}{G_{\theta_p,\beta}(j\omega)}. \end{aligned} \quad (2.2)$$

The optimal non-parametric controllers are given by the blue lines in Fig. 2.4 and Fig. 2.5, respectively.

So far, the controllers given in Eq. (2.2) are non-parametric since FRFs were used. However, they cannot be used for control implementation. Therefore, identification using PDSID_{opt} was conducted to obtain linear models, since QBlade lacks the linearisation functionality as previously mentioned. More details about PDSID_{opt} algorithm can be found in [84].

2.3 Controller Design

For control design, the \mathcal{H}_∞ framework is used. Therefore, first, we start by introducing the \mathcal{H}_∞ problem set-up before defining the generalized plant for the control synthesis, in addition to the performance weights required. Normally, the order of the synthesized \mathcal{H}_∞ controllers is equal to that of the plant model. Subsequently, if the plant model is of a high order, the \mathcal{H}_∞ would be high too, which makes its implementation complicated. Accordingly, lower-order controllers with fixed-structure are employed instead, with the \mathcal{H}_∞ controllers used as reference. Finally, both the \mathcal{H}_∞ and the parametric reduced-order controllers, are then compared with the non-parametric optimal FF controller obtained from the spectral estimation from section 2.2.

The objective of formulating the control problem in the \mathcal{H}_∞ framework is to minimize the \mathcal{H}_∞ norm of the TF from the exogenous inputs, w , to performance outputs, z [89]. The controller synthesis problem is then to find a controller K_{ff} that minimizes the infinity norm of the closed-loop TF, $\|N\|_\infty < 1$.

The generalized plant, P , used for the control synthesis is shown in Fig. 2.3. The exogenous input, w , considered is the wave moment, M_w , while two performance signals, z_1 and z_2 , are specified. Signal z_1 represents the weighted response penalized by the weight W_p to reduce the effect of M_w , while z_2 is the weighted control action penalized by the weight W_u to bound the actuator limits. Signals v and u represent the control input (M_w) and the control action (β), respectively. As for G and G_d , they are defined based on the control objective. For FF- ω , $G = G_{\omega_g,\beta}$ and $G_d = G_{\omega_g,M_w}$, while for FF- θ_p , $G = G_{\theta_p,\beta}$ and $G_d = G_{\theta_p,M_w}$.

$W_p(s)$ is chosen to get a slope of 20 dB/dec in $|S|$ for the low frequency region as follows

$$W_p(s) = \frac{s/M + \omega_B}{s + A\omega_B}, \quad (2.3)$$

with ω_B as the desired closed-loop bandwidth, A is the desired disturbance attenuation within the closed-loop bandwidth, and M is the desired bound on the sensitivity margin [89]. The controller sensitivity is penalized at high frequencies by W_u , which was considered constant in this work.

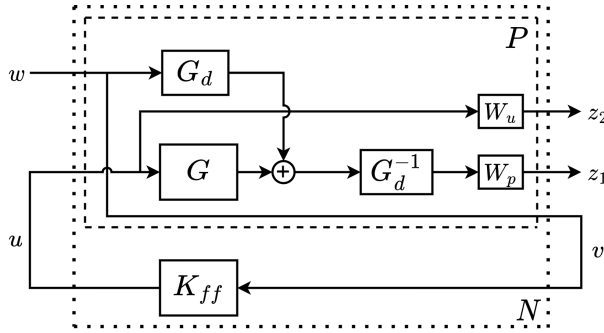


Figure 2.3: Generalized plant with the performance weights

The controller is designed that based on v , a control signal, u , is generated to counteract the influence of w , on z , by minimizing the weighted \mathcal{H}_∞ norm of the closed-loop TFs, N , from w to z_1 and z_2 :

$$N(s) = \begin{bmatrix} W_p \left(I + G_d^{-1} G K_{ff} \right) \\ W_u K_{ff} \end{bmatrix}, \quad (2.4)$$

where the FF controller sensitivity function is defined as:

$$S_{ff}(s) = \left(I + G_d^{-1} G K_{ff} \right). \quad (2.5)$$

S_{ff} gives an indication about the effectiveness of the FF controller can be evaluated in the frequency domain, as it shows that the undesirable effect of the exogenous input, w , altering the exogenous output, z_1 , can be totally cancelled out or at least mitigated to some extent by the inclusion of the FF controller, K_{ff} , as demonstrated in Eq. (2.5). In theory, perfect disturbance cancellation can be achieved by substituting K_{ff} in Eq. (2.4) with the FF controllers in Eq. (2.2), N_1 becomes zero, indicating that $S_{ff} = 0$, and that perfect disturbance rejection has been achieved.

$$z_{1,noFF} = G_d w \quad (2.6)$$

$$z_{1,FF} = W_p \left(I + G_d^{-1} G K_{ff} \right) w \quad (2.7)$$

$$\frac{z_{1,FF}}{z_{1,noFF}} = \frac{W_p \left(I + G_d^{-1} G K_{ff} \right)}{G_d} \quad (2.8)$$

Equations (2.6) and (2.7) show the disturbance signal transfer to the output signal in the absence and the presence of the FF controller, respectively, Eq. (2.8) compares both responses. It can clearly be seen how K_{ff} is able to alleviate the effects of w on z_1 when that ratio in Eq. (2.8) is less than unity.

The wave FF controller, K_{ff} , can then be obtained via the minimisation of the mixed-sensitivity problem with respect to K_{ff} :

$$\min_{K_{ff}} \|N\|_{\infty}. \quad (2.9)$$

Following the control synthesis, the high-order \mathcal{H}_{∞} controllers are reduced by fitting fixed-structure, lower-order controllers, as shown for both generator speed and platform pitch motion in Fig. 2.4 and Fig. 2.5, respectively. The parametric FF- ω controller is then given as:

$$K_{ff,\omega}(s) = \frac{K_{\omega}}{s^2} \frac{\tau s + 1}{s^2 + 2\zeta\omega s + \omega^2}, \quad (2.10)$$

while the parametric FF- θ_p controller, can either be a static gain, K_{θ_p} , or a dynamic controller expressed as:

$$K_{ff,\theta_p}(s) = \frac{K_{\theta_p} s^2}{s^2 + 2\zeta\omega s + \omega^2}, \quad (2.11)$$

where K_{ω} and K_{θ_p} are constants used for scaling the controller gain, τ is a time constant, ζ is the damping ratio, and ω is the natural frequency.

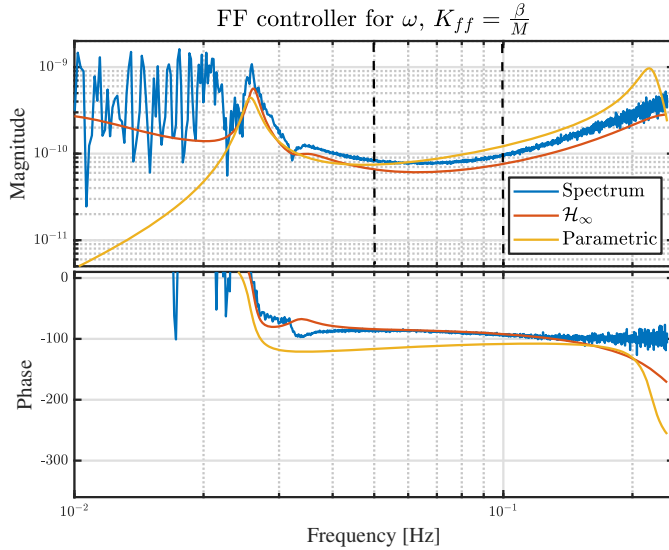


Figure 2.4: Bode plot of the optimal feedforward controller that targets the high-speed shaft rotor speed. Blue: spectral estimate, Red: \mathcal{H}_{∞} control, Yellow: parametric controller.

Fig. 2.4 and Fig. 2.5 show a good agreement between the non-parametric optimal FF controller and the \mathcal{H}_{∞} controller within the frequency band of interest enclosed by the dashed vertical lines.

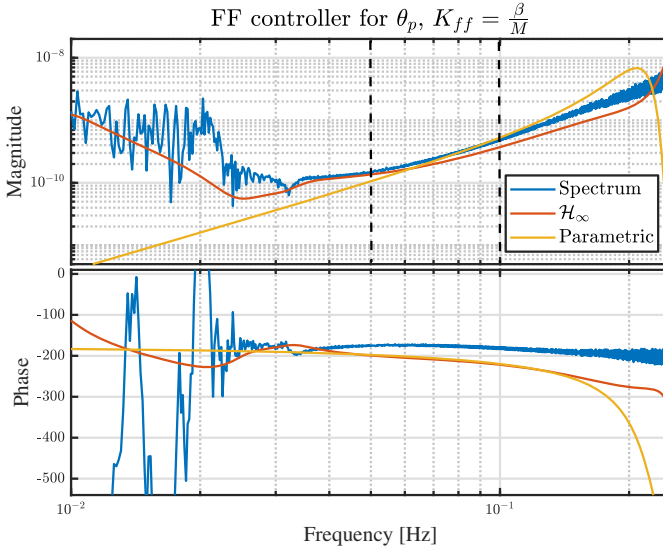


Figure 2.5: Bode plot of the optimal feedforward controller that targets the platform pitch. Blue: spectral estimate, Red: \mathcal{H}_∞ control, Yellow: parametric controller.

Additionally, it is important to mention that the synthesised \mathcal{H}_∞ controllers are, by definition, stable because the internal stability of the feedback system, with the baseline FB controller, is guaranteed. Furthermore, the \mathcal{H}_∞ formulation ensures producing stable FF controllers, unlike the model-inversion FF controllers [75, 76], which would require adding extra elements to the inverted controller to make it stable, in case of non-minimum phase systems comprising RHPZs [83] inverted to become unstable poles.

2.4 Results

In this section, the parametric controller is assessed in mid-fidelity time-domain simulations, using the linear models developed in section 2.2.

The synthesised controllers were augmented to the baseline FB controller, and their performance, under the normal operating environmental conditions of wind and waves, is compared to the normal baseline FB control. Additionally, the effect of each of the wind and wave disturbances is shown separately in the absence of the other to show the frequency band where each disturbance exists. Wind disturbances are less frequent compared to wave disturbances, implying that wind dominates in the low-frequency range, while its dominance diminishes as frequency increases where waves become more dominant. This observation is supported by the power spectra in Fig. 2.7.

The power spectral density (PSD) spotlights the frequency band ranging up to 0.3 Hz, which is the linear wave range (0.05 – 0.3 Hz), where the wave FF controllers are active, reacting only to wave disturbance, while having no effect at lower frequencies.

The feedforward controller for rotor speed regulation (FF- ω) is designed to mitigate wave-induced variations. This is demonstrated by the FBFF- ω controller that evidently

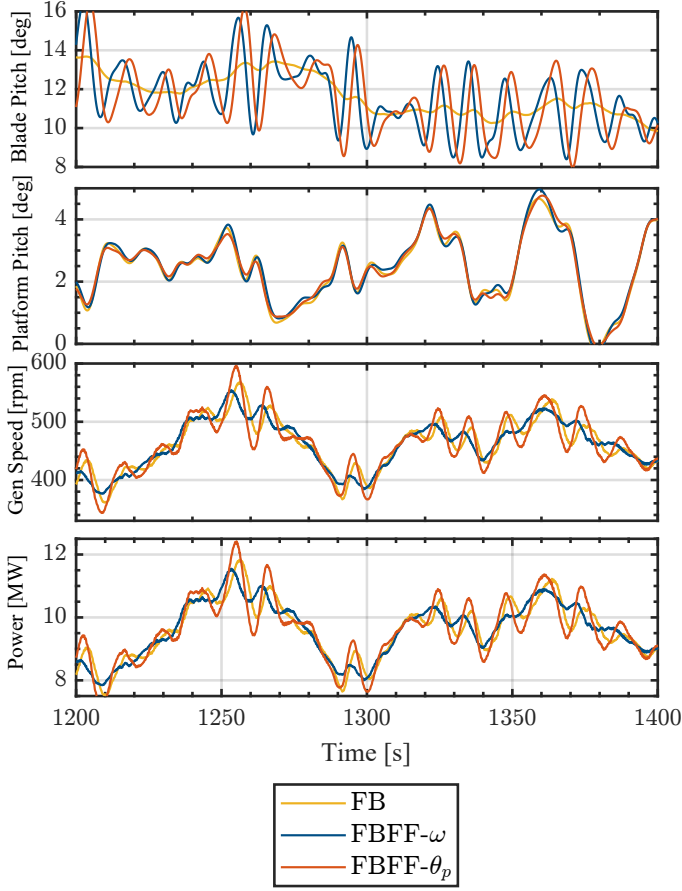


Figure 2.6: Time series of the blade pitch, platform pitch, generator speed and power at 16 m/s turbulent wind.

alleviates the fluctuations in the generator speed, which in return reduces the oscillations in the generator power as shown in Fig. 2.6. This is illustrated in the PSD in Fig. 2.7 where the energy content of the generator speed, as well as the power, are decreased within the wave frequency range below the normal FB operating condition with both wind and waves. The energy content of both the blade pitch actuation and platform pitch, on the other hand, increases indicating more oscillations in these channels, which is clearly manifested in Fig. 2.6.

While the feedforward controller for load minimisation (FF- θ_p), on the other hand, is designed to reduce the oscillations of the rigid body platform pitch motion, which is illustrated by the FBFF- θ_p controller as the addition of the FF- θ_p control to the FB control counteracts the wave-induced platform pitch motion, and slightly reduces the platform pitch motion. However, this comes at the expense of increasing the blade pitch command, rotor speed and power excursions, as shown in Fig. 2.6. This is highlighted in the PSD in Fig. 2.7 where the energy content of the platform pitch is reduced, while that of the

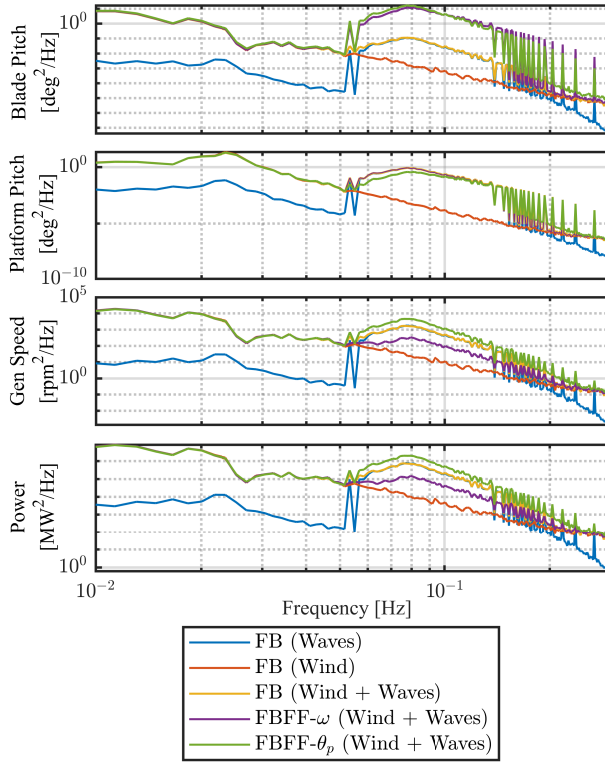


Figure 2.7: Power spectral density of the blade pitch, platform pitch, generator speed and power at 16 m/s turbulent wind.

blade pitch, the generator speed and the power increased above the normal FB operating condition with both wind and waves.

Both FF controllers modify the blade pitch command to meet their control objective, which is lower fluctuations in either the rotor speed or platform pitch motion for speed regulation and load minimization, respectively. According to Fig. 2.6 and Fig. 2.7, they are opposing each other even though their respective blade pitch commands are nearly the same. Yet, this opposing action is due to the phase difference between the two signals. This makes achieving both control objectives at the same time challenging.

Regarding fatigue loading, the performance of the FF controllers is assessed by means of computing the variance of some signals while conducting damage equivalent load (DEL) analysis based on the rainflow counting technique for others. DEL was computed for the FB with both wind and waves acting separately and combined to show the distinct effect of each of them independently, while for FBFF- ω and FBFF- θ_p , the combined wind and waves

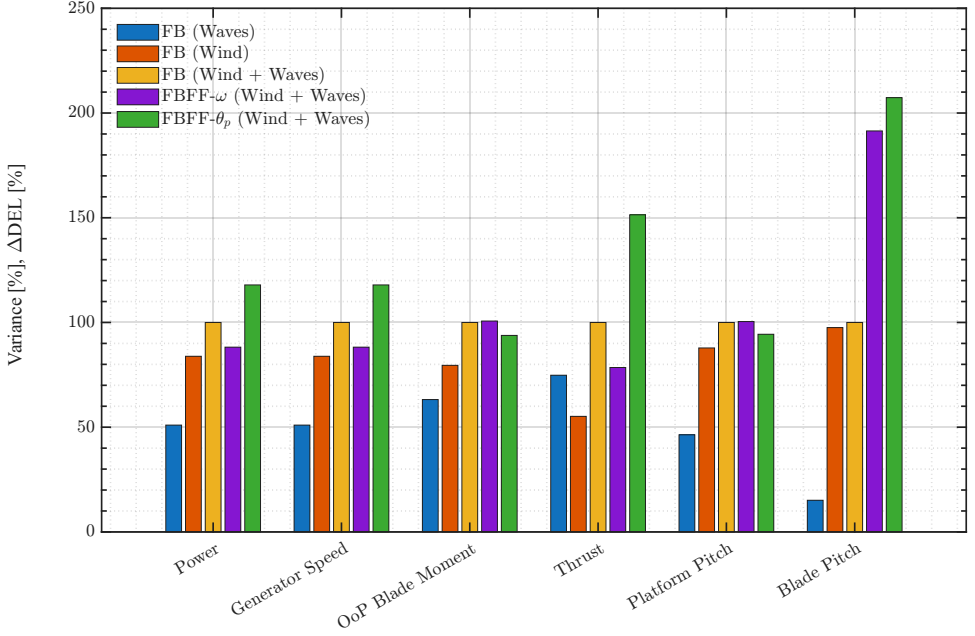


Figure 2.8: Damage equivalent load and variance of different outputs in different scenarios for the feedback controller and the combined feedback-feedforward controllers normalised by the feedback controller [FB (Wind + Waves)].

scenario was considered as Fig. 2.8 shows. It is clear that wind contributes more to the fatigue loads than waves except for thrust force, which is reasonable since the waves cause continuous variation in the relative wind speed seen by the rotor, thus, the rotor thrust varies as a result.

As for FF- ω , the wave FF controller reduces the rotor thrust force. Blade pitch command increases due to the extra blade pitching from the wave-FF. As a result, the rotor thrust force is decreased, leading to less DEL. The effect of the FF- ω on the platform pitch motions and the blade-out-of-plane bending fatigue damage is almost insignificant, while the blade pitch variation increases by nearly double over the normal FB case, indicating more fatigue damage experienced by the pitch actuator.

Concerning FF- θ_p , the wave FF controller is very efficient at reducing the rigid body platform pitch mode, hence, the tower-top FA motion. This curtailment in the platform pitch motion leads to a lower blade-out-of-plane bending fatigue damage, whereas the blade pitch actuator is heavily loaded even more than in the FF- ω case, which causes a significant increase in the rotor thrust. By means of linear analysis, this increase in the thrust force can be explained, as according to [90] there exists an anti-resonance peak at the platform pitch eigenfrequency in the TF from blade pitch to thrust, which a resonance peak at the same frequency in the TF from the blade pitch to the tower top FA displacement.

2.5 Conclusions

In this paper, a feedforward control strategy was developed with the aim of reducing the wave disturbance on floating wind turbines. Two feedforward controllers were designed using the H_∞ framework; the objective of the first one was power regulation through mitigating the wave-induced generator speed fluctuations, while the objective of the second is load minimisation by alleviating the platform pitch motion. To accomplish these objectives, linear models of the floating wind turbine were identified using the $PBSID_{opt}$ algorithm. Then, they were implemented within a generalized plant and employed in the H_∞ control synthesis. Subsequently, the H_∞ controllers were parameterised into fixed-structure lower-order controllers. The feedforward controllers were designed for the DTU 10MW reference wind turbine on top of a spar floating platform developed within the SOFTWIND project.

Time-domain simulations were then conducted in QBlade to evaluate the feedforward control strategy benefits in terms of structural loads and power quality for the floating wind turbine components. It was found that the feedforward controller for rotor speed reduces the power fluctuations, while the one for platform pitch motion reduces the OoP blade loads associated with wave excitation. The proposed feedforward control strategy does not require modifying the industry-standard feedback controller. It requires a forecast of the incoming waves, which is feasible to get with technologies that are already used in the maritime industry, and this is to be integrated into the wind turbine control system.

3

The Potential of Wave Feedforward Control For Floating Wind Turbines: A Wave Tank Experiment

Floating wind energy has attracted substantial interest since it enables the deployment of renewable wind energy in deeper waters. Compared to bottom-fixed turbines, floating wind turbines are subjected to more disturbances, predominantly from waves acting on the platform. Wave disturbances cause undesired oscillations in rotor speed and increase structural loading. This work focuses on investigating the potential of using wave preview measurement in the control system labelled as wave feedforward to mitigate the effects of wave disturbances. Two wave feedforward controllers were designed: one to reduce generator power oscillations and the other one to minimise the platform pitch motion. In this study, a software-in-the-loop wave tank experiment is presented to investigate the potential of these wave feedforward controllers. The experiment uses a 1:40 scaled model of the DTU 10 MW reference wind turbine on top of a spar platform with the baseline feedback control functionalities. Different environmental conditions, including wind speed, significant wave height, turbulence intensity and wave spreading, were applied during the experiments to test the feedforward control performance and their effect on the turbine dynamics in general. It was found that the feedforward controller for the generator power reduced the power fluctuations properly with a fair control effort, while the one for platform pitch motion required almost double the actuation duty for the same percentage reduction. Furthermore, the feedforward controller could counteract the wave disturbance at different wave heights and directions. However, it could not do much with increasing turbulence intensity as wind turbulence was found to have more dominance on the global dynamic response than waves.

This chapter is based on:

📄 A. Hegazy, P. Naaijen, V. Leroy, F. Bonnefoy, M.R. Mojallizadeh, Y. Pérignon, and J.W. van Wingerden: The potential of wave feedforward control for floating wind turbines: a wave tank experiment, *Wind Energy Science*, 9, 1669–1688, doi: 10.5194/wes-9-1669-2024.

3.1 Introduction

Wind energy is pivotal for meeting the decarbonisation objectives of the European Union (EU) energy system, as it ensures delivering clean, affordable and secure electricity to various sectors, including households, industry and transport. Consequently, wind energy is expected to contribute heavily to the EU's renewable energy targets. This is not surprising, especially when we know that in 2022, wind energy covered 16% of the EU electricity demand and accounted for over 37% of the total electricity generated from renewable sources in the EU in 2021. No wonder the EU is regarded as a pioneer in wind energy. Accordingly, this has seen the EU revising the renewable energy directive, which lays down a minimum binding target of 42.5% share of renewables by 2030 with an aspiration to reach 45%. This is 10.5% higher than the initial 32% target. Subsequently, the EU could fulfil its ambition of becoming climate-neutral by 2050 [82].

Offshore wind is quite superior to onshore wind when it comes to higher wind speeds and consistency in direction. Floating offshore wind, in particular, offers unique opportunities for Europe, as FOWTs can produce electricity further offshore and in deeper waters than bottom-fixed turbines, which opens the door for offshore wind development in countries with deeper sea basins, such as the Mediterranean and Atlantic. Nevertheless, floating offshore wind turbines operate in rough environmental conditions. As opposed to onshore turbines, waves come into play and act as another source of disturbances affecting the wind turbine, exerting extra structural loading on top of the loads due to wind turbulence. Consequently, fatigue loads experienced by FOWTs are increased due to the contribution added by the waves [91]. FOWTs come with additional challenges compared to their onshore counterpart from a control point of view, as extra dynamics introduced by the floating platform make the control problem more complex. A well-known example is the negative damping instability that forces a reduction in the bandwidth of the Feedback (FB) pitch controller below the platform pitch eigenfrequency [39, 40, 60, 63, 65, 83]. Consequently, the blade pitch FB controller has limited control over errors caused by disturbances like wind and waves, leading to a delayed response in control actions to these disturbances. As mentioned before, wind and waves are the main sources of disturbance affecting FOWTs. If a preview of those disturbances exists, it can be exploited within a Feedforward (FF) control framework to combat their effects. This would reduce the control effort exerted by the FB controller, as it would not need to react to disturbances anymore since the FF would be taking care of them. As for wind disturbance, nacelle-mounted Light Detection And Ranging (LiDAR) technology can provide measurements of the upstream wind inflow, from which an estimate of the rotor-effective wind speed is obtained, which can be used for FF wind turbine control. LiDAR FF control has proven its ability to reduce fatigue loads and power excursions effectively [48, 53, 54], which helped boost its momentum towards commercialisation.

Generally speaking, wave FF control strategy resembles LiDAR FF control, as in the case of wave FF, a preview of the wave height/loads is acquired based on measurements of the surrounding upstream waves, as shown in Fig. 5.1, which is then exploited within the turbine controller. In this regard, several technologies are available to measure the surface wave elevation, such as wave buoys, radars, or satellites. The radar technology, in particular, has the capability of scanning large areas at further distances, which makes it attractive [76]. Predictions of the surface wave elevation can then be established from the radar images

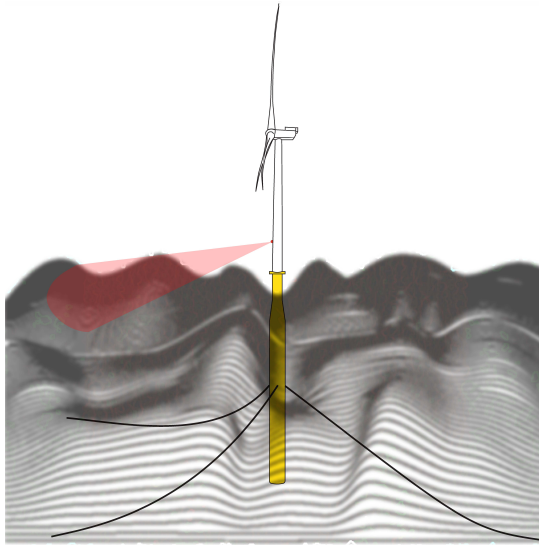


Figure 3.1: Schematic of the wave FF control strategy. The FF control action is based on the wave elevation measured by a radar upstream of the wind turbine. This measurement is used to obtain a preview of the wave excitation forces at the floating platform ahead of time, which is the input to the wave FF controller.

of the wave field [71]. A phase-resolved ocean wave prediction algorithm was developed in [92] to incorporate directional sea states and validated them against dedicated scaled wave tank experiments, considering sea states with different directional spreading as well as different wave steepness. Later on, they continued the development of the prediction algorithms with the aim of enhancing the accuracy of continuous wave prediction, as discussed in [93]. Furthermore, wave excitation force prediction methods were proposed in [94], where they validated the prediction algorithms against the experimental data.

Wave FF, however, is not yet as mature as LiDAR FF since it is not thoroughly discussed in the literature. Only a few studies investigated the subject as in [55] where a Non-linear Model Predictive Control (NMPC) strategy was developed, considering perfect wind/wave preview, demonstrating promising improvement over the baseline feedback controller with regard to blade loads, but the contribution of each of the LiDAR and wave FF separately was not clarified. In [51], an effective deterministic finite-horizon LQR controller was designed, exploiting a real-time forecast of the wave loads to reduce tower-base fore-aft (FA) bending moment, and achieved assorted results. A model-inversion wave FF controller utilizing a preview of the incoming wave elevation, with the objective of reducing rotor speed oscillations, was developed in [75, 76] considering a few degrees of freedom corresponding to the global dynamics of the FOWT, where the FF controller was added to the standard FB controller to improve power quality by reducing the rotor speed fluctuations caused by waves. They showed that the controller could alleviate the effects of the wave disturbance on the rotor speed, hence, the generator power, with a positive side-effect of lowering the fatigue loads for the Low-Speed Shaft (LSS) and blades.

Unlike the model-based control used in [75, 76] for the control synthesis, a data-driven

control approach, which can capture the missing dynamics that are not considered in the model-based one, was employed in [95]. As the Predictor-Based Subspace Identification (PBSID_{opt}) algorithm [84] was used to develop the wave FF controllers, which were synthesised for the same two control objectives discussed in this study: power regulation and platform pitch motion reduction. Those controllers were then tested in the aero-servo-hydro-elastic simulation suite, Qblade [85]. It was shown in [95] that FF control for power regulation helps reduce the rotor speed fluctuations and thus leads to higher power quality output. Meanwhile, the FF control for platform pitch mitigation requires a large control effort.

A step forward towards pushing the technology readiness level of such control strategy would be conducting physical experiments. Such experiments can be performed in the field using a full-scale prototype, or a scaled-model of the system can be tested either in a wind tunnel or a wave tank. Scaled-model testing helps to better understand the system dynamics at a lower cost than full-scale prototypes. The domain where higher accuracy is required plays an important role in choosing the scaled-model testing environment, whether in a wind tunnel to focus on the aerodynamic aspect of the system or a wave basin to focus on the hydrodynamic aspect. If the tests are performed in a wind tunnel, the part of the FOWT with the uncertain theoretical model is reproduced with a physical scale model, while a numerical model is used to emulate the rest of the FOWT. Both the physical and the numerical models are then coupled via continuous measurement of some quantities of the physical model and actuation of other quantities computed in the numerical model [96]. Meanwhile, for wave tank testing, a numerical model is used to define the turbine aerodynamics and control actions, while the hydrodynamic and structural response of the platform is reproduced with a physical scale model [97].

Within the context of FF control of wind turbines, field tests of full-scale prototypes were conducted to investigate the effectiveness of LiDAR FF wind turbine control, which confirmed the positive impact LiDAR FF control has with regard to power regulation and structural loading, as was reported in [47, 52]. Unfortunately, the experiments were not successful due to unknown reasons that have nothing to do with the FF controller itself [81]. So, to the best of the authors' knowledge, no successful experiments have been conducted for the purpose of investigating wave FF control potential so far. This takes us to the main contributions of this article:

- Explore the potential of wave FF control strategy by conducting scaled-model testing in a wave basin.
- Investigate the effect of different environmental conditions on the performance of the different wave FF controllers.

The remainder of this article is structured as follows: Section 3.2 presents the experimental setup of the model-scale test. Afterwards, the control design procedure is discussed in Section 3.3. Results from the conducted wave tank scale-model tests are then discussed in Section 3.4. Finally, Section 3.5 will draw the conclusion.

3.2 Experimental Setup

The experimental campaign was performed in the Hydrodynamic and Ocean Engineering Wave Tank of École Centrale de Nantes (ECN) in France. It is 50 m long, 30 m wide and 5 m deep, equipped with a segmented wave maker composed of 48 independent flaps distributed over the width of the basin, which enables generating high-quality waves. It can produce both regular and irregular waves, taking into account wave direction. Both uni- and multi-directional waves can be generated. The generated wave periods can vary from 0.5 to 5 s, while the significant wave height at model scale can go up to 1 m for regular waves and 0.6 m for irregular ones.

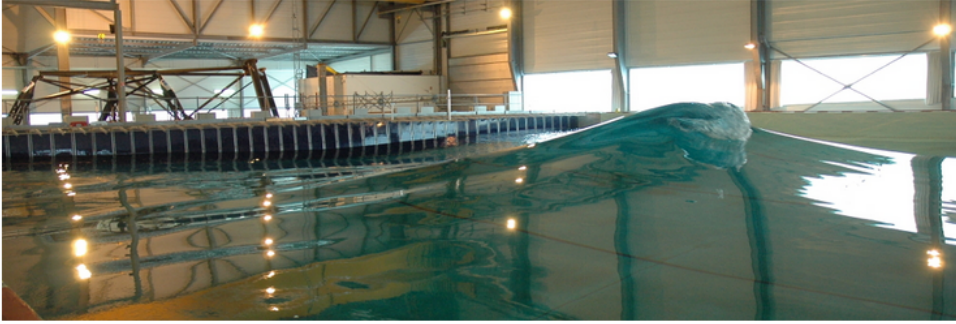


Figure 3.2: Hydrodynamics and Ocean Engineering Tank at École Centrale de Nantes.

3.2.1 Floating wind turbine model

For this study, the DTU 10 MW Reference Wind Turbine (RWT) [86] is mounted on top of a spar-type floater, at scale 1:40, as shown in Fig. 3.3. The floating platform was designed at ECN within the context of the SOFTWIND project [87]. The Softwind floating platform is a spar-type floater. It is 90 m in draft and 18 m in diameter, tapered to 11.2 m in diameter at the water level. The mooring system considered is composed of three catenary lines contained within a 16 m radius with a 120° spacing. Each line is fixed on two fairlead points by means of delta connection lines to ensure high yaw stiffness. The parameters of both the DTU 10 MW RWT and the Softwind floating platform are shown in Table 3.1 and Table 3.2, respectively.

The floating wind turbine is regulated with an industry-standard generator speed controller, as at below-rated wind speeds, the controller is seeking to maximize the extracted power by keeping the collective blade pitch angle, θ_c , constant while varying the generator torque, τ_g , as a function of the square of the generator speed, ω_g , as follows:

$$\tau_g = k_g \omega_g^2, \quad (3.1)$$

with $k_g = 0.5\rho\pi r^2(C_{p,max}/\eta_g^3\lambda_{opt}^3)$, being the generator-torque constant, ρ is the air density, r is the rotor radius, and η_g is the gearbox ratio. $C_{p,max}$ is the maximum power coefficient, which is achieved at the optimal tip-speed ratio, λ_{opt} , and zero blade pitch angle.

At above-rated wind speeds, the controller regulates the generator speed to its rated value while keeping the generator torque constant at its rated value. As a result, generator

power fluctuations are directly proportional to the oscillations occurring in the generator speed. The collective blade pitch controller regulates the generator speed about its rated value, $\omega_{g, rat}$, according to the following feedback control law:

$$\theta_c = k_p(\omega_g - \omega_{g, rat}) + k_i \int (\omega_g - \omega_{g, rat}) dt, \quad (3.2)$$

where k_p and k_i are the proportional and integral gains respectively, which were properly tuned using loop-shaping technique. It is important to mention that the gain crossover frequency was kept below the platform pitch eigenfrequency to avoid the negative damping instability. Moreover, a constant torque strategy was adopted, which, on one hand, limits the rotor speed variations resulting from reducing the natural frequency of the blade pitch controller, and on the other hand, reduces the drive-train loads and the pitch activity [39]. The feedback controller is considered the baseline against which the wave FF controller is evaluated.

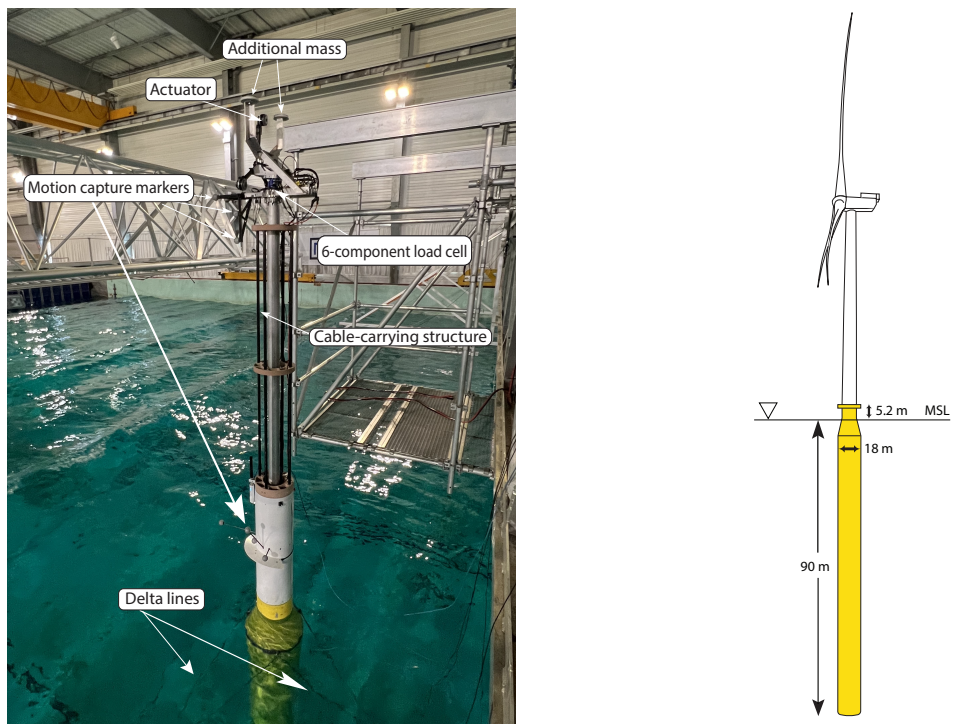


Figure 3.3: A snapshot of the floating wind turbine 1:40 scaled model of the DTU 10 MW RWT on top of the SoftWind Spar in (left), together with a schematic of the full-scale model in (right).

Table 3.1: Key parameters of the SOFTWIND spar platform [87].

Parameter	Value	Unit
Mass	1.94×10^7	kg
Roll inertia about CoG FOWT	10^{10}	kg.m ²
Pitch inertia about CoG FOWT	10^{10}	kg.m ²
Yaw inertia about CoG FOWT	6×10^8	kg.m ²
Draft	90	m
Spar diameter	18	m

Table 3.2: Key parameters of the DTU 10 MW RWT [86].

Parameter	Value	Unit
Cut-in wind speed	4	m/s
Cut-out wind speed	25	m/s
Rated wind speed	11.4	m/s
Rated power	10	MW
Peak power coefficient	0.48	-
Optimal tip speed ratio	7.55	-
Rotor diameter	178.3	m
Hub Height	119	m
Minimum rotor speed	6	rpm
Maximum rotor speed	9.6	rpm
Rotor mass	227,962	kg
Nacelle mass	446,036	kg
Tower mass	628,442	kg

3.2.2 Measurements

The measurement system consists of several sensors. As for the forces and moments, two six-component load cells (model HBM-MCS10) are placed along the tower. The first is installed between the tower-top and the nacelle to measure the rotor's integral forces and torques, while the second is installed at the transition piece to measure the tower-base loads, including the bending moments. The axial load in each mooring line is measured through an in-line submersible one-component load cell located at the connection between the main line and the delta line where the tension is supposed to be maximum. Four strain gauges are installed at the tower base to measure the tower bending strain.

An accelerometer of model ASC 5525MF-002 is installed on the nacelle, above the load cell at the tower-top. This accelerometer is used to compute the inertial force and the weight terms to obtain the actual thrust forces.

Regarding motions, an optical Qualisys motion capture system is used to measure the 3D position of 8 spherical reflective markers (see Fig. 3.3). Four markers are fixed to the

nacelle to measure the tower-top motion, while another four markers are fixed to the platform top to measure the platform motion. The platform and nacelle velocities can then be derived from the positions measured by the motion capture system via an implicit super-twisting differentiator [98].

Moreover, seven wave gauges, required for the wave reconstruction and prediction algorithm, are installed at different locations in the wave basin. The waves were calibrated with one wave probe exactly at the model's equilibrium position.

All the onboard sensors' signals are acquired via CompactRio data acquisition system, which is installed inside the spar platform to record all the measurements of the sensors fixed on the FOWT model. An HBM Quantum signal-conditioning unit records the data from the mooring load cells, the wave gauges and the water temperature sensor through the Catman software. The Qualisys software records the FOWT motions on a PC. An Ethernet cable connects the PC with the CompactRio in order to ensure the fastest possible data exchange. These three systems are then synchronized via a trigger signal generated at the start of the wave maker.

3.2.3 Software-In-the-Loop system

The main purpose of the Software-In-the-Loop (SIL) system is to take care of reproducing the aerodynamic loads on the FOWT model. It is composed of a real-time loop including acquisition, Blade Element Momentum simulation and force reproduction by means of thrusters to mimic the rotor loads, since the wind turbine rotor is not physically scaled. A motion tracking system measures the position of the platform (reference point: tower base) and the tower top deflection (fore-aft and side-side), whenever the model reacts physically to external loads (gravity, waves, moorings, and actuator).

A set of differentiators is then used to calculate the velocities of the platform and nacelle. Once the displacements and the velocities are measured, they are provided to the numerical simulation (OpenFAST), which runs in parallel to the experiments, to compute the relative velocities on the elements of the blades and, thus, the thrust force acting on the rotor. By applying Froude scaling on the thrust force obtained from OpenFAST, the reference force to apply with the actuator is then derived at model scale and applied by a set of thrusters.

The inner loop of the SIL system controls the actuators with implicit sliding mode control [98], which aims at reproducing as fast and accurate as possible the axial thrust force set point [99]. A feedback control loop enables the system to reach a satisfactory accuracy, particularly at low and wave frequencies, which are the main focus of the presented analysis. The delays of the system and the minimum rotor speed are limitations of the current setup. The total delay, defined as the delay between measurement of the state of the physical model and the reproduction of the aerodynamic force corresponding to this instant (sum of delays induced by the acquisition, simulation, and force reproduction) is estimated as 100 ms in the worst case. In terms of force magnitude, the error in the reproduction of the axial force is lower than 5% at low and wave frequencies [100].

3.2.4 Wave loads prediction

Regarding the preview of the wave excitation forces, a real-time phase-resolved ocean wave forecasting algorithm, developed by [92, 93], was used. It is composed of two steps: (1) reconstruction of the initial wave conditions by assimilating data from observations; (2)

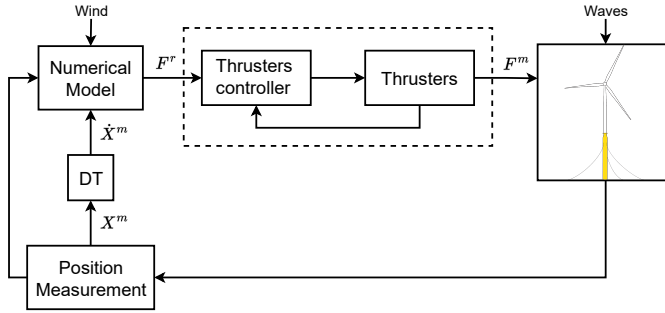


Figure 3.4: Scheme of the real-time loop for the SoftWind SIL approach, with the numerical model emulating the wind turbine controller and aerodynamic response.

wave propagation to achieve wave preview by simulating wave surfaces over a specific zone in the spatio-temporal domain. Once the wave preview is available, the wave excitation force estimation methods in [94] are applied to predict the wave excitation forces acting on the FOWT.

Figure 3.5 illustrates the comparison between the real surface wave elevation and wave excitation pitch moment at the FOWT and the predicted wave elevation and moment expected at the FOWT. We can already see that the prediction algorithm can provide a fairly accurate wave preview.

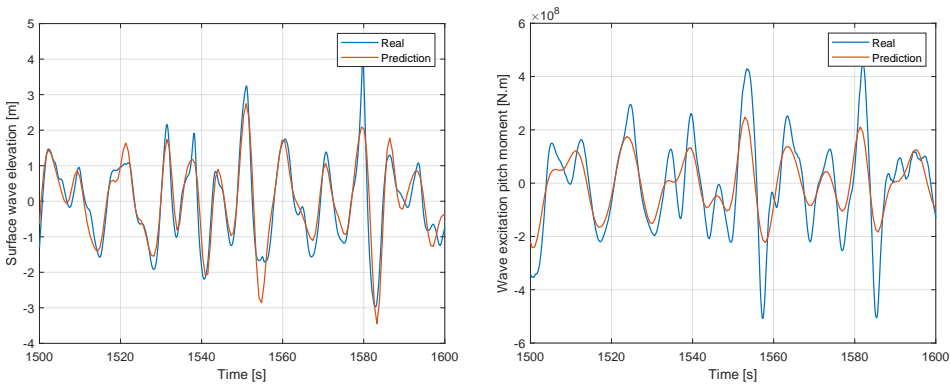


Figure 3.5: Comparison between the wave preview of the surface wave elevation (left) and the wave excitation pitch moment (right), obtained via the prediction algorithm [92], and the real wave height and moment measured at the FOWT location.

3.3 Synthesis of the wave feedforward controller

In this section, the controller design is presented. First, the control model is explained before moving to the control synthesis of the FF controller.

3.3.1 Data-driven approach

Figure 5.4 shows a block diagram of the FOWT model and control signals. Each block represents a linear Transfer Function (TF). G_{θ_p, M_w} represents the mapping from the wave-induced pitch moments, M_w , to the platform pitch motion, θ_p , while G_{ω_g, M_w} maps the wave-induced pitch moments to the generator speed, ω_g . Similar to the wave moment, the effect of blade pitch, β , on the generator speed and the platform pitch motion is described by the TFs $G_{\omega_g, \beta}$ and $G_{\theta_p, \beta}$, respectively.

To obtain these TFs, which are required for the control design, identification is conducted on the results obtained from QBlade [85], where the FOWT is modelled at full scale and was able to reproduce the experimental results [101]. QBlade is a fully coupled, non-linear, aero-hydro-servo-elastic wind turbine simulation suite that is capable of simulating wind turbines. System identification is also required when using QBlade for control design purposes, as it is not equipped with a linearisation functionality, thus making it complicated to do model-based control.

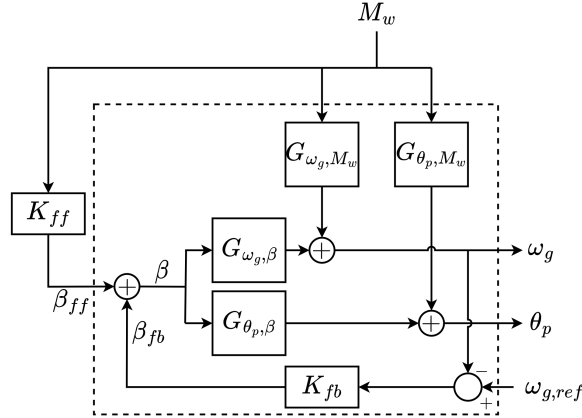


Figure 3.6: Block diagram of the FOWT model

The TFs were identified at an average wind speed of 16 [m/s] as an operating point. A similar procedure was used for both the spectral estimation and the system identification, where an experiment of a duration of 25000 [s] was performed in QBlade.

In order to obtain the TFs; $G_{\omega_g, \beta}(s)$ and $G_{\theta_p, \beta}(s)$, a chirp signal, logarithmically distributed over the experiment's duration, was used to excite β within a frequency band (0.02 to 0.3 Hz). As for $G_{\omega_g, M_w}(s)$ and $G_{\theta_p, M_w}(s)$, a JONSWAP spectrum was used for waves.

A non-parametric form of the above-mentioned TFs is obtained from the input-output data by spectral estimation. A frequency response function (FRF), assuming no correlation between the input and noise signals, is achieved according to:

$$G_{y,u}(j\omega) = \frac{S_{yu}(j\omega)}{S_{uu}(j\omega)}, \quad (3.3)$$

where ω in Eq. (3.3) denotes the frequency, $j = \sqrt{-1}$, while $S_{yu}(j\omega)$ is the cross-power spectral density of the output and input, $S_{uu}(j\omega)$ is the auto-power spectral density, and

$G_{y,u}(j\omega)$ represents the estimated FRF. Based on the estimated frequency response functions and the FF structure given in Fig. 5.4, the optimal non-parametric FF controller, for both the generator speed control and the platform pitch motion control, can be estimated and are respectively given by:

$$\begin{aligned} K_{ff,\omega}(j\omega) &= -\frac{G_{\omega_g,M_w}(j\omega)}{G_{\omega_g,\beta}(j\omega)}, \\ K_{ff,\theta_p}(j\omega) &= -\frac{G_{\theta_p,M_w}(j\omega)}{G_{\theta_p,\beta}(j\omega)}. \end{aligned} \quad (3.4)$$

The optimal non-parametric controllers are given by the blue lines in Fig. 3.7a and Fig. 3.7b, respectively.

So far, the controllers given in Eq. (3.4) are non-parametric since FRFs were used. However, they cannot be directly employed for control implementation.

The parametric controllers are obtained by fitting stable FF parametric TFs to the spectral estimate as shown in Fig. 3.7a and Fig. 3.7b. The fitting must be ensured to be of the highest accuracy within the wave band enclosed by the dashed vertical lines in the figures, such that the performance is ensured within the wave frequency range (0.05-0.2 Hz) without the need for complex higher order control structures. Outside the wave bandwidth, the controller is not supposed to react.

The parametric wave FF targeting the power regulation, K_{ff,ω_g} , takes a structure that is a combination of a double integrator, first order zero, and a second-order system according to Eqn. (3.5):

$$K_{ff,\omega_g} = \frac{K_{\omega_g}}{s^2} \frac{\tau s + 1}{s^2 + 2\zeta\omega_c s + \omega_c^2}, \quad (3.5)$$

where K_{ω_g} is a static gain for controller tuning, τ a time constant, ζ the damping ratio, and ω_c being the corner frequency of the controller.

While for the parametric FF controller targeting the platform pitch, K_{ff,θ_p} , the controller structure is composed of a double differentiator together with a second order system, with K_{θ_p} being a static gain for controller tuning, as illustrated in Eqn. (3.6):

$$K_{ff,\theta_p} = \frac{K_{\theta_p} s^2}{s^2 + 2\zeta\omega_c s + \omega_c^2} \quad (3.6)$$

Investigating Fig. 3.7a and Fig. 3.7b, they show a good agreement between the spectral-based and the parametric FF controller within the frequency band of interest enclosed by the dashed vertical lines, which gives confidence in the fitted parametric controllers.

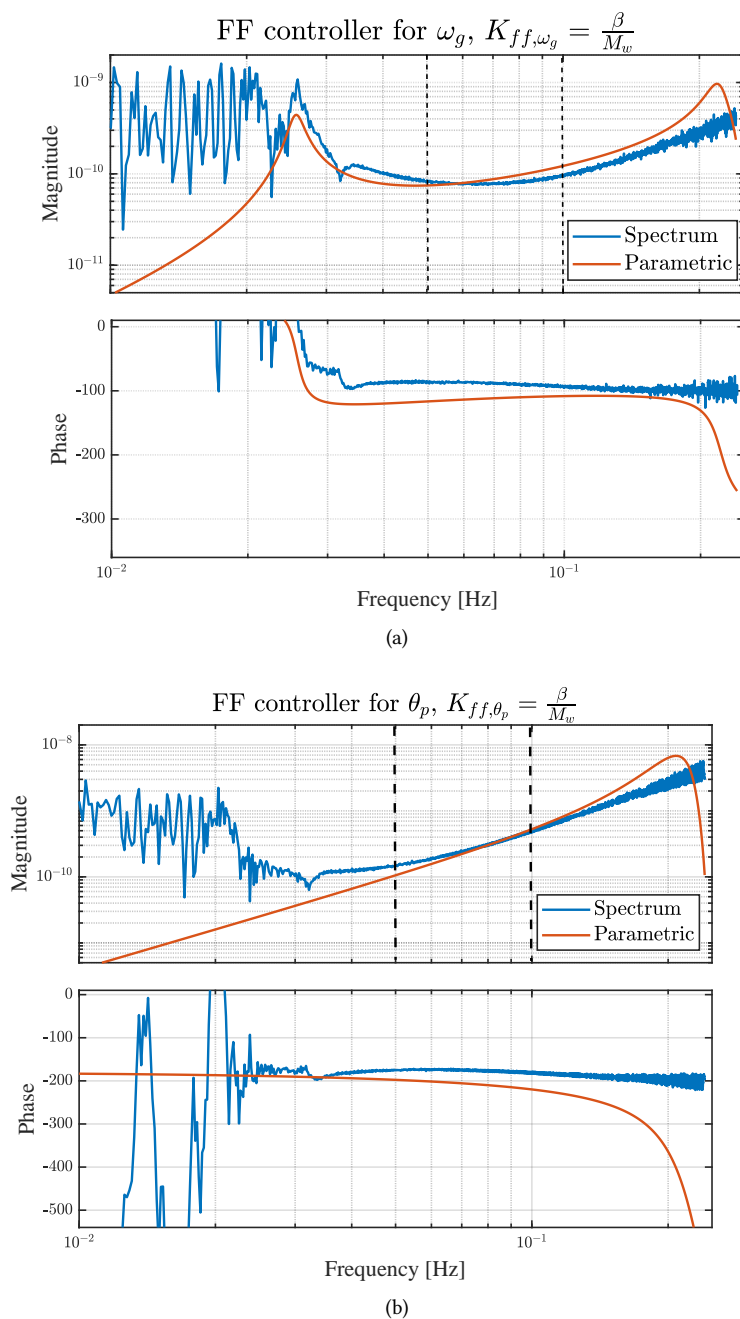


Figure 3.7: Bode plot of the optimal feedforward controller for (a) power regulation and (b) platform pitch motion reduction. Blue: spectral estimate, Red: parametric controller.

3.4 Results

In this section, the results of the experimental campaign are illustrated and discussed. The wave tank tests were performed at different conditions to properly assess the controller performance for power regulation (P_g) and platform pitch motion reduction (θ_p). First, both controllers are tested at the same condition to investigate their effectiveness. Afterwards, we carried out the rest of the experiments with the more effective one, which was then tested at different wind speeds, turbulence intensities, significant wave heights and wave directions. Accordingly, each case would be treated separately. So, we will first look at the effect of varying the turbulence intensity, TI, at a certain wind speed. This is followed by varying the significant wave height, H_s , then the wave directional spreading parameter, s , before concluding with varying the wind speed, V . In each case, one of the parameters is varied, while the rest are kept constant. The different experiments that were performed are listed in Table 3.3:

Table 3.3: Environmental conditions for the different experiments performed in the wave tank, (P_g refers to the power regulation controller, while θ_p for platform pitch motion reduction).

Case	V [m/s]	TI [%]	H_s [m]	T_p [s]	s [-]	Control objective [-]
Control objective	14	7.1	5	12	∞	$[P_g, \theta_p]$
Variable TI	14	[0, 7.1, 13.8]	7	12	∞	P_g
Variable H_s	14	7.1	[5, 7, 9]	12	∞	P_g
Variable s	14	7.1	7	12	[15, 25, 60]	P_g
Variable V	[14, 17, 20]	7.1	7	12	∞	P_g

3.4.1 Control objective

We begin by illustrating the performance of the two different FF controllers for power regulation and platform pitch motion reduction, each one at a time against the baseline FB controller. At the end, we should be able to determine the effectiveness of the wave FF control for each control objective.

The two control strategies were compared by performing the SIL experiment at fixed wind and wave conditions. Turbulent wind at $V = 14$ m/s and $TI = 7.1\%$ was considered. Waves according to a JONSWAP spectrum, with $H_s = 5$ m and $T_p = 12$ s were considered.

Figure 3.8 shows the generator power, the collective blade pitch and the platform pitch time-domain responses together with their PSDs with the different controllers. At first, the experiment was performed only with the FB controller as a baseline case. Afterwards, the FF controllers for both power regulation and platform motion reduction were added to the FB controller. We can see in the time response of the blade pitch signal the higher frequency ripples, corresponding to waves, oscillating about a lower frequency sinusoidal signal corresponding to the wind turbulence. This indicates that adding the FF controller to the control loop on top of the FB controller does not have any effect on the low-frequency content that corresponds to the wind turbulence, as it remains unchanged, but only reacts to the higher frequency wave signals, which results in additional blade pitching. This is also evident in the PSDs, where we see that in the wave frequency range (0.05-0.2 Hz), the generator power signal has less spectral content than the baseline case for the power regulation control objective, while there is no change at lower frequencies for both objectives. On the contrary, when the FF controller for the platform motion reduction

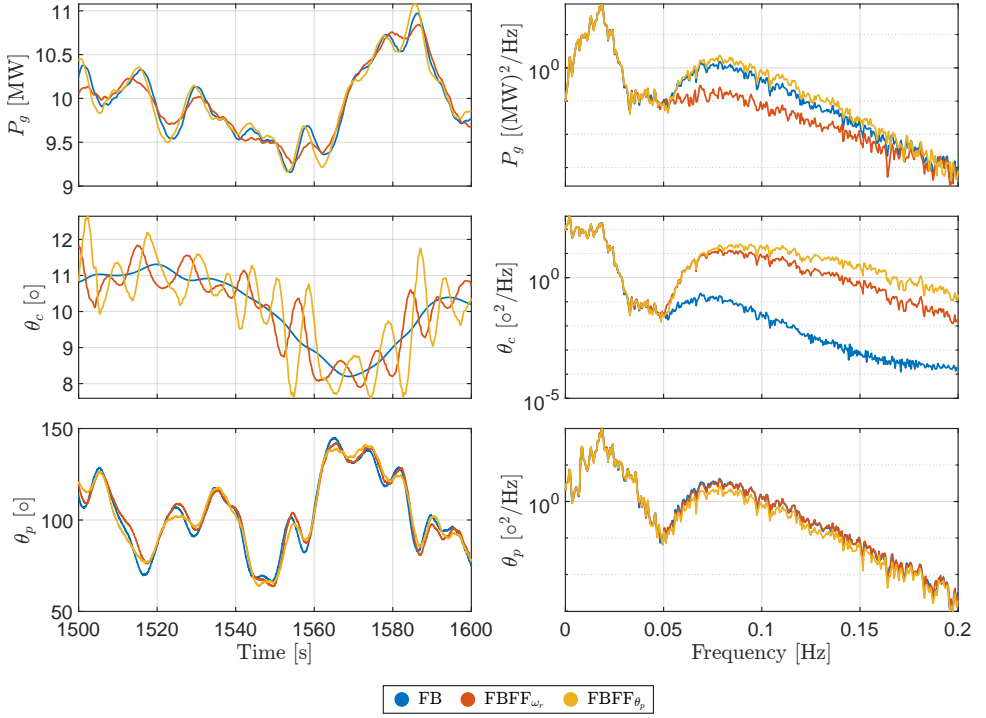


Figure 3.8: Generator power (P_g), blade pitch (θ_c) and platform pitch (θ_p) responses with and without wave feedforward control, at wind $V = 14$ m/s, $TI = 7.1\%$, and wave conditions of $H_s = 5$ m and $T_p = 12$ s. The two feedforward controllers, for the objectives of power regulation and platform pitch motion reduction, are compared to the baseline feedback controller.

objective is operational, the spectral content in the generator power signal slightly increases above the baseline.

The PSDs in Fig. 3.8 also show that the reduction in the generator power fluctuations with the FF controller for power regulation is achieved with less blade pitch actuation than the reduction resulting from the FF controller for the platform pitch motion. So, we conclude that the reduction of the platform pitch motion requires a significantly large actuation for a smaller gain relative to the one for power regulation, which is evident in Fig. 3.8, where the effect of the feedforward controller, FBFF $_{\theta_p}$, on the platform motion is minor, unlike the effect of FBFF $_{\omega_r}$ on the generator power.

In Fig. 3.9, the standard deviation, as a statistical metric illustrating the variation of a signal about its mean, is used to demonstrate the effect of the FF controllers, since they are expected to counteract the effect of the wave disturbance, and thus, reduce the variance of the generator power and the platform pitch. In fact, Fig. 3.9 shows the percentage difference between the standard deviation of the signals with and without the FF control, which is normalised with respect to the standard deviation of the baseline feedback controller. As mentioned earlier in Fig. 3.8, FBFF $_{\omega_r}$ is mitigating the wave effects on the quality of P_g by reducing the variations in ω_r as illustrated in Fig. 3.9. The variation in θ_c increases

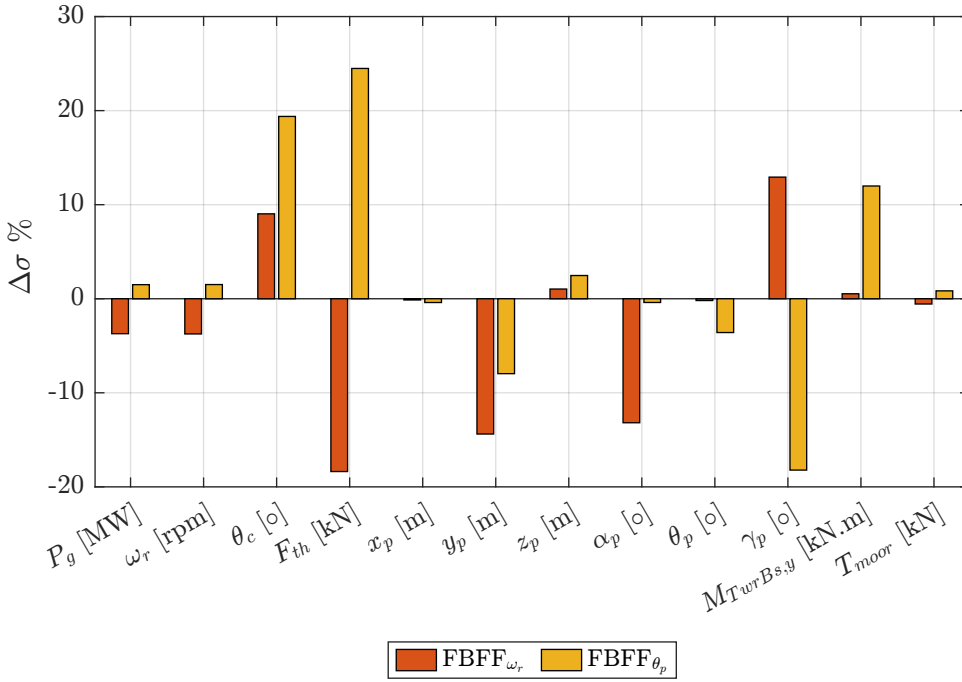


Figure 3.9: Normalised standard deviation percentage change of the two different control modes for different variables with respect to the baseline FB case. All cases were held at wind speed of $V = 14$ m/s, with $TI = 7.1\%$, and wave conditions of $H_s = 5$ m, and $T_p = 12$ s.

for both FF controllers relative to the baseline case. This indicates that, indeed, the FF controller is active for both objectives. However, in order for $FBFF_{\omega_r}$ to achieve its control objective, it requires almost half the blade pitch actuation needed by $FBFF_{\theta_p}$ to achieve its control objective. As for $FBFF_{\theta_p}$, the blade pitch variation about the mean value increases by almost 20% above the baseline case to achieve its control objective.

Even though the blade pitch action is higher with the FF controller than in the FB baseline case, the FF control contribution reduces that of the FB controller, as it does not need to react to the wave disturbance anymore since the FF is taking care of that. The variation of the total thrust force varies for both objectives, as for the $FBFF_{\omega_r}$, the thrust variance decreases below the baseline, which is not the case for $FBFF_{\theta_p}$. The thrust variation is reduced as a result of more blade pitching by $FBFF_{\omega_r}$ in order to regulate the rotor speed, while for $FBFF_{\theta_p}$, thrust is varied continuously to keep the platform pitch motion as minimal as possible.

Regarding the platform motion, we can say that the FF control, in general, has a positive effect on the platform motions as we see a reduction for both control objectives in most of the degrees of freedom (DOFs). Now, that might vary from one DOF to another as we can see, for instance, there is a minor reduction in the surge, x_p , and pitch, θ_p , DOFs, while a significant reduction in sway, y_p , and roll, α_p , DOFs. For heave, z_p , and yaw, γ_p , DOFs, $FBFF_{\omega_r}$ and $FBFF_{\theta_p}$ lead to more oscillations, while their effect differs when it comes to

yaw DOF. As FBFF_{ω_r} increases oscillations in platform yaw, while FBFF_{θ_p} reduces those fluctuations significantly. This is an extra effect from FBFF_{θ_p} since it was designed to mitigate the platform pitch, θ_p , oscillations only. FBFF_{ω_r} hardly affects the tower-base bending moment, $M_{TwrBs,y}$, as an insignificant increase is observed, which is not the case for FBFF_{θ_p} that leads to more tower-base loading. Regarding the mooring tension, T_{moor} , both FBFF_{ω_r} and FBFF_{θ_p} affect the mooring tension slightly, as FBFF_{ω_r} leads to a small reduction in the tension oscillation, while FBFF_{θ_p} causes a slight increase in the mooring tension.

According to Fig. 3.9, not only does the platform motion alleviation objective require large actuation effort, but it also increases the tower-base bending moment, unlike the power regulation objective. As a result, we proceeded with the FF control for power regulation, FBFF_{ω_r} , for the rest of the study.

3.4.2 Effect of turbulence intensity variation

After showing the potential of FF control for both objectives and observing that the platform pitch motion reduction FF control requires large actuation, the remaining experimental results are based on the power regulator FF. We start with investigating the effectiveness of the FF controller while varying the turbulent intensity. The experimental results at wind speed of 14 m/s were chosen for this discussion. Fig. 3.10, Fig. 3.11, and Fig. 3.12 clearly illustrate the performance of the FF control. In Fig. 3.10, the effect of waves on the generator power is reduced compared to the FB only cases, as there is a reduction at all the turbulent intensities within the wave frequency range (0.05–0.2 Hz). This is depicted in the Power Spectral Density (PSD) of Fig. 3.10, where the addition of FF control reduces the energy within the wave energy band. However, it has no effect within the low-frequency band corresponding to wind turbulence, which is to be expected since the controller's bandwidth is targeting the wave frequency range only.

Increasing the turbulence intensity has a direct effect on increasing the variance of the depicted signals. In steady wind, we can clearly observe how the time traces are dominated by the high-frequency sinusoids relevant to wave frequency band, while the low-frequency sinusoids, relevant to wind turbulence, dominate as the TI increases. This leads to increasing the peak-to-peak value about the mean of the signal, indicating an increase in the variance of the signal. This can also be confirmed by the PSD, where there is more spectral content in the low-frequency bandwidth than the bandwidth related to the waves. In steady wind, we can observe a reduction in the generator power variation as a result of using wave FF control. However, once the wind inflow becomes more realistic and wind turbulence increases, the reduction in the generator power oscillations is not as significant. This indicates that the wind turbulence, lying in the low-frequency band, dominates the global dynamic response even though the wave FF controller is taking care of oscillations caused by the waves in the high-frequency band.

Figure 3.11 illustrates the platform pitch response at different turbulence intensities. In Fig. 3.11, we see that the FF controller has no authority on the platform motions in the wave band, which is reasonable since this controller is mainly aimed at reducing power fluctuations. Also, for the TI effect, we see a clear domination of the wind turbulence.

As for the collective blade pitch angle in Fig. 3.12, the pitch actuator is clearly active in the wave frequency range with the FF control compared to the FB controller. We see

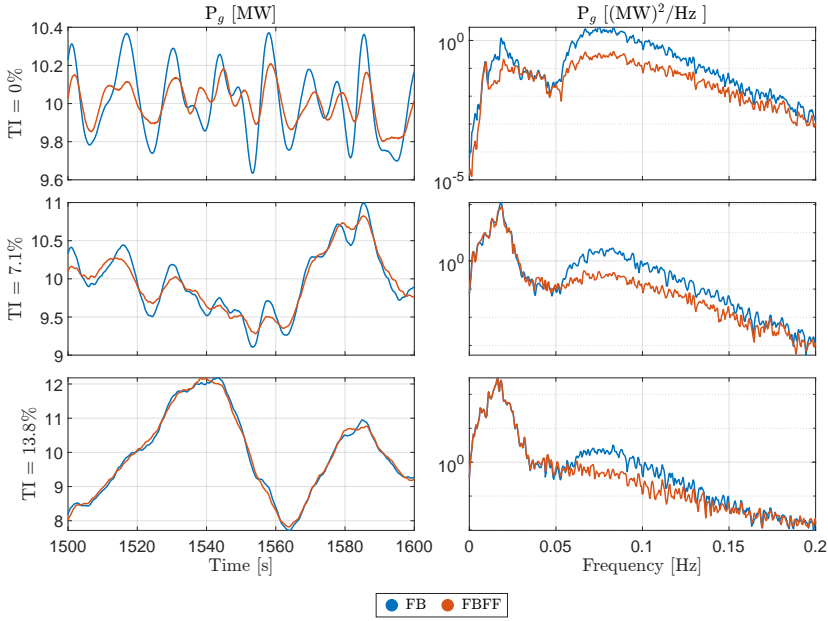


Figure 3.10: Generator power response with and without wave feedforward control, at $V = 14$ m/s, varying from steady wind at 0% TI to turbulent wind at TI = 7.1% and 13.8%.

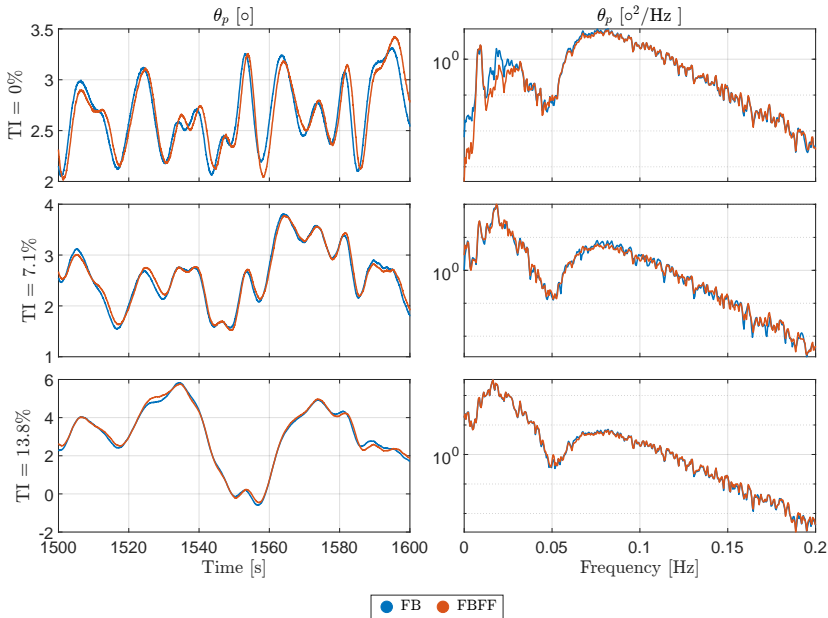


Figure 3.11: Platform pitch response with and without wave FF control, at wind speed of $V = 14$ m/s, varying from steady wind at 0% TI to turbulent wind at a TI of 7.1% and 13.8%.

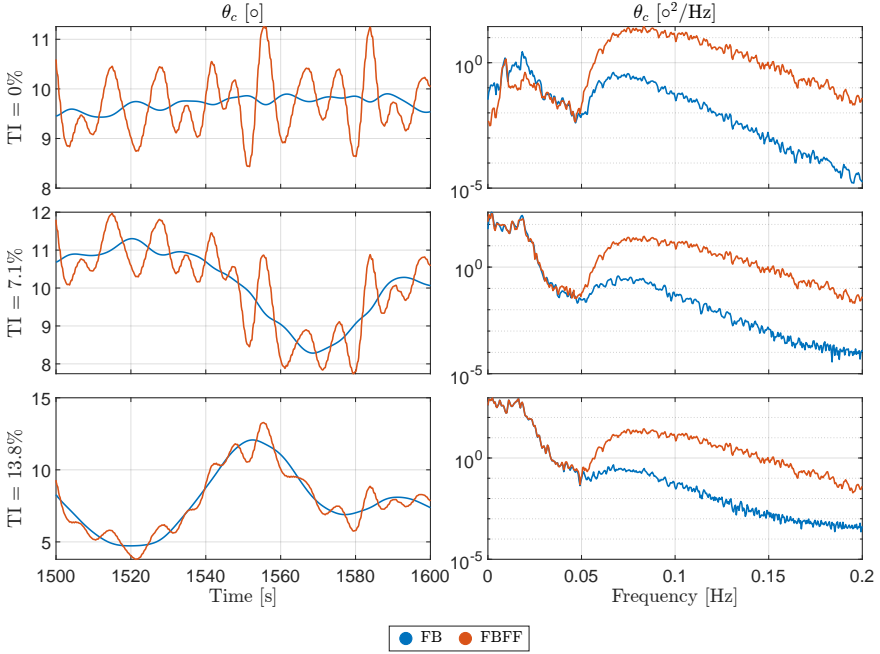


Figure 3.12: Collective blade pitch angle with and without wave FF control, at wind speed of $V = 14$ m/s, varying from steady wind at 0% TI to turbulent wind at a TI of 7.1% and 13.8%.

that the FB controller is only reacting to the low-frequency wind turbulence, while not considering the wave disturbance because of the negative damping implications that would happen if the bandwidth of the FB controller is increased [39, 40, 63, 65, 83, 102, 103]. Moreover, it is observed that the peak-to-peak value of the FBFF control signal decreases as the turbulence intensity increases. This indicates that in steady wind, the blade pitch actuator is varying at a higher rate than in turbulent wind, and the higher the turbulence, the lesser the blade pitch variation. This is depicted and discussed in Fig. 3.13.

The Standard Deviation (SD) of the signals is used to quantify the effect of the FF control on the different variables of interest, as shown in Fig. 3.13. It is fair to mention that the figure illustrates the difference between the FF control with respect to the baseline FB controller in steady wind case. The effect of including FF control can already be seen as the main objective of the FF controller is to regulate the generator power, P_g . However, the focus in this subsection is on the effectiveness of the FF strategy at different wind inflow turbulent intensity conditions. It is striking to see how the wind dominates the waves as the turbulence intensity increases, as the reduction in the generator power fluctuations decreases with the increase in the turbulence intensity. Thus, we can conclude that the FF strategy is indeed effective for improving the power quality, but as the turbulence intensity increases, the effectiveness of the FF diminishes. Furthermore, the effect of the turbulence intensity on the platform motion varies from one DOF to another, and there is no clear trend for the different DOFs.

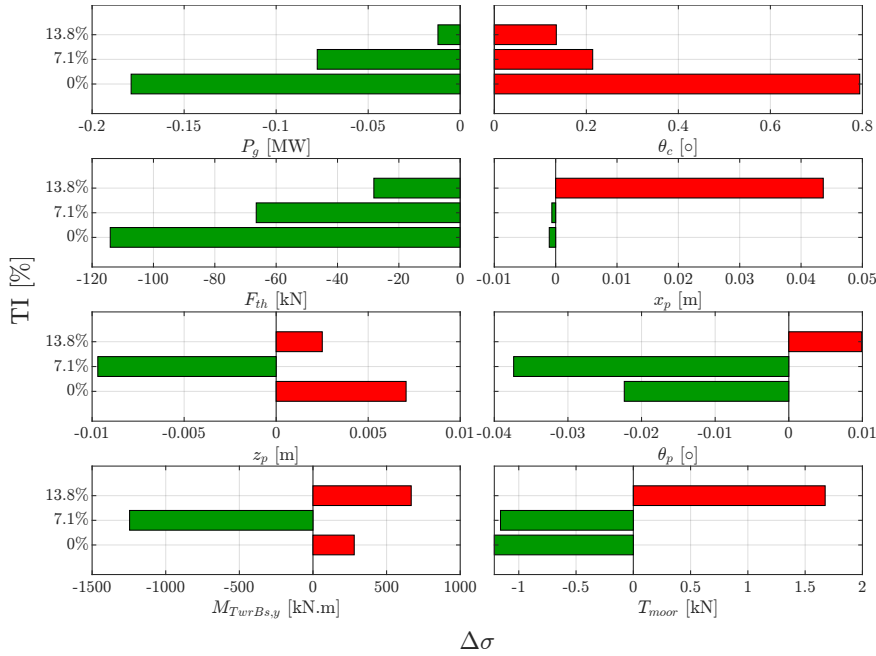


Figure 3.13: Standard deviation change with wave FF control relative to the baseline feedback control, at wind speed of $V = 14$ m/s, varying from steady wind at 0% TI to turbulent wind at a TI of 7.9% and 13%.

3.4.3 Effect of significant wave height variation

Varying the significant wave height has, without a doubt, effects on the FF control performance. As the disturbance TF accounts for the mapping from the wave excitation forces, as a disturbance input, to the rotor speed. By wave excitation forces, we are referring to the first-order wave forces based on linear wave theory [104], where there is a direct transfer from the wave height to the first-order wave excitation forces through the transfer functions known as the Response Amplitude Operators (RAOs). To have a deeper look at this subject, different wave conditions were applied, where different significant wave heights were considered while keeping both the peak period and the wind speed constant. This is in addition to having long-crested unidirectional waves (i.e., $s = \infty$). The peak period was kept constant because the natural periods are very large compared to the waves (>30 s). The motions RAOs are hence quite low, in particular on a spar, which is known to have small wave-induced motions. Therefore, there would be only a very limited effect of varying the peak period across the typical peak periods of ocean waves.

Looking at Fig. 3.15, apart from the FF control operating as expected, we can see how the amplitude of the generator power oscillations at the wave frequencies increases as waves get bigger, which corresponds to an increase in energy in the PSDs for the corresponding signals. This rise in amplitude can also be observed in the blade pitch signal to maintain the rotor speed as close to its rated value as possible.

Figure 3.16 summarises the effect of varying the significant wave height on the different variables of interest. It is pretty clear how the FF controller reacts to waves; the bigger they

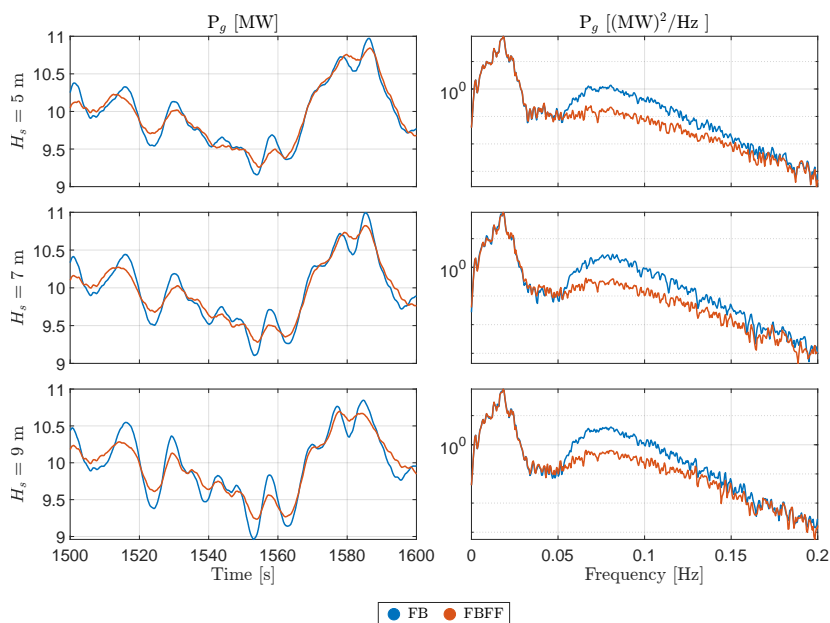


Figure 3.14: Generator power responses with and without wave FF control, at a turbulent wind speed of $V = 14$ m/s with $TI = 7.1\%$, and unidirectional waves at $s = \infty$, and $T_p = 12$ s, but at different significant wave heights, H_s .

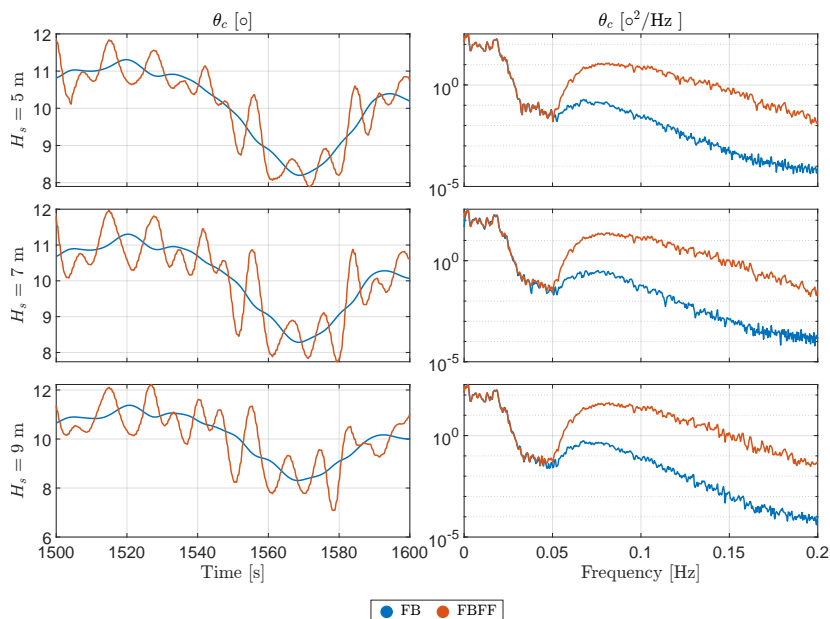


Figure 3.15: Collective blade pitch responses with and without wave FF control, at a turbulent wind speed of $V = 14$ m/s with $TI = 7.1\%$, and unidirectional waves at $s = \infty$, and $T_p = 12$ s, but at different significant wave heights.

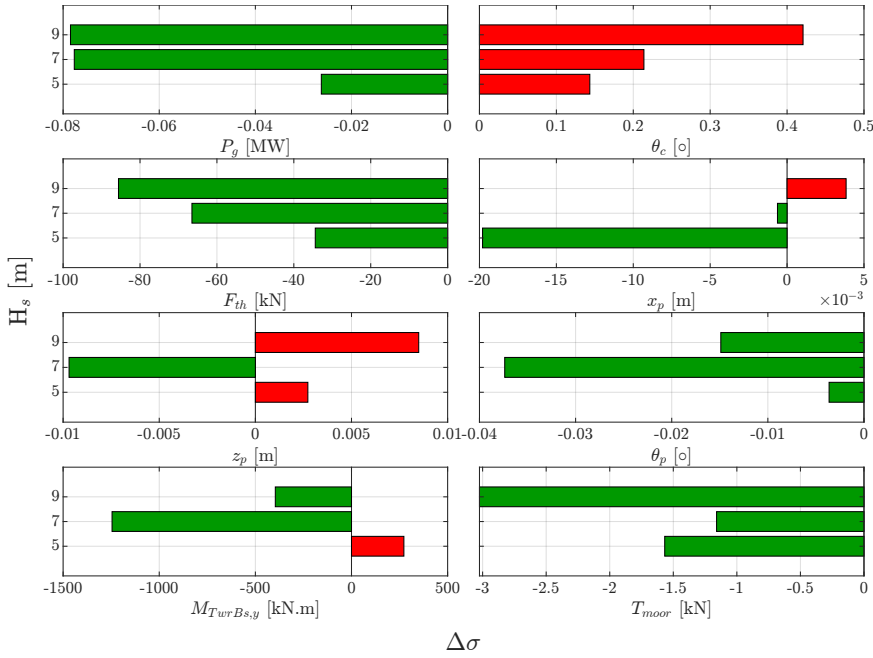


Figure 3.16: Standard deviation change of different variables of interest with wave FF control, at a turbulent wind speed of $V = 14$ m/s with $TI = 7.1\%$, and waves of $T_p = 12$ s, but at different significant wave heights, H_s . The bars illustrate the difference in standard deviation with the FF control compared to the baseline case at each significant wave height.

get, the stronger the FF control action is. This is illustrated in the generator power and the blade pitch signals. On the contrary, we see a rise in the fluctuations in the thrust force as the significant wave height becomes higher.

Regarding the platform motion, each DOF has a different sensitivity to the wave height variation. We see, for instance, that the fluctuations in the surge DOF significantly decreases with the FF control compared to the baseline FB controller at $H_s = 5$ m, while as H_s increases, the percentage difference in the standard deviation goes from negative to positive at $H_s = 9$ m indicating that the power regulation FF control leads to higher surge displacements at bigger waves. Concerning heave and pitch DOFs, we observe that at $H_s = 7$ m in particular, there is a considerable alleviation in the oscillations of both signals with respect to the baseline FB control. However, an increase in the platform heave oscillations can be seen for the other two wave heights, while a mitigation in the platform pitch fluctuations is observed at all the wave heights.

3.4.4 Effect of wave directional spreading

After investigating the effect of varying the turbulence intensity and the significant wave height, we move on to the effect of the wave directional spreading on the different variables of interest with the FF control present. For this part of the experimental campaign, waves were generated at $H_s = 7$ m, and $T_p = 12$ s, but at a different directional spreading parameter,

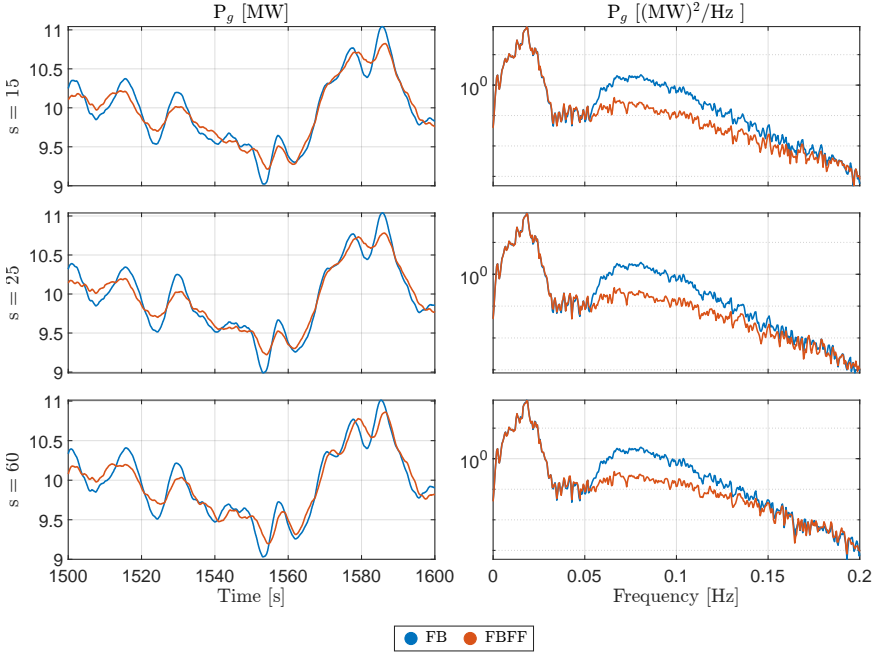


Figure 3.17: Generator power response with and without wave FF control, at a turbulent wind speed of $V = 14$ m/s with $TI = 7.1\%$, and waves with $H_s = 7$ m, and $T_p = 12$ s, but with different directional spreading parameter, varying from short to long crested waves.

where it was varied from a low value corresponding to short-crested waves of a multi-directional nature, to higher values that correspond to long-crested waves that act in a more unidirectional manner.

Starting with Fig. 3.17, where the generator power is depicted, it can be observed that even though the disturbance TF, used in the FF control synthesis, was identified based on unidirectional waves, yet the FF controller is working well also in multidirectional waves, which is evident in the time history and the PSD. As for the different directional spreading parameter cases, whether with FB only or FBFF, we can not really detect a big influence of the wave directional spreading on the generator power signal, as the amplitudes at each time instant, or frequency, almost do not change. This is an expected result, which is attributed to the fact that the system identification was performed with the wave excitation moment as a disturbance input instead of the surface wave elevation. This was done for the purpose of eliminating the effect of wave directionality from the control problem. Therefore, there is no reason to expect the FF controller to be less effective in wave conditions with different directional spreading since the directional spreading does not have a very significant effect on the distribution of the wave excitation forces over the frequencies.

Moving to Fig. 3.18, again, the activity of the FF controller within different wave directional conditions is clear, and again, the amplitudes of the blade pitch signal do not differ too much from each other.

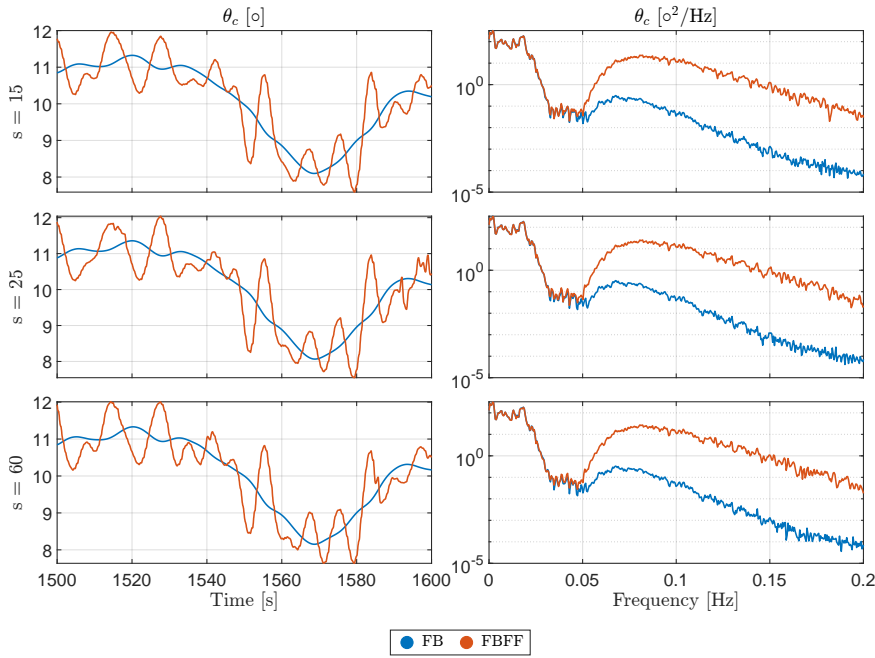


Figure 3.18: Collective blade pitch response with and without wave FF control, at a turbulent wind speed of $V = 14$ m/s with $TI = 7.1\%$, and waves with $H_s = 7$ m, and $T_p = 12$ s, but with different directional spreading parameter, varying from short to long crested waves.

The wave directionality results are summarised in Fig. 3.19. We see that in short-crested waves, which are the ones with low spreading parameter, the effectiveness of the FF control is slightly reduced compared to the long-crested waves case. Directional spreading results in a reduction of the pitch and surge excitation forces. So, in terms of the wave excitation force, an increased directional spreading has an effect similar to a decreased wave height. In that sense, the results in Fig. 3.19 are consistent with those in Fig. 3.9.

Again, there is no specific trend for the platform motions, as we see a different effect at each spreading parameter for every DOF. Also, the different DOFs do not agree on a certain behaviour at every spreading parameter. We see the surge decreasing at short-crested, then increasing, before decreasing again. The heave decreases slightly before increasing all the way. The platform pitch is always less oscillatory than the baseline FB case, but this reduction in oscillations seems to vary in a random manner, as the reduction is maximum at short-crested waves, then decreases as the wave spreading decreases (s increases), before increasing again slightly as the waves become more long-crested.

3.4.5 Controller performance at different wind speeds

In this subsection, we show the control performance when the wind speed varies. Initially, the controller was synthesised at a single operating point at wind speed of 16 m/s. Consequently, the controller might be expected not to perform optimally at other wind speeds.

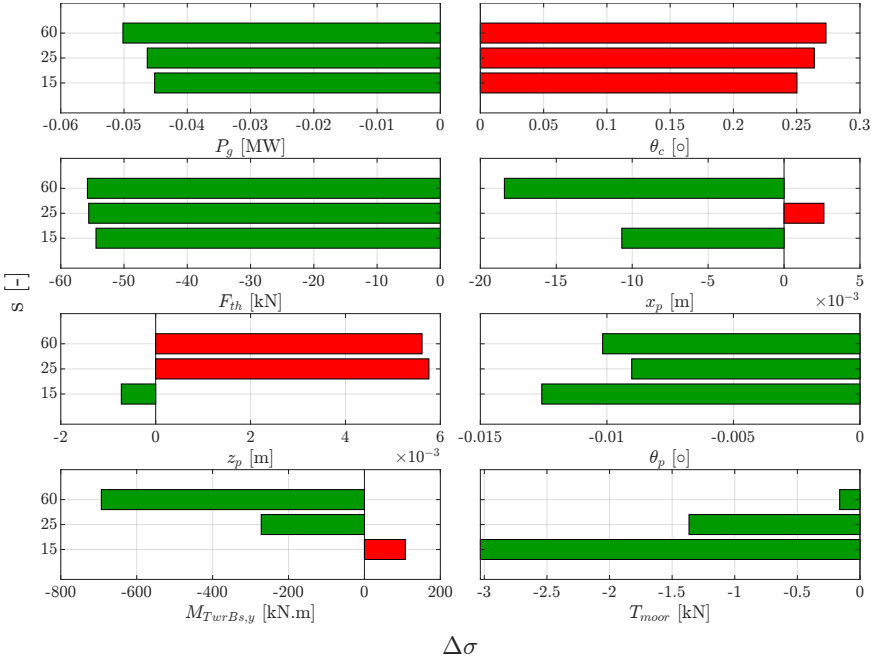


Figure 3.19: Normalised standard deviation percentage change of different variables of interest with wave FF control, at a turbulent wind speed of $V = 14$ m/s with $TI = 7.1\%$, and waves with $H_s = 7$ m, and $T_p = 12$ s, but with different directional spreading parameter, S , varying from short-crested, at $s = 15$, to longer crested waves at $s = 60$. The bars illustrate the difference in standard deviation with the FF control compared to the baseline case at each directional spreading parameter.

However, Fig. 3.20 suggests otherwise, as it shows the controller efficiently operating at different wind speeds. This is clear in both the time response, where we observe a decent reduction in the peak-to-peak amplitudes, as well as the spectral content in the PSDs.

This gives confidence in the controller that it is robust enough to handle the non-linear dynamics of the FOWTs without the need for gain scheduling, even though it was synthesised for a single operating point. Of course, having a gain-scheduled controller would ensure that the controller is performing optimally at each operating point across the spectrum of the operating wind speeds of the wind turbine. Yet, sometimes, having a sub-optimal controller is preferred to have a compromise between performance and control effort.

3.5 Conclusions

Successful wave tank experiments were conducted to evaluate the benefits of the wave feedforward control strategy, using a wave excitation force preview, in terms of the structural loads and the power quality of the floating wind turbine components. It was found that the effectiveness of the wave feedforward controller for reducing the power fluctuations is higher than the one for decreasing the platform pitch motion, as, the feedforward controller for generator power requires less actuation than the feedforward controller

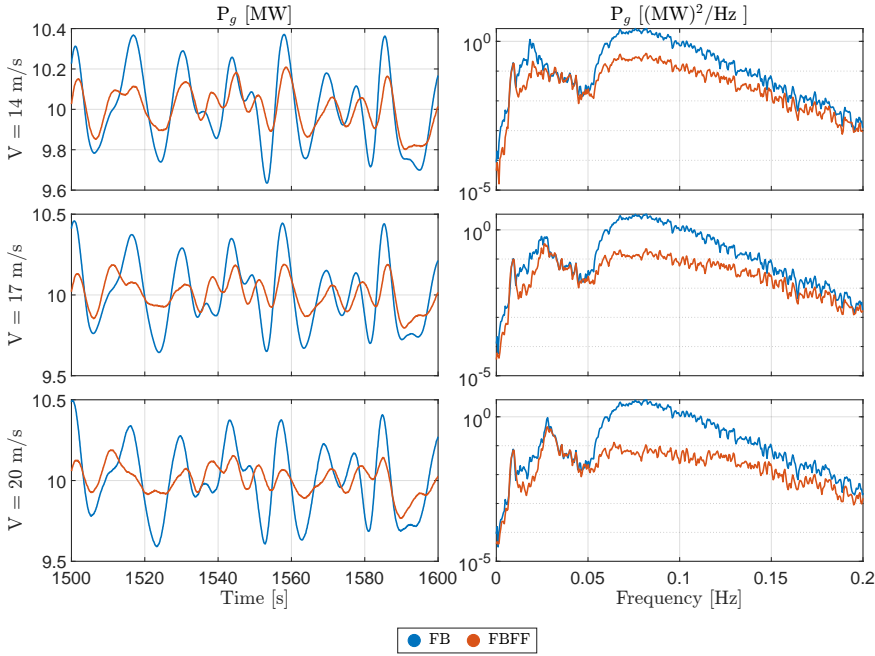


Figure 3.20: Generator power response with and without wave FF control, at different steady wind speeds at 14 m/s, 17 m/s and 20 m/s, and long-crested waves with $H_s = 7$ m, $T_p = 12$ s, and $S = \infty$.

for the platform pitch motion, and the reduction in the generator power oscillations is greater than the alleviation in the platform pitch motion. The experiments went on to investigate the performance of the feedforward control for power regulation within several environmental conditions, as well as how these conditions affect the turbine dynamics in general. Subsequently, some experiments were performed at different wind turbulence intensities, others at varying significant wave heights, and others at contrasting wave spreading conditions.

The wave feedforward strategy was indeed proven to be operational and effective at different environmental conditions. However, we concluded that as the turbulence intensity increases, the wind dominates, and the effectiveness of the feedforward control diminishes. As for varying significant wave heights, as the waves get bigger, the responses of the different DOFs of the platform motion vary randomly. While for different wave spreading parameters, it was shown that the power fluctuations are higher in the case of short-crested waves than in long-crested ones. However, the difference is rather insignificant, which indicates that the main source of fluctuations is the fore-aft direction.

In short, the wave feedforward control strategy is effective when it comes to alleviating the effects of the wave forces on the produced power of the FOWT, whereas wave feedforward control requires a significant amount of actuation to minimise the platform pitch motion, which makes such a technology unfavourable for that objective.

4

4

A Novel Control Architecture for Floating Wind Turbines

The control of Floating Wind Turbines (FWTs) is challenging, as they possess much lower natural frequencies related to the structure's rigid body motion, which creates an undesirable coupling between tower motion and the blade pitch control. As a result, the tower motion is negatively damped triggering instability. This is because of the presence of Right Half Plane Zeros (RHPZs) imposing fundamental limitation on the control bandwidth. To address this problem, different solutions were proposed with varying control structures ranging from Single-Input, Single-Output (SISO) controllers to Multiple-input, Multiple-output (MIMO) ones. In this paper, a new control structure, of Single-Input, Multiple-Output (SIMO) is proposed that is able to lift the bandwidth limitation, while using simple elements that match the industry demands.

This chapter is based on:

📄 A. Hegazy, P. Naaijen, J.W. van Wingerden, "A novel control architecture for floating wind turbines", 2023 International Federation of Automatic Control (IFAC) World Congress, Yokohama, Japan, IFAC-PapersOnLine, Volume 56, Issue 2, 2023, Pages 7644-7649, ISSN 2405-8963, doi:10.1016/j.ifacol.2023.10.1163

4.1 Introduction

During model experiments of Floating Wind Turbines (FWTs), it was observed that the conventional blade pitch control, for above-rated wind speeds, excites the platform pitch mode, causing unacceptable tower motions [102]. It was then explained that the blade pitch controller used to regulate the rotor speed modifies both the aerodynamic torque and thrust, which directly contributes to aerodynamic damping, coupling the rotor with the platform pitch [39]. This coupling is not unique for FWTs, though, as it was shown that it also existed in onshore turbines due to tower fore-aft bending mode [105]. The aerodynamic damping varies with the wind speed, as it is positive in the below-rated region, but negative in the above-rated one [39, 40, 63]. The main difference is that the fore-aft frequency is significantly lower for FWTs. Usually, the baseline control bandwidth is below the eigenfrequency of the first tower fore-aft mode for onshore turbines, which exceeds the platform pitch eigenfrequency for FWTs. Therefore, the controller may cause severe instability, amplifying the tower motion [39, 40], as illustrated in Fig. 4.1.

Reducing the control bandwidth below the floating platform pitch eigenfrequency while keeping the Single-input, Single-output (SISO) blade pitch Proportional-Integral (PI) control structure was proposed as a solution [39, 40]. However, this makes the controller react very slowly to the rotor speed oscillations [65]. An extra loop was then implemented to add damping by feeding back the tower-top motion to the blade pitch via a proportional (P) controller [40, 63]. This requires an extra sensor, hence, called a Multiple-Input, Single-Output (MISO) controller, which slightly improves the performance, yet with limited bandwidth, as the RHPZs persist. Multiple-Input, Multiple-Output (MIMO) controllers can help increase the controller bandwidth beyond the platform pitch eigenfrequency, and thus, overcome the bandwidth limitation [60]. Accordingly, a MIMO controller was proposed in [65] by using the generator torque as an extra actuator instead of the blade pitch in the MISO case, as the tower-top velocity is fed back to the generator torque this time using a decentralised MIMO controller. As a result, the bandwidth limitation vanishes, as the extra loop compensates for the Right Half Plane Zeros (RHPZs). Later, it was reported that feeding back the platform pitch velocity instead is preferable, as it provides extra filtering [106]. Moreover, centralised model-based control approaches as H_∞ , Linear Quadratic Regulator (LQR), and Non-linear Model Predictive Control (NMPC), are discussed in the literature [60]. Furthermore, feedforward control has proven to be a promising technology with the help of wind and wave previews [53, 75].

The contribution of this paper is twofold:

1. We show that a Single-Input, Multiple-Output (SIMO) feedback controller, relying on the rotor speed measurement as a single input and both the blade pitch and generator torque as multiple outputs, also lifts the RHPZs limitation.
2. A fixed-structure feedback controller, based on the synthesised SIMO controller, is introduced to meet the industrial demand for low-order parameterised controllers.

The paper is organised as follows. In Section 4.2, the FWT model is introduced, as well as the negative damping instability. Section 4.3 demonstrates the different conventional control strategies proposed to tackle that instability. The newly developed control structure

is explained in Section 4.4. Finally, the results of the optimised controller are discussed in Section 4.5 before concluding in Section 4.6.

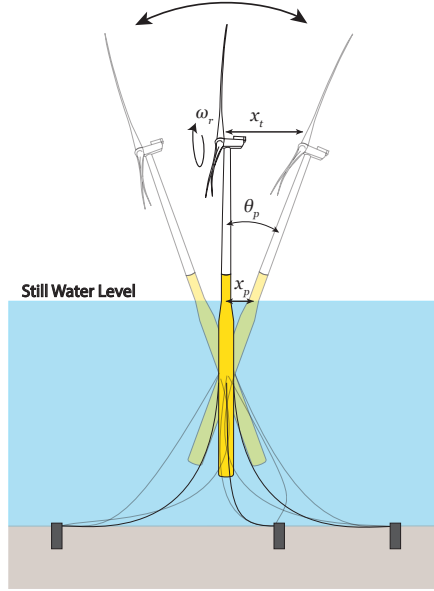


Figure 4.1: A scenario where the platform pitch, θ_p , creates a platform surge, x_p , at the centre of flotation. Similarly, this pure platform pitching creates a linear tower top displacement, x_t , at the nacelle.

4.2 Floating Wind Turbine description

For this study, we used the NREL 5 MW Reference Wind Turbine (RWT) [17] atop the OC3 spar floating platform [18].

It is worth mentioning that the controllers in this paper are investigated at wind speed 14 m/s.

4.2.1 Floating Wind Turbine Model

To address the problem, a simplified mathematical model, including the rigid body platform pitch mode in still water and the rotor dynamics, is used. Equation (4.1) describes the FWT dynamics in the pitch mode as:

$$M_t \ddot{\theta}_p + B_t \dot{\theta}_p + K_t \theta_p = F_{th} l_{hub}, \quad (4.1)$$

where θ_p is the platform-pitch angle (rad), $\dot{\theta}_p$ is the platform-pitch velocity (rad/s), $\ddot{\theta}_p$ is the platform-pitch acceleration (rad/s²), M_t is the overall mass comprising both the structural and added masses of the FWT in pitch, B_t is the overall damping including the hydrodynamic radiation damping and the linearised viscous damping in pitch, K_t is the overall stiffness including the hydrodynamic stiffness and the linearised mooring stiffness

in pitch, F_{th} is the thrust force (N), and l_{hub} is the hub height (m). With the thrust force expressed in Eq. (4.2).

$$\begin{aligned} F_{th} &= \frac{1}{2} \rho \pi R^2 v_{rel}^2 C_T(\lambda, \beta_c) \\ &= \frac{1}{2} \rho \pi R^2 (v - l_{hub} \dot{\theta}_p)^2 C_T\left(\frac{\omega_r R}{v_{rel}}, \beta_c\right), \end{aligned} \quad (4.2)$$

where ρ is the air density (kg/m^3), R is the rotor diameter (m), v_{rel} is the rotor effective wind speed (m/s), v is the free-stream wind speed (m/s), C_T is the thrust coefficient, λ is the tip speed ratio, ω_r is the rotor speed (rad/s), and β_c is the blade pitch angle (rad).

The surge mode is acceptably damped by the mooring lines and thus not considered [60]. Unlike the surge mode, the pitch mode is insufficiently damped; hence, motions increase uncontrollably in this mode. Only F_{th} is considered because of the coupling between the blade pitch control and the aerodynamic thrust. However, there is no coupling between the wave forces and the pitch control, and thus, waves are excluded.

To explicitly see the effect of F_{th} on the platform-pitch damping, F_{th} is linearised around an operating point, and θ_p is replaced with the tower-top translational displacement, x_t . As for small pitch angles, $x_t = l_{hub} \theta_p$, this results in Eq. (4.3).

$$\begin{aligned} \underbrace{\frac{M_t}{l_{hub}^2}}_M \ddot{x}_t + \underbrace{\left(\frac{B_t}{l_{hub}^2} + \frac{\partial F_{th}}{\partial v} \right)}_B \dot{x}_t + \underbrace{\left(\frac{K_t}{l_{hub}^2} \right)}_K x_t &= \frac{\partial F_{th}}{\partial \omega_r} \omega_r \\ &+ \frac{\partial F_{th}}{\partial v} v + \frac{\partial F_{th}}{\partial \beta_c} \beta_c \end{aligned} \quad (4.3)$$

The rotor is modelled using Eq. (4.4) with the aerodynamic torque, τ_g , linearised about an operating point that is a function of the wind speed as:

$$\dot{\omega}_r = \frac{1}{J_d} \left(\frac{\partial \tau_a}{\partial \omega_r} \omega_r - \frac{\partial \tau_a}{\partial v} \dot{x}_t + \frac{\partial \tau_a}{\partial v} v + \frac{\partial \tau_a}{\partial \beta_c} \beta_c - N_g \tau_g \right) \quad (4.4)$$

Combining the linear models of the rotor dynamics and the platform pitch described in Eq. (4.3) and Eq. (4.4), respectively, yields a state space-model with a state vector, $x(t) = [x_t, \dot{x}_t, \omega_r]^\top$, and an input vector, $u(t) = [\tau_g, \beta_c, v]^\top$. The state-space model following $\dot{x}(t) = Ax(t) + Bu(t)$ is:

$$\begin{aligned} \dot{x}(t) &= \begin{bmatrix} 0 & 1 & 0 \\ -\frac{K}{M} & -\frac{1}{M} \left(B + \frac{\partial F_{th}}{\partial v} \right) & \frac{1}{M} \frac{\partial F_{th}}{\partial \omega_r} \\ 0 & -\frac{1}{J_d} \frac{\partial \tau_a}{\partial v} & \frac{1}{J_d} \frac{\partial \tau_a}{\partial \omega_r} \end{bmatrix} \begin{bmatrix} x_t \\ \dot{x}_t \\ \omega_r \end{bmatrix} \\ &+ \begin{bmatrix} 0 & 0 & 0 \\ 0 & \frac{1}{M} \frac{\partial F_{th}}{\partial \beta_c} & \frac{1}{M} \frac{\partial F_{th}}{\partial v} \\ -\frac{N_g}{J_d} & \frac{1}{J_d} \frac{\partial \tau_a}{\partial \beta_c} & \frac{1}{J_d} \frac{\partial \tau_a}{\partial v} \end{bmatrix} \begin{bmatrix} \tau_g \\ \beta_c \\ v \end{bmatrix}, \end{aligned} \quad (4.5)$$

where $\dot{x}(t)$ is the the state derivative vector, A is the system dynamics matrix, and B is the input matrix. The transfer functions in the Laplace domain, $G(s)$, from the inputs, $u(t)$, to the outputs, $y(t) = Cx(t)$, required for the controller design, can be obtained by applying $G(s) = C(sI - A)^{-1}B$. Accordingly, the TF $G_{\beta_c \rightarrow \omega_r}$, mapping β_c to ω_r , is:

$$G_{\beta_c \rightarrow \omega_r} = \frac{Ms^2 + \left[B + \frac{\partial F_{Th}}{\partial v} - \frac{\partial \tau_a}{\partial v} \frac{\partial F_{Th}}{\partial \beta_c} \left(\frac{\partial \tau_a}{\partial \beta_c} \right)^{-1} \right] s + K}{\left(J_d s - \frac{\partial \tau_a}{\partial \omega_r} \right) (Ms^2 + \left[B + \frac{\partial F_{Th}}{\partial v} \right] s + K) + \frac{\partial \tau_a}{\partial v} \frac{\partial F_{Th}}{\partial \omega_r} s} \quad (4.6)$$

Setting the numerator in Eq. (4.6) to zero shows that RHPZs emerge if:

$$B < \frac{\partial F_{Th}}{\partial v} - \frac{\partial \tau_a}{\partial v} \frac{\partial F_{Th}}{\partial \beta_c} \left(\frac{\partial \tau_a}{\partial \beta_c} \right)^{-1} \quad (4.7)$$

Analytically, a complex pair of RHPZs appears in $G_{\beta_c \rightarrow \omega_r}$ as shown in Eq. (4.7), if the fore-aft dynamics are not sufficiently damped [65]. The frequency of the RHPZs always coincides with the fore-aft natural frequencies, like the tower bending modes and the platform pitch mode. Should the zeros have a positive real part, an inverse-response behaviour occurs, posing a hard constraint for control design [64]. Thus, the system becomes unstable if excited at or above the RHPZs frequencies [39, 40]. The RHPZs are witnessed around the rated wind speed, but disappear from the plant at higher wind speeds as demonstrated in Fig. 4.2, as they move to the Left Half Plane (LHP) with blade pitching, indicating an increase in the fore-aft damping [105].

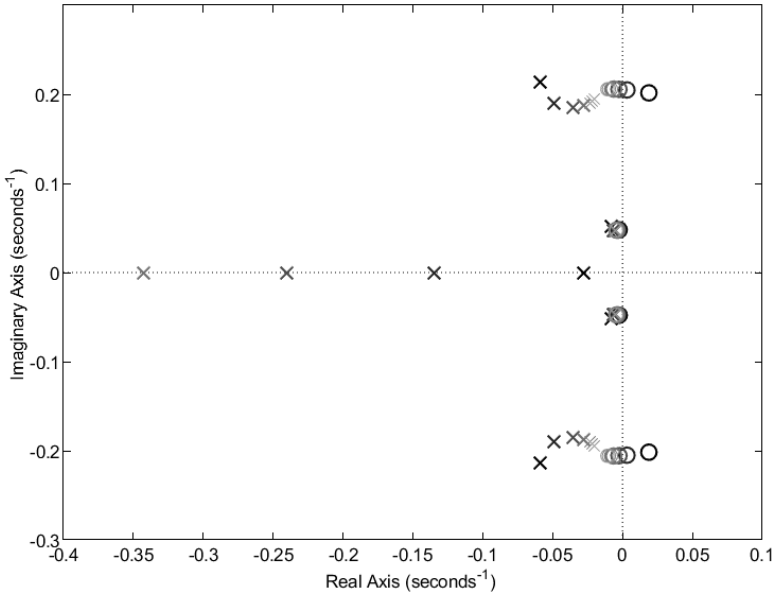


Figure 4.2: Pole-zero plot of the TF from blade pitch to rotor speed, $G_{\beta_c \rightarrow \omega_r}$, at different wind speeds ranging from 12 m/s (darkest) to 24 m/s (lightest).

4.3 Conventional Control Design

Neglecting the floating platform dynamics during the FWT control design often yields instability in the operating points containing RHPZs. This is because of the high control bandwidth triggered by the high feedback control gains, causing platform pitch resonance [40]. At first, one might expect exponential growth in the response due to resonance, but this is not the case due to the non-linear dynamic coupling between the different FWT modes. Yet the FWT keeps oscillating back and forth without reaching steady state, which is still undesirable. There are several ways to mitigate this challenging problem, and thus, in the remainder of this section, the conventional solutions are presented, followed by our proposed solution in the next section.

4

4.3.1 Detuning

One way to overcome resonance is to reduce the bandwidth of the blade pitch controller to be lower than the platform's natural frequency [39, 40, 63]. This leads to overcome resonance, but at the expense of the generator speed tracking performance at the operating points where detuning is applied. A more robust approach uses the linear model to account for the stability margin to be above some threshold and tunes the controller to the fastest possible response at each operating point [60].

4.3.2 Parallel Compensation (MISO & MIMO)

The conventional approach to tackling the negative damping instability includes the closure of a parallel loop, feeding back the tower fore-aft motion, measured at the nacelle. This method is known as "parallel compensation" [63]. Parallel compensation can be attained by blade pitch [63], or generator torque actuators [65], which is a step towards MIMO control. This method attempts to reduce the coupling between the competing aerodynamics of rotor torque and thrust while regulating generator speed through blade pitch. In this study, the fore-aft velocity signal used for parallel compensation is the tower-top pitch rate, which is identical to the platform pitch rate assuming a rigid tower. Both blade pitch and generator torque are considered for parallel compensation in this work, and a combination of both is shown to be a good compromise between the benefits and drawbacks of each. In Eq. (4.5), element $A(3,2)$ demonstrates the state transition term from the fore-aft motion, \dot{x}_t , to the rotor acceleration, $\ddot{\omega}_r$. Setting this term to 0 reduces the platform-pitching effect on rotor speed tracking. With this tuning method, the parallel compensation feedback does not reduce the platform motion directly but compensates for the effect that the platform motion has on generator speed regulation instead, which increases the overall closed-loop system stability.

1. **Blade pitch (MISO control):** Parallel compensation using blade pitch feedback, as shown in Fig. 4.3, is achieved by adding an extra term to element $A(3,2)$, corresponding to the closure of the parallel extra feedback loop, where the parallel compensation gain is scheduled to be consistent with the PI controller gains for each operating point. The blade pitch parallel compensation uses proportional feedback of the tower-top velocity due to the platform pitch rate:

$$\beta = -k_\beta \dot{x}_t \quad (4.8)$$

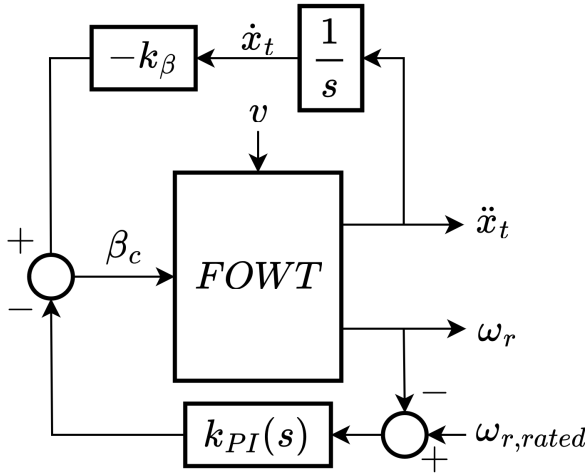


Figure 4.3: Block diagram of the blade pitch parallel compensation (MISO controller)

This extra blade pitch in Eq. (4.8) is added to the blade pitch command from the PI controller before the actuator saturation limits are applied. By closing the parallel loop in Fig. 4.3, a term $k_\beta \frac{1}{J_d} \frac{\partial \tau_a}{\partial \beta_c}$ is subtracted from $A(3,2)$ in Eq. (4.5). Solving for a gain that makes $A(3,2) = 0$ leads to full compensation of the effect of platform pitch on the rotor speed. However, due to blade pitch coupling with both aerodynamic torque and thrust, such a gain reduces the effective system fore-aft damping as a side effect. It is, therefore, sensible to choose a smaller gain to partially compensate the fore-aft motion, which can be achieved by multiplying the parallel compensation gain by a static gain, ξ_β . The parallel compensation gain for blade pitch then becomes

$$K_\beta = -\xi_\beta \frac{\partial \tau_a}{\partial v} \left(\frac{\partial \tau_a}{\partial \beta} \right)^{-1} \quad (4.9)$$

The sign of ξ_β determines the control objective of the extra blade pitch loop. If $\xi_\beta \in [0, 1]$, the effect of the tower-top motion on the rotor speed is thus eliminated at the expense of less fore-aft damping, however, this loop requires extra filtering to change its dynamics, otherwise, it becomes unstable [35]. Whereas, if $\xi_\beta \in [-1, 0]$, the fore-aft damping is improved, while the drivetrain damping decreases, thus less rotor speed tracking performance. Although the MIMO plant does not have any transmission zeros, the poor rotor speed tracking performance can be referred to the persistence of the RHPZs in $G_{\beta_c \rightarrow \omega_r}$, as they are not affected by the parallel loop, and still impose a limitation on the PI controller bandwidth.

2. **Generator torque (MIMO control):** Instead of using the blade pitch in the parallel loop, generator torque can be used instead, as illustrated in Fig. 4.4, thus taking a step towards MIMO control. Unlike the blade pitch, the generator torque compensation

is different, as when $G_{\beta_c \rightarrow \omega_r}$ is closed with the generator torque parallel loop, the RHPZs move to the LHP. With enough gain, the system becomes minimum phase. At optimal gain, pole-zero cancellation occurs, leading the RHPZs to vanish from $\tilde{G}_{\beta_c \rightarrow \omega_r}$, which is the TF representing $G_{\beta_c \rightarrow \omega_r}$ after closing the generator torque parallel loop. Consequently, the bandwidth of the PI controller can be increased above the platform pitch mode. Applying the same tuning procedure as in blade pitch, we end up with:

$$K_{\tau_g} = \xi_{\tau_g} \frac{1}{N_g} \frac{\partial \tau_a}{\partial v} \quad (4.10)$$

4

The main drawback of this approach is the generator torque limit for parallel compensation that can be supplied by the actuator. The usage of the full-compensation gain ($\xi_{\tau_g} = 1$) eliminates the RHPZs, thus turning the system to minimum phase for all operating points; however, the constraint imposed by the τ_g saturation restrains actuator signals exceeding the maximum generator torque. Reducing the compensation gain with $\xi_{\tau_g} \in [0, 1]$ is rather advantageous in practice, as on one hand, it prohibits the generator torque actuator from saturating, and on the other hand, it reduces the drivetrain loads [65]. With $\xi_{\tau_g} < 1$, RHPZs are partially compensated giving the opportunity for higher achievable bandwidth and, hence, improved performance.

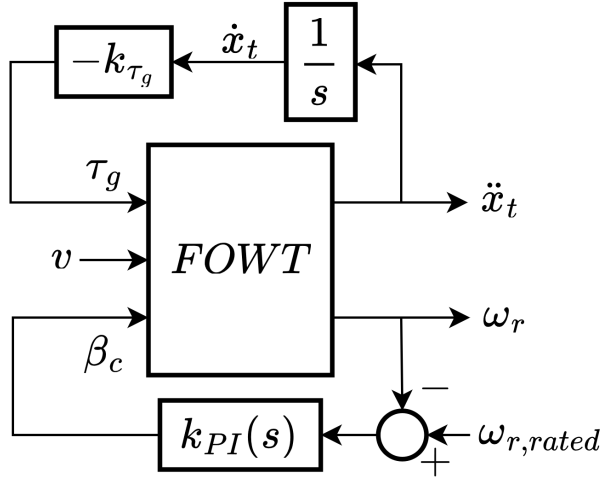


Figure 4.4: Block diagram of the generator torque parallel compensation (MIMO controller)

4.4 SIMO Control

In this section, we present a new control structure, which is illustrated in Fig. 4.5. In this control structure, we have a SIMO controller that only has the rotor speed error as input and both the blade pitch and generator torque as outputs. Unlike the conventional solutions,

finding a SIMO controller is not straightforward. So, we rely on the \mathcal{H}_∞ formulation for the control synthesis. Based on the synthesised SIMO controller, a fixed structure controller with a matching performance, composed of simple elements, is designed in an industry-standard way.

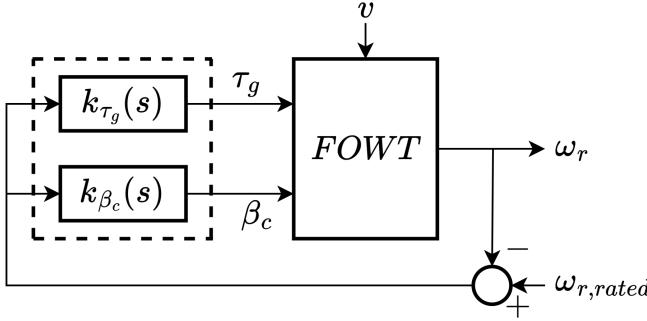


Figure 4.5: Block diagram of the SIMO controller enclosed by the dashed lines.

\mathcal{H}_∞ control synthesis makes use of the general control configuration, in Fig. 4.6, where P is the generalised plant, and K is the synthesised controller. The objective is then to minimise the \mathcal{H}_∞ norm of the transfer function from the exogenous inputs, w , to performance outputs, z [89]. The control synthesis problem is then to find a controller, K , that minimises the infinity norm, $\|N\|_\infty < 1$.

The generalised plant is typically used to synthesise \mathcal{H}_2 or \mathcal{H}_∞ controllers. The advantage of \mathcal{H}_∞ controller design is mainly the ability to shape closed-loop transfer functions and set stability and robustness margins. That is in addition to the possibility for extensions to LPV and robust control.

Here, w is considered the reference rotor speed ($w = \omega_{r, ref}$). While two performance signals, z_1 and z_2 , are specified, with z_1 representing the weighted response penalised by the weight W_p to reduce the effect of w , and z_2 representing the weighted control action penalised by the weight W_u to bound the actuator limits. Signals v and u represent the control input ($\omega_{r, ref} - \omega_r$) and the control action $[\tau_g, \beta_c]^\top$, respectively. As for G , it is TF matrix mapping both τ_g and β_c to ω_r .

In this paper, the \mathcal{H}_∞ controller synthesis considers two criteria to design and evaluate the performance of the controller. The sensitivity, S , and the controller sensitivity, KS , which are defined as

$$S = (I + GK)^{-1}, \quad KS = K(I + GK)^{-1}, \quad (4.11)$$

where S is the TF mapping the disturbance to the system output, while KS is the TF from the disturbance to the control signal. The closed-loop S should be small for low frequencies in order to achieve good disturbance rejection. $W_P(s)$ is chosen to get a slope of 20 dB/dec in $|S|$ for the low-frequency region as follows

$$W_P(s) = \frac{s/M + \omega_B}{s + A\omega_B}, \quad (4.12)$$

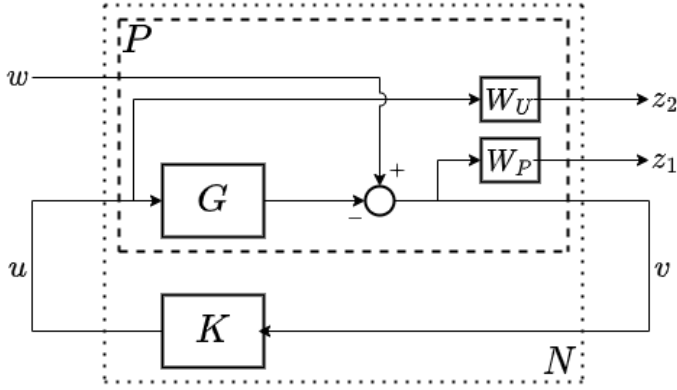


Figure 4.6: Block diagram of the generic model of the generalised plant and controller. The generalised plant $P(s)$ includes all the elements of the system except the controller $K(s)$.

where ω_B is the desired closed-loop bandwidth, A is the desired disturbance attenuation within the closed-loop bandwidth, and M is the desired bound on the sensitivity margin [89]. The controller sensitivity is penalised at high frequencies by W_U .

As mentioned above, the main benefit of H_∞ control synthesis is the ability to shape closed-loop frequency responses. The controller is designed such that based on the information in v , a control signal, u , is generated to counteract the influence of the exogenous inputs, w , on the exogenous outputs, z , by minimising the weighted H_∞ norm of transfer functions from w to z_1 and z_2 . The controller is obtained via the minimisation of the mixed-sensitivity problem with respect to the controller K

$$\min_K \|N(K)\|_\infty = \left\| \begin{bmatrix} W_P S \\ W_U K S \end{bmatrix} \right\|_\infty \quad (4.13)$$

Once the H_∞ SIMO controller is obtained, it serves as a reference for designing a fixed control structure. Subsequently, the fixed-structure could be identified for the SIMO controller, and was found to be composed of an inverted-notch filter at the generator torque input channel, and a PI at the blade pitch input channel, as shown in Fig. 4.5, from which we can observe the significant increase in the bandwidth in both the SIMO H_∞ , and the fixed structure SIMO compared to the rest of the controllers.

4.5 Results

Following the synthesis of the SIMO H_∞ controller, it is observed in Fig. 4.7, that the generator torque channel has a structure close to an inverted notch filter concentrated close to the platform pitch natural frequency, while the blade pitch input channel resembles a simple PI controller. Regarding the RHPZs, we can already see that at the platform pitch eigenfrequency, the τ_g channel has a resonance peak to deal with the existing anti-resonance peak in the plant. At the same time, we see in the magnitude plot of the β_c

channel that there are no resonant peaks, indicating that the PI control is unaffected by the RHPZs anymore.

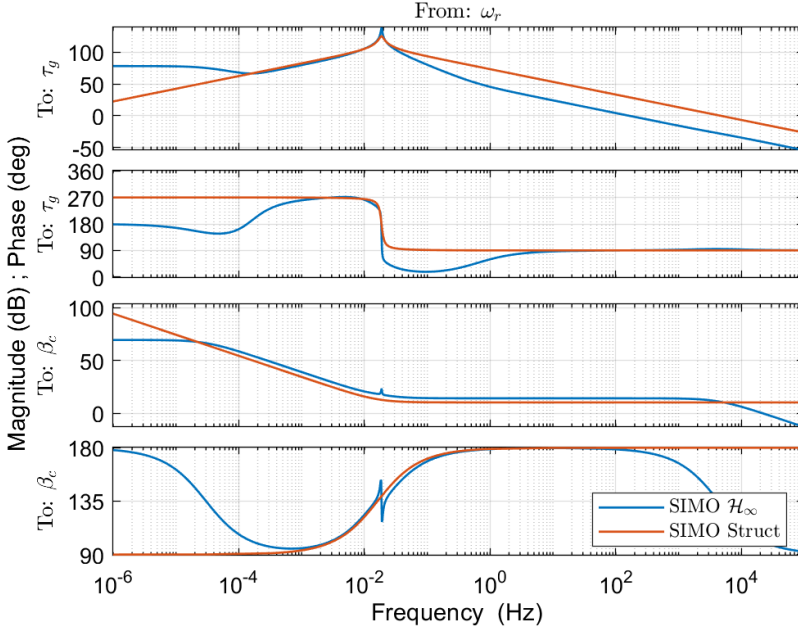


Figure 4.7: Comparison between SIMO \mathcal{H}_∞ and the structured SIMO controllers at wind speed 14 m/s.

Although a fixed-structure SIMO controller, which is close to the synthesised SIMO \mathcal{H}_∞ controller, was achieved, the fixed-structure controller should be implemented with great caution, as the SIMO \mathcal{H}_∞ one is a feedback controller that does not require any prior loop closures. On the other hand, the fixed-structure SIMO control loops can be closed either simultaneously or sequentially. Assuming sequential loop closure as a step towards industry, the generator torque loop must be closed first with the inverted-notch filter to manipulate the RHPZs and move them to another unimportant output channel, before closing the blade pitch loop with the PI controller that, in theory, should now have a much higher bandwidth than the baseline one. In practice, the bandwidth would still be limited by other unstable modes in addition to the actuators' saturation limit, as mentioned before. However, the blade pitch loop must not be closed first by any means; otherwise, instability occurs.

The performance of the different controllers is compared in a linear fashion using the sensitivity function, S , which is illustrated in Fig. 4.8.

Figure 4.8 shows the superiority of the SIMO controller compared to the other ones. As it is clear how high the closed-loop bandwidth can be compared to the other cases, where the bandwidth is defined as the frequency where the sensitivity crosses -3 dB from below. This indicates that the RHPZs bandwidth limitation is lifted with the SIMO controller. It

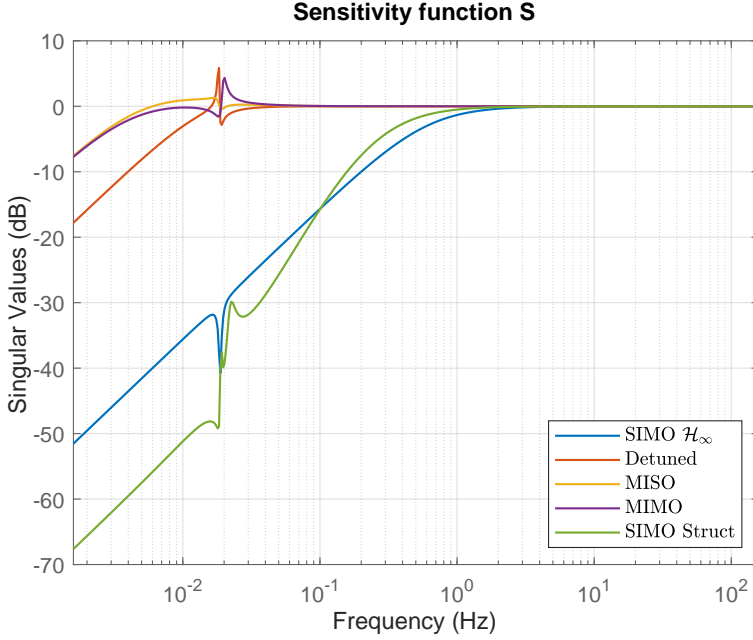


Figure 4.8: Sensitivity function of the different controllers at wind speed 14 m/s.

also shows that with just a single measurement (rotor speed), a controller exists that can tackle the negative damping instability, instead of using a second measurement (tower-top motion) and turn into full MIMO control.

4.6 Conclusion

A generalised framework was set up for the \mathcal{H}_∞ synthesis of a SIMO feedback controller for the rotor speed regulation of floating wind turbines, from which a simple control structure for industry standards was derived. Rotor speed oscillation minimisation was included in the controller synthesis. An \mathcal{H}_∞ SIMO controller was obtained that was then reduced to a fixed-structure SIMO controller, which is composed of simple elements as an inverted-notch and a PI controller. Should sequential loop closure be applied to the fixed-structure controller, the correct order of loop closures must be followed, otherwise, instability arises.

5

Control Design for Floating Wind Turbines

5

While the generator speed feedback control of onshore wind turbines, via the pitch controller to feather the blades, is well-established, employing the same controller gains with floating offshore wind turbines causes the turbines to become unstable. Such instability is attributed to the coupling between the nacelle fore-aft motion and the wind turbine controller, which makes the wind turbine negatively damped. The non-minimum phase zeros existing in the transfer function from the blade pitch to the generator speed impose a fundamental limitation on the closed-loop bandwidth, posing a challenge to the operation of the floating turbines. This paper gives an overview of the control strategies and their tuning techniques employed for floating wind turbines in the presence of the negative damping instability. It discusses the different available strategies. Moreover, we propose a new controller that can alleviate the adverse effects of the negative damping while preserving the standard proportional-integral control structure. Contrary to the multi-input-multi-output controllers that have been proposed, the proposed controller is more robust since it does not require additional signals of the floating platform, which makes controllers often sensitive to unmodelled dynamics. The controller is compared against the previously proposed controllers using the non-linear simulation tool, OpenFAST. The proposed controller excels in regulating generator speed, surpassing other controllers in performance. Additionally, it effectively mitigates the platform pitch in addition to the tower and blade loads. However, achieving a balance between power quality, actuator usage, and structural loading presents inherent trade-offs that need to be carefully addressed.

Parts of this chapter are based on:

📄 Hegazy, A., Naaijen, P., and van Wingerden, J.W.: Control design for floating wind turbines, Wind Energy Science Discussions, [preprint], doi: 10.5194/wes-2025-68, in review, 2025.

5.1 Introduction

Wind energy is essential to meeting the decarbonisation objectives of the European Union (EU) energy system, as it ensures delivering clean, affordable and secure electricity to various sectors, including households, industry and transport. Consequently, wind energy is expected to heavily contribute to the EU renewable energy targets. This is not surprising, especially when we know that in 2024, wind energy covered 19% of the EU electricity demand. No wonder the EU is regarded as a pioneer in wind energy. Accordingly, this has seen the EU revising the renewable energy directive, which lays down a minimum binding target of 42.5% share of renewables by 2030 with an aspiration to reach 45%. This is 10.5% higher than the initial 32% target. Subsequently, the EU could fulfil its ambition of becoming climate-neutral by 2050 [82].

As of 2025, Europe boasts a total installed wind capacity of approximately 285 gigawatts (GW), marking a significant expansion in the region's renewable energy infrastructure. Wind power accounts for almost 20% of Europe's electricity consumption nowadays, and projections indicate that this figure could rise in the future. The EU aims to increase its wind capacity from 225 GW today to 350 GW by 2030, with a target of 425 GW to align with ambitious energy security goals [4].

Offshore wind offers significant advantages over onshore wind due to higher wind speeds and more consistent wind directions. Floating Offshore Wind Turbines (FOWTs) present unique opportunities as they can be deployed in deeper waters and farther from shore compared to bottom-fixed turbines. This expands the potential for offshore wind development in regions with deeper sea basins, such as the Mediterranean and the Atlantic. However, FOWTs face harsher environmental conditions than onshore turbines. Unlike onshore turbines, FOWTs are subjected to additional disturbances caused by waves, which contribute to increased structural loading on top of the loads induced by wind turbulence. As a result, FOWTs experience higher fatigue loads due to the added impact of waves [91].

The cost of energy defines the potential of one type of energy source to be preferred over another, with the Levelised Cost Of Energy (LCOE) being the metric representing the average cost of generating electricity over the lifetime of a power-generating asset, expressed in monetary terms per unit of electricity. The main challenge facing the further deployment of FOWTs is their high LCOE. While modifications to their aerodynamic, hydrodynamic and structural design are applied to bring the LCOE down, the control system should not be overlooked. Developing new control architectures can contribute to reducing the LCOE. Another approach is control co-design [107], which has proven to be highly effective.

From a control perspective, FOWTs present additional complexities compared to onshore turbines. The dynamics introduced by the floating platform make control more challenging. A notable concern is the negative damping effect [61], as applying a fixed-bottom controller to a floating wind turbine can significantly amplify the system's dynamic response, leading to large oscillations. The simplest way to avoid closed-loop instability without modifying the conventional baseline controller structure is to detune the control gains such that the closed-loop response of the generator speed mode in isolation has a natural frequency below the platform pitch resonant frequency [39, 40]. However, this leads to a degradation in the reference tracking performance of the blade pitch controller as its ability to effectively respond to disturbances becomes restricted [60, 108]. Maintaining

global detuning across all wind speeds sacrifices higher control bandwidths at higher wind speeds that do not suffer from this instability. Accordingly, it is reasonable to schedule the detuning at each wind speed separately [60, 67, 108, 109].

Other methods explored in the literature involve incorporating extra feedback loops to counteract the instability arising from rotor-platform interactions. By utilising nacelle fore-aft velocity as feedback to adjust the existing baseline controller actuators, blade pitch [40, 63, 103] and generator torque [65, 106] control inputs showed performance improvements could be achieved without the need for additional actuators. Systems with more than one actuating control input and more than one sensor output may be considered as multivariable systems or Multi-Input-Multi-Output (MIMO) systems. The control objective for multivariable systems is to obtain a desirable behaviour of several output variables by simultaneously manipulating several input channels. A FOWT is a MIMO system. To evaluate such a system, MIMO transfer function matrix is needed. In many FOWT control strategies, the feedback control loops are often designed separately in a decoupled format, with each control loop tuned to improve the response of a specific output [110]. This means that the multivariable controller design is reduced to a series of single-loop controllers. Although this approach is common, the loops in a MIMO system are dynamically coupled. As a result, changing the settings of one control loop can affect the behaviour of other loops, causing interaction between them. Subsequently, the interaction between the different control loops of a system should be dealt with simultaneously. It was demonstrated that improved performance could be achieved when optimally tuning all the control loops collectively accounting for the interdependencies within the MIMO feedback structure rather than tuning each control loop independently [67]. Modern multivariable control methodologies employing state-feedback architectures, including Linear Quadratic Regulator (LQR) [50] and H_∞ control [83, 111] demonstrate systematic efficacy in achieving specified stability and performance envelopes for complex dynamical systems [89].

This paper provides a tutorial on the design of closed-loop controllers for FOWTs, outlining various control strategies proposed in the literature. It also evaluates the performance of these strategies, particularly in addressing the negative damping instability. Additionally, a novel controller structure is introduced, which eliminates the need for additional sensors, along with a detailed tuning technique.

The remainder of this paper is structured as follows: In Section 2, the FOWT control problem is defined, and the control design model is introduced. In Section 3, conventional Single-Input Single-Output (SISO) and MIMO control strategies are discussed. In Section 4, the controllers are evaluated by simulating the closed-loop system using the non-linear aero-servo-hydro-elastic tool OpenFAST [112].

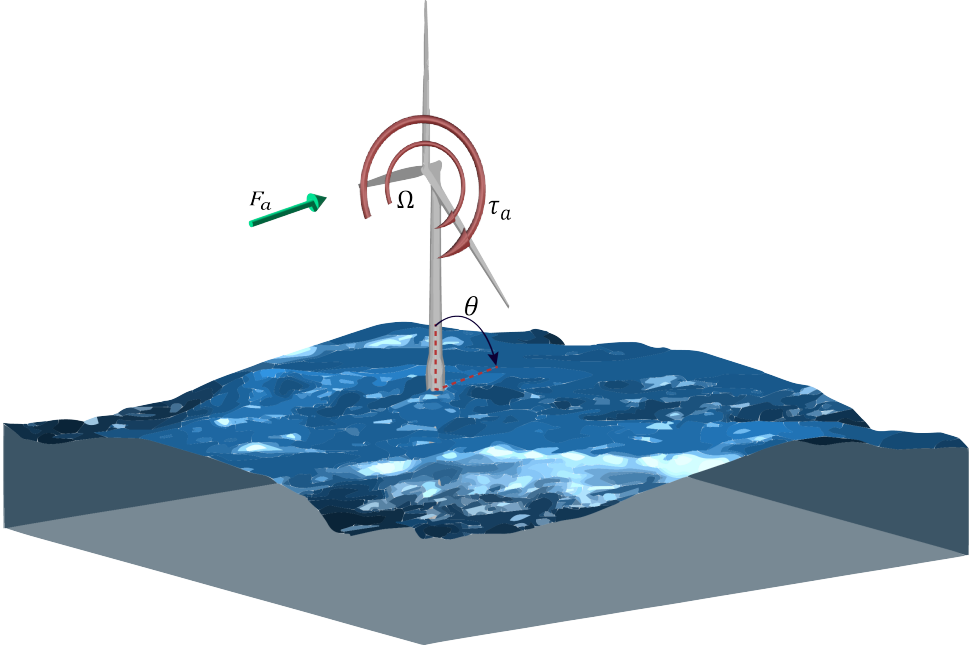


Figure 5.1: Schematic of the FOWT depicting the generator speed, Ω , and the platform pitch, θ , DoFs of the simple control model together with the external forces, namely, the aerodynamic thrust, F_a , and torque, τ_a , as expressed in Eq. (5.14).

5.2 Problem background

In this section, we start by introducing the dynamic model of a conventional fixed-bottom wind turbine. Afterwards, we go on to explain the process of closing the loop with the baseline controller and the tuning methodology of the controller gains. Once this is established, we move on to the FOWTs where we introduce the additional dynamics for the floating platform to form a representative dynamic model of a FOWT to conduct further analysis on the complexities that arise when controlling FOWTs.

Conventional wind turbine dynamics are excited by the imbalance between the aerodynamic torque and the generator torque, which drives the generator speed, and thus a simplified wind turbine model is described as:

$$\frac{J_r}{N_{gb}} \dot{\Omega} = \tau_a(\Omega, \beta, v) - N_{gb} \tau_g, \quad (5.1)$$

where J_r (kg.m^2) is the rotor drivetrain inertia, Ω (rad.s^{-1}) is the generator speed with the dot notation indicating the time derivative, τ_a (N.m) is the aerodynamic torque, N_{gb} (-) is the gearbox ratio, and τ_g (N.m) is the generator torque. The aerodynamic torque $\tau_a(\Omega, \beta, v)$ is modelled by a non-linear function:

$$\tau_a = \frac{1}{2} \rho \pi R^2 N_{gb} \frac{v^3}{\Omega} C_p(\lambda, \beta), \quad (5.2)$$

with ρ (kg.m^{-3}) as the air density, R (m) being the rotor radius, $C_p(\lambda, \beta)$ as the power coefficient, which depends on the blade pitch angle, β (rad), and the tip-speed ratio, $\lambda = \Omega R / v N_{gb}$, with v (m.s^{-1}) being the wind speed normal to the rotor plane. Around an equilibrium point, \bar{x} , a perturbation state, δx , is defined as $\delta x = x - \bar{x}$, and a non-linear function $f(\bar{x}) = 0$. Therefore, the non-linear wind turbine dynamics in Eq. (5.1), at steady-state, can be linearised using first-order Taylor series expansion around an equilibrium point as:

$$\delta \dot{\Omega} = \frac{N_{gb}}{J_r} \left(\frac{\partial \tau_a}{\partial \Omega} \delta \Omega + \frac{\partial \tau_a}{\partial v} \delta v + \frac{\partial \tau_a}{\partial \beta} \delta \beta - N_{gb} \delta \tau_g \right), \quad (5.3)$$

where the partial derivatives of τ_a with respect to its independent variables are known as the aerodynamic sensitivities.

In practice, wind turbines are regulated with a generator speed controller, as at below-rated wind speeds, the controller is seeking to maximise the extracted power by keeping the collective blade pitch angle, β , constant while varying the generator torque, τ_g , as a function of the square of the generator speed, Ω , as follows [30]:

$$\tau_g = k_g \Omega^2, \quad (5.4)$$

with $k_g = 0.5 \rho \pi R^2 (C_{p,max} / N_{gb}^3 \lambda_{opt}^3)$, being the generator-torque constant. The variable $C_{p,max}$ is the maximum power coefficient achieved at the optimal Tip-Speed Ratio (TSR), λ_{opt} , and at a specific constant blade pitch angle known as fine blade pitch angle. Although simple, the controller in Eq. (5.4) operates under the assumption that k_g remains constant throughout the wind turbine's lifetime. In reality, this is not the case, as it is influenced by modelling inaccuracies and assumption errors. To address this limitation, the TSR tracking controller has proven to be more effective and is widely adopted in the wind energy industry [35, 113].

At above-rated wind speeds (referred to as Region 3), a conventional wind turbine controller relies on the blade pitch to regulate the generator speed to its rated value while keeping the generator torque constant at its rated value [30]. As a result, generator power fluctuations are directly proportional to the oscillations occurring in the generator speed, $\delta \Omega = \Omega - \bar{\Omega}$. The collective blade pitch controller regulates the generator speed about its steady-state value, $\bar{\Omega} = \Omega_{rat}$, according to the following feedback control law:

$$\delta \beta = k_p \delta \Omega + k_i \int \delta \Omega dt, \quad (5.5)$$

where k_p and k_i are the proportional and integral controller gains, respectively. To reach a description of the gains, the azimuth angle ψ is introduced as $\Omega = \dot{\psi}$ in Eq. (5.3) and Eq. (5.5). By combining both equations and focusing on the generator speed terms, we derive a closed-loop system. When rewritten in the standard form of a second-order mass-spring-damper system, it becomes:

$$\delta \ddot{\psi} + \underbrace{\frac{-N_{gb}}{J_r} \left(\frac{\partial \tau_a}{\partial \Omega} + \frac{\partial \tau_a}{\partial \beta} k_p \right)}_{2\zeta_c \omega_c} \delta \dot{\psi} + \underbrace{\frac{-N_{gb}}{J_r} \frac{\partial \tau_a}{\partial \beta} k_i}_{\omega_c^2} \delta \psi = 0. \quad (5.6)$$

Notice that the terms irrelevant to the control problem in Eq. (5.3) were dropped and do not appear in Eq. (5.6). Accordingly, we can parametrise the PI blade pitch controller gains:

$$k_i = -\omega_c^2 \frac{J_r}{N_{gb}} \left(\frac{\partial \tau_a}{\partial \beta} \right)^{-1} \quad (5.7)$$

$$k_p = \left(-2\zeta_c \omega_c \frac{J_r}{N_{gb}} - \frac{\partial \tau_a}{\partial \Omega} \right) \left(\frac{\partial \tau_a}{\partial \beta} \right)^{-1} \quad (5.8)$$

Given a desired natural frequency, ω_c , and damping ratio, ζ_c , the PI controller gains can be computed [114]. By defining the ω_c and ζ_c of the generator speed response, the dynamic response of the rotor to wind speed variations can be altered. The value of ω_c defines the bandwidth of the feedback controller. Typically, the controller bandwidth is chosen below the lowest structural natural frequency of the system to avoid interaction with lightly damped modes, leading to instability. The bandwidth should not include the Right Half Plane Zeros (RHPZs) existing in the wind turbine system as [105] reported. As shown in Eq. (5.7) and Eq. (5.8), their controller gains depend on the aerodynamic sensitivities, which significantly vary across operating points. As a result, the controller gains are scheduled at each operating point and modified during operation as the wind speed changes to maintain consistent closed-loop transient behaviour using a linear controller.

The main challenge associated with the control of FOWTs, within Region 3 concerns their fore-aft motion [39, 40, 63, 65]. Therefore, it is critical to include floating platform dynamics in the control design model.

5.2.1 Floating wind turbine model

The main problem associated with the control of floating wind turbines concerns the pitch stability in full load [39, 40, 63, 65]. The effect of varying wind speed on the steady state thrust, in the above-rated region, has to be considered in order to understand this problem. The above-rated part of the steady state thrust curve, shown in Fig. 5.2, is defined as the thrust force required at a given wind speed to produce rated power at rated generator speed. The steady-state blade pitch angle varies along the operating curve to achieve constant generator torque instead of constant power since this limits the generator speed variations, hence, reduced drive train loads and pitch activity [39]. The objective is to achieve a stable power production with less variations such that its total differential diminishes.

To form a FOWT mathematical model, the generic 1-DOF model of the wind turbine in Eq. (5.3) is combined with the floating platform dynamics. For the sake of explaining the negative damping problem, only a 2-DOF FOWT model capturing the critical dynamics is used, where the platform pitch degree of freedom (DOF) is primarily considered to characterise platform dynamics, as the negative damping instability is most pronounced at the platform pitch eigenfrequency, where there is no damping from the mooring and very little hydrodynamic damping leading to negative damping if the pitch control is fast [39, 40]. However, to preserve key dynamic couplings, the control model used for the control design must include additional modes that capture the most significant system dynamics, namely the platform's surge and heave, and the tower first fore-aft bending [60]; otherwise, some interactions within the system may be overlooked [109]. The non-relevant DOFs are

neglected to avoid accounting for extra states, which would increase the complexity. For this analysis, the NREL 5-MW Reference Wind Turbine (RWT) [17] is mounted on top of the OC3 spar floater [18]. Such analysis was performed in [66, 67, 115] for different FOWT system.

The rigid floating platform pitch motion in still water, thus, affected by the aerodynamic thrust force only without any wave-induced forces, can be modelled as a second-order mass-spring-damper system:

$$I_p \ddot{\theta} + C \dot{\theta} + K \theta = l_h F_a(\Omega, v, \beta), \quad (5.9)$$

where θ is the platform pitch angle, $\dot{\theta}$ is the platform pitch rotational velocity, $\ddot{\theta}$ is the platform pitch rotational acceleration, I_p is the total mass moment of inertia about the platform pitch axis, comprising the structural inertia and the added mass associated with hydrodynamic radiation, C is the damping coefficient, K includes the hydrostatic and the mooring stiffnesses. Within the simplified 2D model, the frequency-dependent radiation memory effects are disregarded by assuming a constant added mass and omitting radiation damping, as it is insignificant compared to viscous damping in FOWT platforms [60, 64], while for the control model, used for control synthesis, a parametric radiation model is used [116, 117]. However, for the time-domain simulations, the convolution integral [118] is incorporated to account for the frequency-dependent coefficients. The variable F_a is the aerodynamic rotor thrust force, which causes a pitching moment on the platform through the hub height, l_h , as a lever arm. The aerodynamic thrust force $F_a(\Omega, \beta, v)$ is a non-linear function is expressed by:

$$F_a = \frac{1}{2} \rho \pi R^2 v^2 C_t(\lambda, \beta), \quad (5.10)$$

where v is the rotor effective wind speed, C_t is the thrust coefficient function in λ and β . The platform pitch motion influences the dynamics as it induces a relative wind speed at the rotor apart from the inflow wind speed, v_∞ . Thus, the rotor effective wind speed, v , is:

$$v = v_\infty - l_h \dot{\theta}. \quad (5.11)$$

Similar to Eq. (5.3) while considering Eq. (5.11), the non-linear platform dynamics can be linearised around an equilibrium point as:

$$I_p \delta \ddot{\theta} + C \delta \dot{\theta} + K \delta \theta = l_h \left(\frac{\partial F_a}{\partial \Omega} \delta \Omega - l_h \frac{\partial F_a}{\partial v} \delta \dot{\theta} + \frac{\partial F_a}{\partial \beta} \delta \beta \right) \quad (5.12)$$

In a standard second-order form, by considering only the coefficients corresponding to the platform pitch motion, Eq. (5.12) can be rewritten as:

$$\delta \ddot{\theta} + \underbrace{\frac{1}{I_p} \left(C + l_h^2 \frac{\partial F_a}{\partial v} \right)}_{2\zeta_p \omega_p} \delta \dot{\theta} + \underbrace{\frac{K}{I_p}}_{\omega_p^2} \delta \theta = 0, \quad (5.13)$$

with ω_p and ζ_p being the natural frequency and the damping ratio of the floating platform in the pitch DoF, respectively.

The coupled dynamics of the wind turbine in Eq. (5.3) and the floating platform in Eq. (5.12) form a third-order system, which is represented in state space form of $\dot{\mathbf{x}} = \mathbf{A}\mathbf{x} + \mathbf{B}\mathbf{u}$, with a state vector $\mathbf{x} = [\theta \ \dot{\theta} \ \Omega]^\top$, and control input vector $\mathbf{u} = [\tau_g \ \beta]^\top$, as:

$$\dot{\mathbf{x}} = \begin{bmatrix} 0 & 1 & 0 \\ A_K^\theta & A_C^\theta & A_\Omega^\theta \\ 0 & A_\theta^\Omega & A^\Omega \end{bmatrix} \mathbf{x} + \begin{bmatrix} 0 & 0 \\ 0 & B_\beta^\theta \\ B_{\tau_g}^\Omega & B_\beta^\Omega \end{bmatrix} \mathbf{u}, \quad (5.14)$$

where the individual elements of the system matrix, \mathbf{A} , and the input matrix, \mathbf{B} , are defined in Table 5.1. The output vector $\mathbf{y} = \mathbf{C}\mathbf{x} + \mathbf{D}\mathbf{u}$, with the output matrix \mathbf{C} and the feed-through matrix \mathbf{D} , is defined according to the available system measurements, which is typically a subset of the states in the state vector \mathbf{x} . In this paper, the output vector is chosen as $\mathbf{y} = [\dot{\theta} \ \Omega]^\top$, and thus obtained for the state-space model in Eq. (5.14) as:

$$\mathbf{y} = \begin{bmatrix} 0 & 1 & 0 \\ 0 & 0 & 1 \end{bmatrix} \mathbf{x}, \quad (5.15)$$

The element A_θ^Ω in the system matrix, \mathbf{A} , in Eq. (5.14) is the state transition term from the platform pitch velocity, $\delta\dot{\theta}$, to the generator acceleration, $\delta\dot{\omega}_g$, which clearly shows the direct effect of the platform pitch motion on the generator acceleration via the term $\frac{-1}{J_r} \frac{\partial \tau_a}{\partial v}$.

Now with such linear state space model, we can view the problem analytically with a pole-zero plot, shown in Fig. 5.3, of the TF, $G_{\Omega,\beta}$, mapping the collective pitch pitch, β , to generator speed, Ω , describing how generator speed (controlled variable) responds to a variation in blade collective pitch angle (control input). First, let us look at the analytical description of $G_{\Omega,\beta}$. This requires transferring to the frequency domain, which can be attained by applying $G(s) = \mathbf{C}(s\mathbf{I} - \mathbf{A})^{-1}\mathbf{B} + \mathbf{D}$, with s being the Laplace variable, and \mathbf{I} being the identity matrix. As a result, we get a MIMO transfer function matrix, $G(s) = G_{uy}(s)$, mapping the input vector \mathbf{u} to the output vector \mathbf{y} . The transfer function matrix $G(s)$ is composed of SISO TF $G_{u_i y_i}(s) = y_i(s)/u_i(s)$ mapping each input $u_i(s)$ to each output $y_i(s)$:

$$G(s) = \begin{bmatrix} G_{\dot{\theta}, \tau_g} & G_{\dot{\theta}, \beta} \\ G_{\Omega, \tau_g} & G_{\Omega, \beta} \end{bmatrix} \quad (5.16)$$

For the feedback control of FOWTs in Region 3, the control objective is to reduce the generator speed oscillations using the blade pitch action. Consequently, the TF, $G_{\Omega,\beta}$, mapping the blade pitch angle to the generator speed, in Eq. (5.16) is of the main interest:

$$G_{\Omega,\beta} = \frac{\frac{\partial \tau_a}{\partial \beta} (I_p s^2 + [C + I_h^2 \frac{\partial F_a}{\partial v}] s + K) - I_h^2 \frac{\partial \tau_a}{\partial v} \frac{\partial F_a}{\partial \beta} s}{\left(\frac{J_r}{N_g b} s - \frac{\partial \tau_a}{\partial \Omega} \right) (I_p s^2 + [C + I_h^2 \frac{\partial F_a}{\partial v}] s + C) + I_h^2 \frac{\partial \tau_a}{\partial v} \frac{\partial F_a}{\partial \Omega} s}, \quad (5.17)$$

where all the gradients vary with the operating point. To determine the zeros of $G_{\Omega,\beta}$, its numerator polynomial is set to zero, and the resulting equation is solved for s using the

Table 5.1: The elements of the system matrices A and B .

Element	Definition
A_K^θ	$-\frac{K}{I_p}$
A_C^θ	$-\frac{1}{I_p} \left(C + I_h^2 \frac{\partial F_a}{\partial v} \right)$
A_Ω^θ	$\frac{l_h}{I_p} \frac{\partial F_a}{\partial \Omega}$
A_θ^Ω	$-l_h \frac{N_{gb}}{J_r} \frac{\partial \tau_a}{\partial v}$
A^Ω	$\frac{N_{gb}}{J_r} \frac{\partial \tau_a}{\partial \Omega}$
B_β^θ	$\frac{l_h}{I_p} \frac{\partial F_a}{\partial \beta}$
$B_{\tau_g}^\Omega$	$-\frac{N_{gb}^2}{J_r}$
B_β^Ω	$\frac{N_{gb}}{J_r} \frac{\partial \tau_a}{\partial \beta}$

quadratic formula. Upon algebraic manipulation, it becomes evident that RHPZs, indicating non-minimum phase behaviour, emerge under the following condition [65]:

$$C < -I_h^2 \underbrace{\left[\frac{\partial F_a}{\partial v} - \frac{\partial \tau_a}{\partial v} \frac{\partial F_a}{\partial \beta} \left(\frac{\partial \tau_a}{\partial \beta} \right)^{-1} \right]}_{\mu_{aero}} \quad (5.18)$$

Equation (5.18) highlights that the emergence of non-minimum phase behaviour, driven by the presence of RHPZs, is closely tied to the aerodynamic damping coefficient (μ_{aero}), which is influenced by aerodynamic gradients. This coefficient varies with the operating conditions and tends to be particularly low near the rated wind speed, as will be demonstrated in the following analysis.

Figure 5.2 illustrates the relationship between the steady-state aerodynamic thrust force (F_a) and the rotor-effective wind speed (v) for the above-rated operation of the NREL 5-MW reference wind turbine [17] installed on the OC3 spar floating platform [18]. In a closed loop FOWT system at steady state, the gradient dF_a/dv is positive below-rated wind speed, meaning the thrust force increases as wind speed rises. However, beyond the rated wind speed, this gradient becomes negative, as shown in Fig. 5.2. This behaviour results from the pitch-to-feather control strategy, which reduces aerodynamic loads and modifies

the force direction in the above-rated region. As a consequence, aerodynamic damping is positive at below-rated wind speeds but turns negative at above-rated wind speeds. As F_a begins with a positive slope ($\mu_{aero} > 0$) in Region 2, where F_a keeps increasing till reaching its maximum at the rated wind speed where $\mu_{aero} = 0$. Once Region 3 is reached, F_a starts decreasing with a significantly steep negative slope ($\mu_{aero} < 0$). The steeper this decline, the lower the aerodynamic damping, with its minimum occurring just beyond the rated wind speed. As wind speed continues to increase, the slope gradually becomes less steep, indicating a partial recovery of aerodynamic damping.

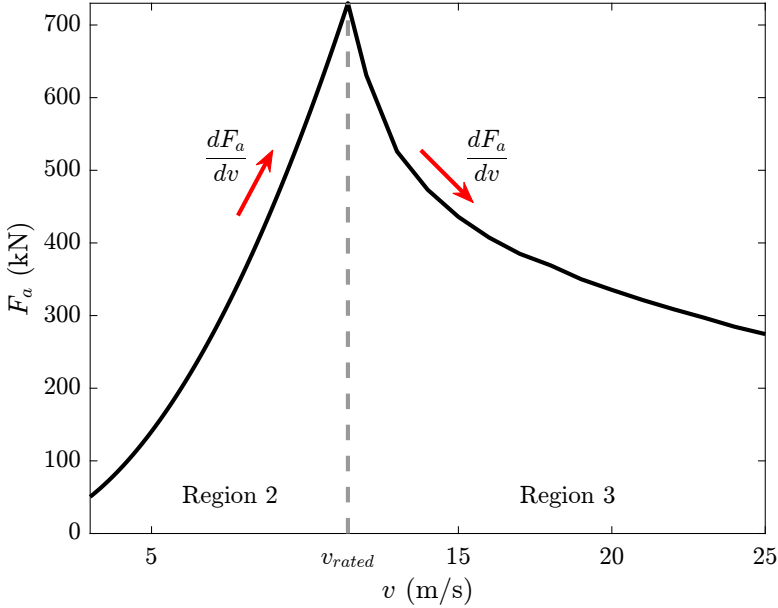


Figure 5.2: Steady-state values of rotor thrust force, F_a , as a function of the effective rotor wind speed, v , for the NREL 5-MW baseline wind turbine on OC3 spar floating platform.

The root cause of this behaviour is the negative total derivative of thrust force with respect to above-rated wind speeds [65] as in Region 3, the rotor speed (Ω_r) is at its constant rated value, while the aerodynamic torque (τ_a) varies. The objective is to achieve stable power production (P) with fewer variations such that its total differential diminishes [63]:

$$dP = \Omega_r d\tau_a = \Omega_r \left(\frac{\partial \tau_a}{\partial v} dv + \frac{\partial \tau_a}{\partial \beta} d\beta \right) = 0, \quad (5.19)$$

and from Eq. (5.19), the total differential of the blade-pitch angle is:

$$d\beta = -\frac{\partial \tau_a}{\partial v} \left(\frac{\partial \tau_a}{\partial \beta} \right)^{-1} dv \quad (5.20)$$

Similar to $d\tau_a$ in Eq. (5.19), the total differential of F_a is:

$$dF_a = \frac{\partial F_a}{\partial v} dv + \frac{\partial F_a}{\partial \beta} d\beta \quad (5.21)$$

Combining Eq. (5.20) and Eq. (5.21), the total derivative of the aerodynamic thrust with respect to the wind speed, yielded from the variation of blade pitch to maintain rated power, is:

$$\frac{dF_a}{dv} = \frac{\partial F_a}{\partial v} - \frac{\partial F_a}{\partial \beta} \frac{\partial \tau_a}{\partial v} \left(\frac{\partial \tau_a}{\partial \beta} \right)^{-1} = \mu_{aero} \quad (5.22)$$

Equation (5.22) demonstrates why F_a has a negative gradient, $dF_a/dv < 0$, as wind speed increases, a condition that is necessarily true for all conventional pitch-to-feather wind turbines [63]. It is explained that as the wind increases above-rated, the pitch angle increases to maintain constant generator torque, but the aerodynamic thrust and torque decrease, indicating that the gradients $\partial F_a/\partial \beta$ and $\partial \tau_a/\partial \beta$ are negative, which allows the downwind fore-aft motion to decrease, which leads to an upwind fore-aft motion, causing the relative wind speed seen by the rotor to increase [14]. Consequently, the aerodynamic torque increases further, causing more pitch action [40, 63]. So, the gradient $\partial \tau_a/\partial v$ is positive. Therefore, after considering the signs of all the gradients in Eq. (5.22), it becomes clear why $dF_a/dv < 0$ in the above-rated operation.

After obtaining $G_{\Omega,\beta}$ from $G(s)$ in Eq. (5.16), the pole-zero map of $G_{\Omega,\beta}$, that maps the blade collective pitch, β , to the generator speed, Ω , describing how the generator speed responds to a variation in blade pitch angle, is shown in Fig. 5.3.

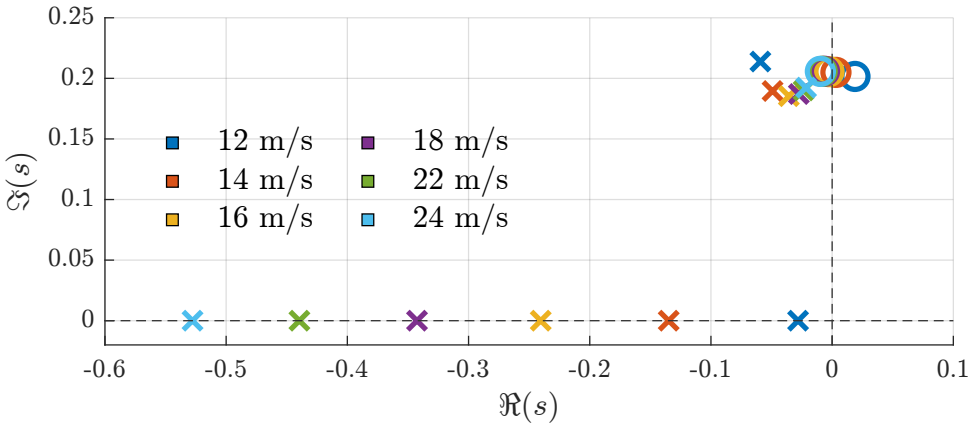


Figure 5.3: Pole-Zero map of the TF from blade collective pitch to rotor speed, $G_{\Omega,\beta}$, at different operating points. Poles and zeros are denoted by \times and \circ , respectively.

Figure 5.3 shows that the TF, $G_{\Omega,\beta}$, consists of a complex pole pair, corresponding to the platform rigid-body pitch mode, and a real pole, associated with the drivetrain mode. Additionally, a complex pair of RHPZs appears at a frequency close to that of the platform pitch mode, indicating that the RHPZs condition in Eq. (5.18) is satisfied. The poles in the platform pitch mode of the open-loop transfer function, $G_{\Omega,\beta}$, correspond to

the pitch-free decay damping ratio, ζ_p , and natural frequency (eigenfrequency), ω_p . It can be seen in Fig. 5.3 that the open-loop system is originally stable because of the sufficient hydrodynamic damping [108] since all the poles are in the left-half-plane.

However, the closed-loop poles of a system would migrate from the open-loop poles location towards the open-loop zeros as the feedback gain increases [63]. Hence, according to Fig. 5.3, the platform pitch mode becomes less damped, whilst the generator speed tracking improves. In the case where the zeros are in the right half plane, which for the model visualized in Fig. 5.3 is true only for the platform pitch zeros, the frequencies provide bandwidth limits on $G_{\Omega,\beta}$ loop.

5.2.2 Effect of RHP zeros

The roots of the numerator of a transfer function are called zeros (denoted by \circ in Fig. 5.3). A zero represents a critical frequency, referred to as the frequency of the zero, where the input signal is entirely blocked and has no effect on the system's output. In particular, RHPZs exhibit an "inverse-response behaviour," meaning the system output initially moves in the opposite direction of the expected response [89]. This unique characteristic imposes strict constraints on control system design, especially in SISO configurations [64]. Additionally, when the system is excited at or near the frequency of the zero, the risk of instability increases significantly. To mitigate this, limiting the controller bandwidth below the smallest RHPZ frequency is a must [89].

The effects of RHPZs extend beyond simple instability risks. As detailed in [119], RHPZs introduce phase loss, which diminishes the performance of closed-loop systems as the zero frequency approaches the loop's cross-over frequency. This degradation becomes more critical in systems with weakly damped zeros (characterised by low damping ratios, ζ), where abrupt phase shifts occur near the zero frequency, ω_z . Such phase shifts are particularly problematic when the RHPZ frequencies fall below the controller bandwidth or the loop transfer function's cross-over frequency, exacerbating instability risks and limiting achievable performance. From a control design standpoint, RHPZs are universally undesirable due to their adverse impact on system stability and the fundamental limitations they impose on the achievable closed-loop bandwidth. Therefore, a careful balance between system performance and the trade-offs introduced by RHPZs should be considered, ensuring that controller bandwidth is appropriately tuned to account for these limitations.

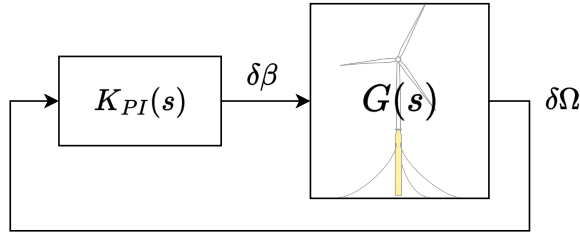


Figure 5.4: Block diagram of the FOWT closed loop system, where $G(s)$ represents the plant model, and $K_{PI}(s)$ represents the collective blade pitch controller.

5.3 Control of floating wind turbines

This section reviews various control strategies proposed for mitigating the negative damping instability in FOWTs, beginning with the most straightforward approaches and progressing toward more complex solutions involving additional sensors and actuators. Each method is evaluated in terms of its ability to address the negative damping effect and its effectiveness in overcoming the bandwidth limitation imposed by the RHPZs. Ultimately, the analysis concludes that only the incorporation of an additional actuator can effectively alleviate the constraint on closed-loop bandwidth—a point that is elaborated further in this section.

Figure 5.4 shows the block diagram of the closed-loop FOWT system with the simple feedback PI controller. Each block represents a linear TF, with $G(s)$ mapping β , the collective blade pitch angle, to Ω , the generator speed, while $K_{PI}(s)$ is the collective blade pitch controller.

Neglecting the floating platform dynamics during the FOWT control design often yields instability in the operating points containing RHPZs. As the high control bandwidth, associated with the high feedback control gains, causes platform pitch excitation [40]. At first, one might expect exponential growth in the response due to negative damping, but this is not the case because of the non-linear dynamic coupling between the different FOWT modes. Yet the FOWT keeps oscillating back and forth without reaching a steady state, which is still undesirable. There are several ways to mitigate this challenging problem. Thus, in the remainder of this section, the conventional solutions are presented, followed by our proposed solution in the next section.

5.3.1 Detuning

A common approach to mitigating negative damping instability is to reduce the bandwidth of the blade pitch controller below the platform's natural frequency [39, 40, 63]. While this stabilises the system, it compromises generator speed tracking performance at operating points where detuning is implemented.

Detuning introduces a control performance trade-off in the vicinity of rated wind speeds. Lowering the closed-loop bandwidth to maintain stability compromises the system's disturbance rejection capability and degrades power tracking performance.

5.3.2 Robust scheduled tuning

As previously mentioned, stability can be maintained in the presence of RHPZs by detuning, such that the natural frequency of the closed-loop is below the frequency of the RHPZs, which is approximately equal to the resonant frequency of the platform pitch [60]. Applying the global detuning approach means that the bandwidth and the damping ratio are constant across all the operating points, which is inefficient since it sacrifices better tracking performance. According to Fig. 5.2 and Fig. 5.3, the limitation set by the RHPZs varies according to the operating point.

Rather than applying a global detuning strategy at all the operating points as described in the previous section, a more efficient approach is to detune the PI controller to the fastest possible response at each operating point separately while maintaining the stability of the linear system [60, 67, 109]. In practice, it is not enough that a system is stable. There must also be some margins of stability that describe how far from instability the linear

system is and its robustness to perturbations. The gain and phase margins are classical robustness measures that have been used for a long time in control system design, but they are not always good robustness indicators when it comes to the Nyquist stability criterion. However, the stability margin s_m can be used instead to give a more general robustness measure. On one hand, it unites both the gain and phase margins under a single parameter, while on the other hand, it ensures that the Nyquist stability criterion is met. The stability margin s_m is also a good robustness measure of nominally stable systems against model uncertainties. The stability margin of a closed-loop system is defined as the shortest distance between the Nyquist curve of the system's loop transfer function, $L(s) = G(s)K(s)$, and the critical point at $s = -1$ in the s -plane, and it expresses how well the Nyquist curve of the loop transfer avoids the critical point. While there is no representation of s_m in the Bode plot of the loop transfer function, s_m is related to the peak magnitude, M_s , of the sensitivity closed-loop transfer function, $S(s) = (1 + L(s))^{-1}$, through $s_m = 1/M_s$, and M_s being the \mathcal{H}_∞ norm of $S(s)$ as [114]:

$$s_m = \frac{1}{M_s} = \frac{1}{\|S(s)\|_\infty} \quad (5.23)$$

System stability robustness is a critical design priority for FOWTs, often leveraged in prior studies to calibrate both SISO [60] and MIMO control architectures [67]. The contour plots in Fig. 5.5 and Fig. 5.6 depict the stability margin and the closed-loop bandwidth evaluated over a range of the Proportional-Integral (PI) control parameters, namely, the natural frequency ω_c , and the damping ratio ζ_c , showcasing the stable design space of the controller parameters, with the white-coloured region determining the unstable region. The stable region becomes larger as wind speed increases and the effect of the RHPZs fades according to Fig. 5.3, which allows for more freedom to increase the controller gains and thus increase the closed-loop bandwidth without destabilising the system. It is important to mention that a stable design space means that the combination of the control parameters means a stable closed-loop system (i.e. not having right-half plane poles). Although the stable design space is extended at higher wind speeds, some combinations of the controller parameters would significantly increase the controller aggressiveness, leading to instability in the non-linear simulations.

Increasing the closed-loop bandwidth reduces the stability margin, pushing the system closer to instability, as shown in Fig. 5.5 and Fig. 5.6. Consequently, achieving robust tuning of the PI controller requires a trade-off between stability robustness and closed-loop bandwidth, as these are competing objectives. Inspired by the work done in [60, 67, 115], an optimisation-based tuning integrating the two key system properties: the stability margin and the closed-loop system bandwidth while considering the actuator limits, is thus employed. The PI controller is parametrised by ω_c and ζ_c collected in the vector $\mathbf{x} \in \mathbb{R}^2$. A scalar objective function $J(\mathbf{x}) : \mathbb{R}^2 \rightarrow \mathbb{R}$ is then constructed with the following requirements: (i) maximise robust stability margin, (ii) maximise closed-loop bandwidth, and (iii) maintain acceptable actuator activity. When formulating $J(\mathbf{x})$, an important aspect is considering the actuator activity to avoid saturation. The control sensitivity function, $K(s)S(s)$, is a good indicator of the actuator activity. Inspired by s_m , the control effort margin s_c is introduced here as a measure of actuation robustness. A low s_c indicates high

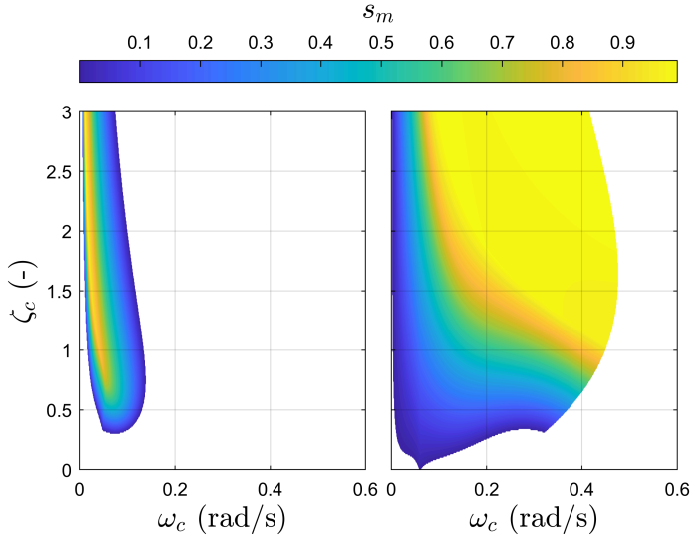


Figure 5.5: Stability margin contours across the natural frequency ω_c and damping ratio ζ_c of the PI controller, shown at two different operating points; near-rated ($\bar{v} = 13$ m/s) and near cut-out ($\bar{v} = 24$ m/s) wind speeds. The white region indicates a destabilising combination of ω_c and ζ_c .

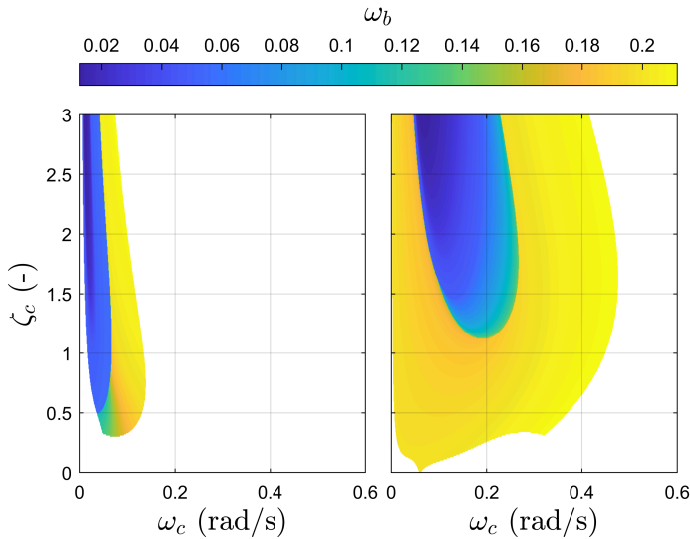


Figure 5.6: Closed-loop bandwidth contours across the natural frequency ω_c and damping ratio ζ_c of the PI controller, shown at two different operating points; near-rated ($\bar{v} = 13$ m/s) and near cut-out ($\bar{v} = 24$ m/s) wind speeds. The white region indicates a destabilising combination of ω_c and ζ_c .

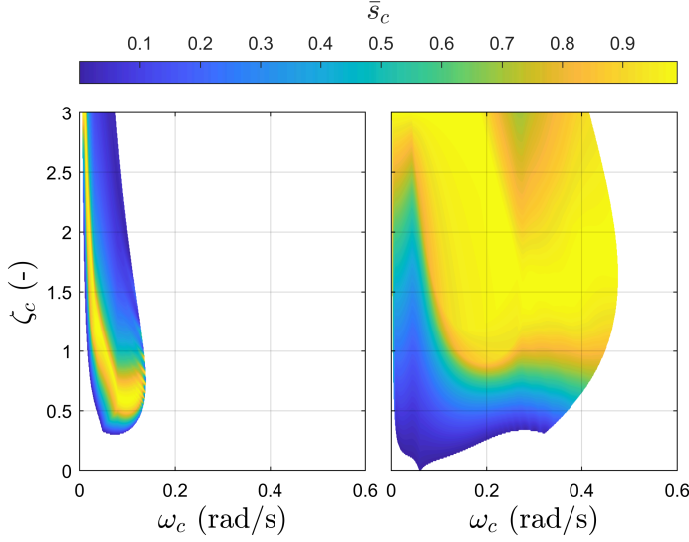


Figure 5.7: Control effort margin contours across the natural frequency ω_c and damping ratio ζ_c of the PI controller, shown at two different operating points; near-rated ($\bar{v} = 13$ m/s) and near cut-out ($\bar{v} = 24$ m/s) wind speeds. The white region indicates a destabilising combination of ω_c and ζ_c .

sensitivity to disturbances, risking actuator saturation. Analogous to s_m , we propose the variable s_c that is related to the peak magnitude of the control sensitivity function M_c through $s_c = 1/M_c$, where M_c is defined as $M_c = \|K(s)S(s)\|_\infty$. The objective function is then formulated as:

$$J(\mathbf{x}) = w_{s_m} s_m(\mathbf{x})^{-1} - w_{b_w} \omega_b(\mathbf{x}) + w_{s_c} s_c(\mathbf{x})^{-1}, \quad (5.24)$$

where w_{s_m} , w_{b_w} , and w_{s_c} are weights adjusting the importance of the stability margin, the bandwidth, and the control effort margin, respectively. Regularisation terms may be added to the objective function to fulfil control objectives such as minimising the generator speed and power oscillations, as well as reducing the loads [60], and limiting the control gains [115]. Despite acknowledging that regularisation terms may be added to limit the gains, the work in [115] does not explicitly integrate actuator limits within their objective function formulation. Neglecting the actuator limits in the objective function would result in controller saturation. Conversely, Eq. (5.24) explicitly incorporates this constraint for the well-posedness of the optimisation problem, ensuring the controller remains within operational limits. The objective function in Eq. (5.24) is then implemented in the optimisation problem in the form:

$$\mathbf{x} = \underset{\mathbf{x}}{\operatorname{argmin}} J(\mathbf{x}) \quad (5.25)$$

In this framework, the optimisation variables (denoted as \mathbf{x}) are the tuning parameters influencing three critical system properties: the stability margin, the closed-loop bandwidth,

and the control effort margin. A systematic tuning method, leveraging the simplified dynamic system, enables rapid recalibration of control settings and assessment of steady-state behaviour. The core objective is to maximise the closed-loop bandwidth while minimising the inverse of the stability margin. Focusing on the inverse of the stability margin ensures the closed-loop stability of the system, while parameters that cause instability are dropped out. After formulating and weighting the objective function, a locally optimal solution is derived using a gradient-based optimisation solver.

Based on Eq. (5.24) and according to Fig. 5.5 and Fig. 5.6, we have two competing objectives, as an increase in the closed-loop bandwidth leads to a reduction in the closed-loop stability margin. Therefore, tuning the PI controller gains to achieve both objectives is not trivial, especially since finding a globally optimal solution is not guaranteed with gradient-based optimisation. Accordingly, a multi-objective optimisation problem is formulated over a set of continuous input variables $\mathcal{X} \subset \mathbb{R}^d$ called the d -dimensional design space [120]. The optimisation goal is to maximise both the stability margin and the closed-loop bandwidth. The optimisation goal is to minimise the vector of the objectives defined as $f(x) = [f_1(x), \dots, f_n(x)]$ with $n \geq 2$, $x \in \mathcal{X}$ being the vector of input variables and $f(\mathcal{X}) \subset \mathbb{R}^n$ the n -dimensional image representing the performance space.

The conflicting nature of the objectives does not always allow for the finding of a single optimal solution to the maximisation problem but a set of optimal solutions as shown in Fig. 5.8, referred to as the Pareto set $\mathcal{P}_s \subseteq \mathcal{X}$ in the design space and the Pareto front $\mathcal{P}_f = f(\mathcal{P}_s) \subset \mathbb{R}^n$ in the performance space [120].

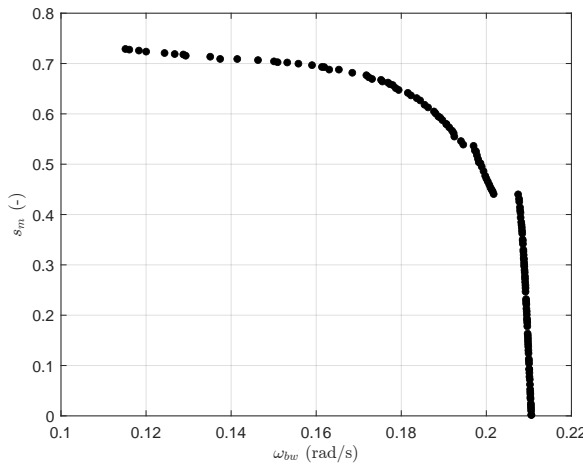


Figure 5.8: The Pareto front resulting from the multi-objective optimisation. Each data point indicates an optimal combination of the PI controller parameters ω_c and ζ_c .

The Pareto front in Fig. 5.8 clearly illustrates the trade-off between closed-loop stability and bandwidth. Beyond a certain threshold, further increasing the bandwidth significantly compromises system stability. The knee point on the Pareto front represents an optimal balance between these competing objectives, making it a favorable region for selection. However, caution is needed when considering solutions in the upper-right region of the

Pareto front. While they offer higher bandwidth, they also lead to excessive pitch activity, rendering them impractical due to actuator constraints.

5.3.3 Multi-loop control

A standard method to address negative damping instability involves implementing a secondary feedback loop that incorporates the platform pitch velocity signal. This technique can utilise blade pitch [63] or generator torque actuation [65], representing a shift toward MIMO control strategies. The approach seeks to reduce the coupling between competing aerodynamic forces—rotor torque and thrust—while maintaining generator speed regulation via blade pitch adjustments. In this work, the platform pitch rate is employed as the fore-aft velocity signal for the secondary feedback loop. The study evaluates both blade pitch damping and generator torque for parallel compensation, finding that combining the two actuators balances their advantages and limitations.

In Eq. (5.14) of the state-space model, the matrix element A_{θ}^{Ω} represents the dynamic coupling between platform pitch velocity, $\dot{\theta}$, and rotor acceleration, $\ddot{\Omega}$. Nullifying this term diminishes the influence of platform pitching on rotor speed tracking. This tuning strategy does not directly suppress platform motion but counteracts its destabilizing effect on speed regulation, thereby enhancing closed-loop stability.

Blade pitch damping: MISO control structure

Compensation using blade pitch feedback, as shown in Fig. 5.9, is achieved by adding an extra term to the element A_{θ}^{Ω} , corresponding to the closure of the inner loop, where the static gain, k_{β} , is scheduled to be consistent with the PI controller gains for each operating point. The blade pitch damping approach uses proportional feedback of the platform pitch velocity [40, 63]:

$$\delta\beta_d = -k_{\beta}\dot{\theta} \quad (5.26)$$

Therefore, the overall blade pitch signal becomes:

$$\delta\beta_t = \delta\beta + \delta\beta_d \quad (5.27)$$

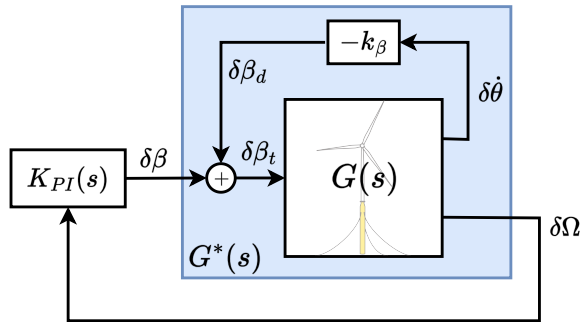


Figure 5.9: Block diagram of the blade pitch damping (MISO controller)

Closing the inner feedback blade pitch loop by substituting $\delta\beta$ from Eq. (5.27) in Eq. (5.3) and Eq. (5.12), the system matrix of the inner loop, A^* , becomes:

$$A^* = \begin{bmatrix} 0 & 1 & 0 \\ -\frac{K}{I_p} & -\frac{1}{I_p} \left(C + l_h^2 \frac{\partial F_a}{\partial v} + l_h k_\beta \frac{\partial F_a}{\partial \beta} \right) & \frac{l_h}{I_p} \frac{\partial F_a}{\partial \Omega} \\ 0 & -l_h \frac{N_{gb}}{J_r} \left(\frac{\partial \tau_a}{\partial v} + k_\beta \frac{\partial \tau_a}{\partial \beta} \right) & \frac{N_{gb}}{J_r} \frac{\partial \tau_a}{\partial \Omega} \end{bmatrix} \quad (5.28)$$

This extra blade pitch in Eq. (5.26) is added to the collective blade pitch command from the PI controller, $K_{PI}(s)$ in Fig. 5.9, before the actuator saturation limits are applied. At first glance, it is observed that the extra feedback loop affects, not only the state transition from the platform pitch velocity to the generator speed, as shown by element $A^*(3,2)$ but also the damping of the platform pitch mode shown by element $A^*(2,2)$. This indicates that this parallel loop can be used for two control objectives: either to compensate for the RHPZs or to increase the platform pitch damping.

Solving for a gain that makes $A^*(3,2) = 0$ leads to full compensation of the effect of platform pitch on the generator speed. However, due to blade pitch coupling with both aerodynamic torque and thrust, such a gain reduces the effective system fore-aft damping as a side effect. It is, therefore, sensible to choose a smaller gain to partially compensate the fore-aft motion, which can be achieved by multiplying the parallel compensation gain by a static gain, ξ_β . The parallel compensation gain for blade pitch then [67, 83]:

$$k_\beta = -\xi_\beta \frac{\partial \tau_a}{\partial v} \left(\frac{\partial \tau_a}{\partial \beta} \right)^{-1} \quad (5.29)$$

The value of $\xi_\beta \in [0, 1]$ determines the degree of partial compensation from the blade pitch actuator to alleviate the effect of the platform pitch motion on the generator speed at the expense of less fore-aft damping. Should the objective of decoupling the drivetrain and the platform dynamics be sought, extra filtering is required to change its dynamics; otherwise, the system damping worsens and it becomes unstable. However, if the control objective shifts to increasing the fore-aft damping, that will be at the expense of reducing the drivetrain damping, thus resulting in less generator speed tracking performance. Similar to Eq. (5.13), the platform pitch dynamics in the second row of A^* is represented in standard form as:

$$\delta \ddot{\theta} + \underbrace{\frac{1}{I_p} \left(C + l_h^2 \frac{\partial F_a}{\partial v} + l_h k_\beta \frac{\partial F_a}{\partial \beta} \right)}_{2\zeta_p^* \omega_p} \delta \dot{\theta} + \underbrace{\frac{K}{I_p}}_{\omega_p^2} \delta \theta = 0, \quad (5.30)$$

where ζ_p^* is the new desired damping ratio of the platform pitch DoF, without any change in its natural frequency. According to Eq. (5.30) and taking Eq. (5.13) into account, k_β can be parametrised as [67]:

$$k_\beta = \frac{2\omega_p \Delta \zeta_p}{l_h \frac{\partial F_a}{\partial \beta}} = \frac{2\omega_p (\zeta_p^* - \zeta_p)}{l_h \frac{\partial F_a}{\partial \beta}}, \quad (5.31)$$

where $\Delta\zeta_p$ represents the desired change in the platform damping. The extra feedback loop acts as a damper, increasing the system damping by moving the poles of $G_{\Omega,\beta}^*$, corresponding to the platform pitch mode, away from their respective zeros. While the RHPZs remain unaffected, setting restrictions on the closed-loop control performance, which is evident from the phase loss of 180° in Fig. 5.10, the damper effect is illustrated, highlighting its direct influence on the outer loop $G_{\Omega,\beta}^*$. It is observed that the rotor dynamics deteriorate by adding the blade pitch damper as the depth of the anti-resonance dip increases, indicating an increase in generator speed oscillations, thereby affecting power production within the frequency range of the fore-aft mode.

Although the MIMO plant, $G(s)$ does not have any transmission zeros, the poor generator speed tracking performance is attributed to the persistence of the RHPZs in $G_{\Omega,\beta}^*$, as they are not affected by the parallel inner loop, and still impose a limitation on the PI controller bandwidth. This is confirmed by checking the numerator of $G_{\Omega,\beta}^*$, whose damping term becomes:

$$C + l_h^2 \underbrace{\left(\frac{\partial F_a}{\partial v} - \frac{\partial \tau_a}{\partial v} \frac{\partial F_a}{\partial \beta} \left(\frac{\partial \tau_a}{\partial \beta} \right)^{-1} \right)}_{\mu_{aero}} - k_\beta l_h \frac{\partial F_a}{\partial \beta} + k_\beta l_h \frac{\partial F_a}{\partial \beta} \quad (5.32)$$

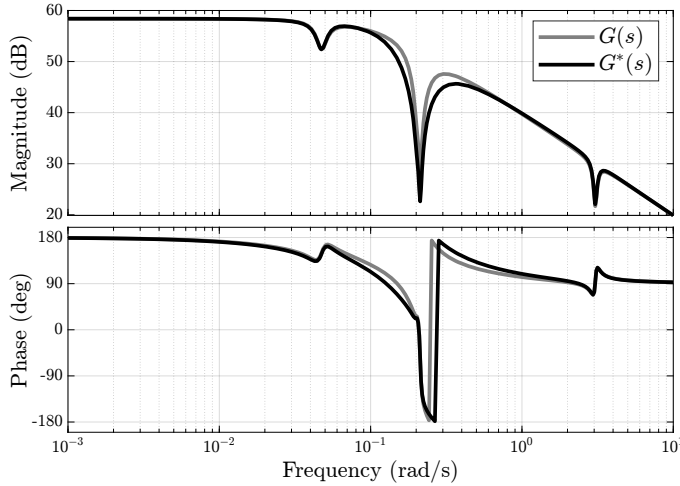


Figure 5.10: Bode plot comparing the channel mapping $\delta\beta$ to $\delta\Omega$ of the original transfer function $G(s)$ with the modified transfer function $G^*(s)$ depicted in Fig. 5.9, obtained after closing the inner loop from platform pitch velocity to blade pitch.

As shown in Eq. (5.32), the RHPZs are indeed unaffected since the inner-loop contribution cancels, thus leaving the RHPZs condition in Eq. (5.18) with no change.

Parallel compensation: MIMO control structure

So far, the previous control strategies proved not to be able to compensate for the deteriorating effect of the RHPZs. The only way to move zeros is by parallel compensation, $y = (G + K)u$, which, if y is a physical output, can only be accomplished by adding an extra input (actuator) [89].

As mentioned earlier, the presence of zeros implies the blockage of certain input signals. In this case, the blade pitch input is blocked due to the emergence of RHPZs, which is depicted in Fig. 5.10 where anti-resonance dips exist, indicating a significant attenuation of the input signals at those frequencies. Therefore, instead of using the blade pitch in the parallel loop, the generator torque can be used as illustrated in Fig. 5.11, thus taking a step towards MIMO control. Unlike the blade pitch, the generator torque compensation is different as when $G_{\Omega, \beta}$, is closed with the generator torque parallel compensation loop, the RHPZs move to the LHP. At optimal gain, the RHPZs vanish from $G_{\Omega, \beta}^*$, which is the TF representing $G_{\Omega, \beta}$ after closing the generator torque parallel loop, indicating that the system became minimum phase. The generator torque parallel compensation uses proportional feedback of the platform pitch velocity [65, 67, 83]:

$$\delta \tau_g = -k_{\tau_g} \delta \dot{\theta} \quad (5.33)$$

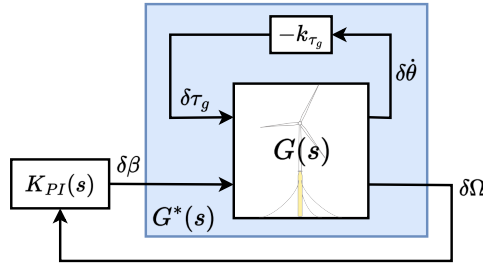


Figure 5.11: Block diagram of the generator torque parallel compensation (MIMO controller)

Closing the inner feedback generator torque loop by substituting $\delta \tau_g$ from Eq. (5.33) in Eq. (5.3) and Eq. (5.12), the system matrix of the inner loop becomes:

$$\mathbf{A}^* = \begin{bmatrix} 0 & 1 & 0 \\ -\frac{K}{I_p} & -\frac{1}{I_p} \left(C + l_h^2 \frac{\partial F_a}{\partial v} \right) & \frac{l_h}{I_p} \frac{\partial F_a}{\partial \Omega} \\ 0 & \frac{N_{gb}}{J_r} \left(k_{\tau_g} N_{gb} - l_h \frac{\partial \tau_a}{\partial v} \right) & \frac{N_{gb}}{J_r} \frac{\partial \tau_a}{\partial \Omega} \end{bmatrix} \quad (5.34)$$

Therefore, to eliminate the effect of platform pitch rate on the rotor dynamics, set $\mathbf{A}^*(3, 2) = 0$. Consequently, the parallel compensation gain for the generator torque actuator is [67, 83]:

$$k_{\tau_g} = \xi_{\tau_g} \frac{l_h}{N_{gb}} \frac{\partial \tau_a}{\partial v}, \quad (5.35)$$

where $\xi_{\tau_g} \in [0, 1]$ is introduced as a tunable parameter determining the intensity of parallel compensation since it is not necessary to remove the RHPZs totally. Having a glance at the numerator of $G_{\Omega, \beta}^*$, it can be noticed that adding the parallel compensation loop modifies the damping term in the numerator by modifying the aerodynamic coefficient, μ_{aero} in Eq. (5.18), to a new one, which in return, leads to a different zeros locations. The new aerodynamic coefficient becomes:

$$\tilde{\mu}_{aero} = \frac{\partial F_a}{\partial v} + (\xi_{\tau_g} - 1) \frac{\partial \tau_a}{\partial v} \frac{\partial F_a}{\partial \beta} \left(\frac{\partial \tau_a}{\partial \beta} \right)^{-1} \quad (5.36)$$

According to Eq. (5.36), the parallel compensation feedback loop makes it possible to manipulate the zeros of $G_{\Omega, \beta}$ and compensate for the RHPZs by pushing them towards the LHP [65, 67, 83, 108]. The level of compensation is tunable based on the tuning of the gain ξ_{τ_g} . The higher ξ_{τ_g} , the more the RHPZs move towards the LHP till they migrate to the LHP indicating the removal of those RHPZs. Consequently, the bandwidth of the PI controller can be increased above the platform pitch mode. This is clear in Fig. 5.12, as the depth of the anti-resonance dip, corresponding to the RHPZs, decreases meaning that the limitation set by the RHPZs is vanishing, which gives the opportunity to increase the aggressiveness of the PI controller.

The main drawback of this approach is the generator torque limit for parallel compensation that can be supplied by the actuator. The usage of the full-compensation gain ($\xi_{\tau_g} = 1$) eliminates the RHPZs, thus, turning the system to minimum phase for all operating points, however, the constraint imposed by the τ_g saturation restrains actuator signals exceeding the maximum generator torque. Reducing the compensation gain with $\xi_{\tau_g} \in [0, 1]$ is rather advantageous in practice, as on one hand, it prohibits the generator torque actuator from saturating, and on the other hand, it reduces the drivetrain loads [83]. With $\xi_{\tau_g} < 1$, the RHPZs are partially compensated, allowing higher achievable bandwidth and, hence, improved performance.

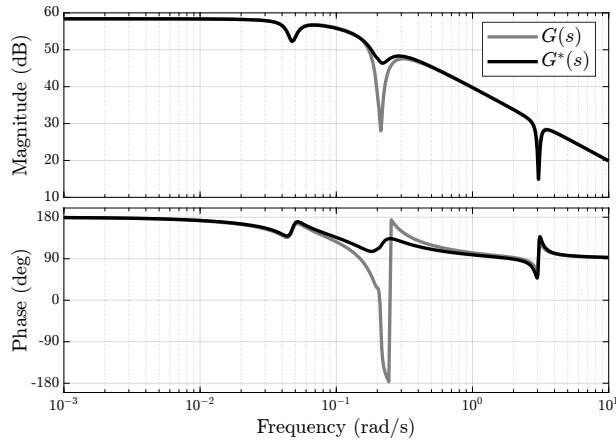


Figure 5.12: Bode plot comparing the original transfer function $G(s)$, which maps $\delta\beta$ to $\delta\Omega$, with the modified transfer function $G^*(s)$ depicted in Fig. 5.11, obtained after closing the parallel compensation feedback inner loop from platform pitch velocity to generator torque.

Parallel compensation: SIMO control structure

It was shown in [83] that the feedback of the platform motion is not necessary for parallel compensation, as only generator speed can be used. They went on to show the control structure of the blade pitch and the generator torque controllers. It was learnt from \mathcal{H}_∞ control synthesis that the blade pitch maintains the PI structure, while the generator torque requires an inverted-notch filter such that it only operates around the RHPZs frequency where the blade pitch input is blocked [83].

Figure 5.13 illustrates the control structure defined in [83], where the blade pitch controller maintains the PI control structure as:

$$K_\beta(s) = k_p + \frac{k_i}{s}, \quad (5.37)$$

where k_p and k_i are the proportional and the integral gains, respectively. As for the generator torque channel, an inverted notch is applied as:

$$K_{\tau_g}(s) = \frac{2\zeta_{\tau_g}\omega_{\tau_g}s}{s^2 + 2\zeta_{\tau_g}\omega_{\tau_g}s + \omega_{\tau_g}^2} \quad (5.38)$$

Consequently, the SIMO controller takes the form:

$$K(s) = \begin{bmatrix} K_{\tau_g}(s) \\ K_\beta(s) \end{bmatrix} \quad (5.39)$$

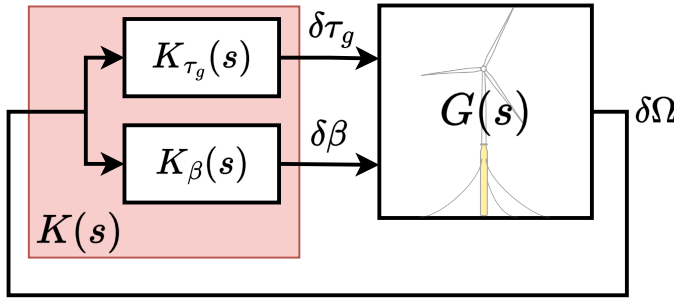


Figure 5.13: Block diagram of the FOWT closed-loop system, where $G(s)$ represents the plant model, and $K(s)$ represents the SIMO structure feedback controller composed of 2 SISO controllers; $K_{\tau_g}(s)$ controller acting on the generator torque actuator, and $K_\beta(s)$ active on the blade pitch actuator.

Now that the need for SIMO control to deal with the negative damping problem has been established in Fig. 5.13, tuning each controller separately sounds complicated due to the dynamic interactions between the MIMO channels that would arise when either of the controllers is modified. Therefore, the objective is to turn the SIMO system into a SISO one. In order to do that, the original MISO plant $G(s)$ is normalised to \bar{G} such that the magnitude of both the blade pitch and the generator torque input channels becomes unity so that both control inputs are of comparable effect. Afterwards, a linear combination of the two control elements \bar{K}_{τ_g} and \bar{K}_β is combined with normalised MISO plant \bar{G} . This is

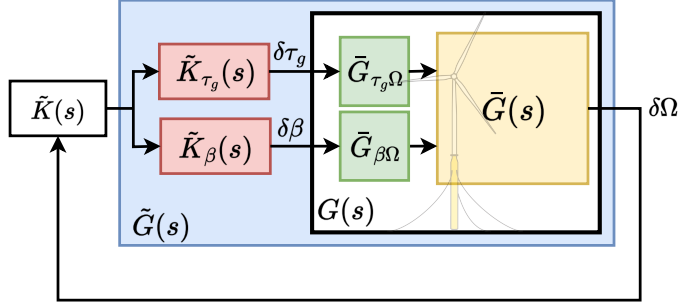


Figure 5.14: Transition from SIMO to SISO control structure

depicted in Fig. 5.14 where the extra blocks are integrated with the plant such that there is a new plant $\tilde{G}(s)$. Therefore, the new SISO plant $\tilde{G}(s)$ is the result of the linear combination of both control channels as:

$$\tilde{G}(s) = \tilde{G}(s) \tilde{K}(s) \begin{bmatrix} 1 \\ 1 \end{bmatrix}, \quad (5.40)$$

where the controllers $K_{\beta}(s)$ and $K_{\tau_g}(s)$ have to be decomposed such that:

$$K(s) = \begin{bmatrix} \tilde{K}_{\tau_g}(s) \\ \tilde{K}_{\beta}(s) \end{bmatrix} \tilde{K}(s) \quad (5.41)$$

where an inverted notch filter is the outcome of combining a high-pass filter and an integrator:

$$K_{\tau_g}(s) = \tilde{K}(s) \tilde{K}_{\tau_g}(s) = \frac{2\zeta_{\tau_g} \omega_{\tau_g} \bar{k}}{s} \times \frac{s^2}{s^2 + 2\zeta_{\tau_g} \omega_{\tau_g} s + \omega_{\tau_g}^2}, \quad (5.42)$$

while a PI controller results from the combination of a PD and an integrator:

$$K_{\beta}(s) = \tilde{K}(s) \tilde{K}_{\beta}(s) = \frac{2\zeta_{\tau_g} \omega_{\tau_g} \bar{k}}{s} \times (\tilde{k}_p + \tilde{k}_d s), \quad (5.43)$$

where the PD controller gains are:

$$\tilde{k}_p = \frac{1}{2\zeta_{\tau_g} \omega_{\tau_g}} \quad (5.44)$$

$$\tilde{k}_d = \frac{1}{(2\zeta_{\tau_g} \omega_{\tau_g})^2} \quad (5.45)$$

The gain \bar{k} in $\tilde{K}(s)$ is a static gain to either crank up or reduce the overall gain of the controllers \tilde{K}_{τ_g} and \tilde{K}_{β} simultaneously. The objective is to tune one single controller instead of multiple control components, which would complicate the control tuning process.

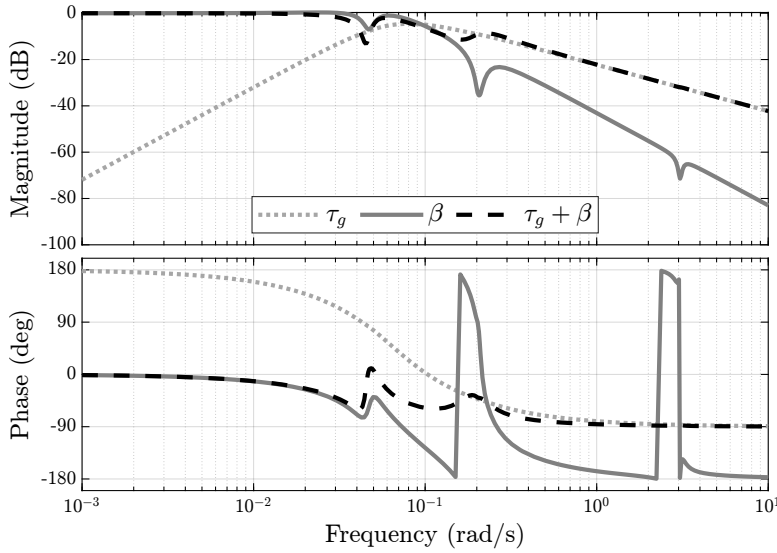


Figure 5.15: Bode plot of the normalised MISO plant \tilde{G} illustrating the frequency response of each control channel separately (solid lines) and the response of the SISO plant \tilde{G} in case of the linear combination of both actuators (dashed line) where the blade pitch actuator is active till a certain frequency before its authority deteriorates and the generator torque actuator takes over from that frequency onwards.

The generator torque actuator is only active within the RHPZs frequency band to take over the control from the blade pitch, which is limited by the non-minimum phase behaviour around that band. This is depicted in Fig. 5.15, where the limitation set on the blade pitch, while regulating the generator speed, is lifted by the generator torque, and the linear combination of both actuators can lead to an increase in the control bandwidth, as shown in Fig. 5.16. The two vertical lines depict the closed-loop bandwidth of each controller. Clearly, the baseline feedback PI controller has its bandwidth constrained by the RHPZs, which are also around the platform pitch natural frequency. Looking at the loop transfer function of the linear combination of both actuators, we can see the jump in the bandwidth the SIMO controller makes over the baseline controller, as the SIMO controller intersects with the 0 dB line much later than the baseline controller. Moreover, the anti-resonance dip that corresponds to the RHPZs existing in the bode plot of the baseline controller is eliminated in the SIMO controller, reflecting on its robustness as it significantly increased with a phase margin of almost 90° .

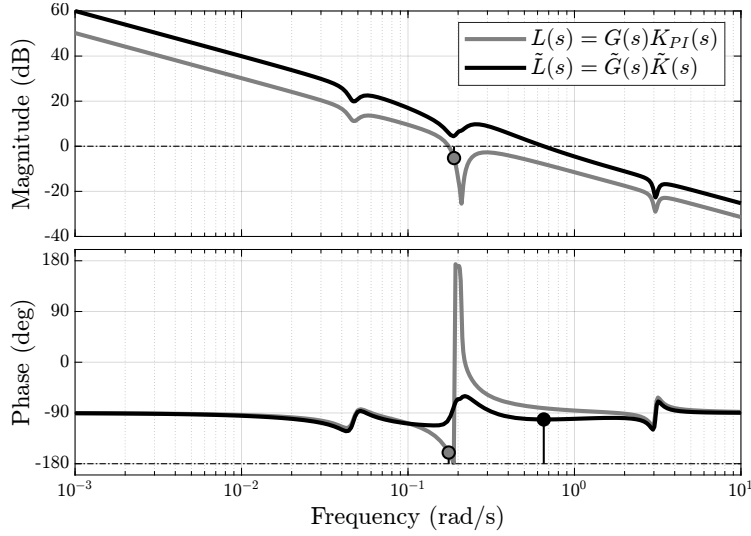


Figure 5.16: Bode plot of the loop transfer function, $L(s)$, of the baseline controller, $K_{PI}(s)$ and the SISO plant, $G(s)$ (grey), and the loop transfer of the artificial SISO plant, $\tilde{G}(s)$, in Fig. 5.14 and $\tilde{K}(s)$ illustrating the effect of the linear combination of both actuators on increasing the bandwidth of the closed-loop system indicated by the vertical lines in the phase plot.

5.4 Results

The FOWT system (NREL 5-MW RWT [17] atop OC3 floater [18]) was simulated in OpenFAST [112] with the five controllers discussed in Section 5.3 in environmental conditions of turbulent wind and irregular waves. The simulations were conducted in the above-rated Region 3 ($v_{rated} = 11.4$ m/s) at average wind speeds ranging from 12 m/s to 24 m/s, with TurbSim [121] to simulate the turbulent wind field, where the International Electrotechnical Commission (IEC) Kaimal spectral model was used as a turbulence model with a turbulence intensity of 14%. The irregular waves were generated using JONSWAP spectrum at a significant wave height $H_s = 3$ m and peak period $T_p = 12$ s. All the simulations were performed for a simulation time of 1200 s, with the first 600 s neglected for transients.

An example time-domain simulation at a reference wind speed of 18 m/s is illustrated in Fig. 5.17 and Fig. 5.18. The time traces are complemented with the power spectra for a detailed view of the controllers' performance. Looking at the rotor speed signal in Fig. 5.17, we can see the significant impact the robust tuning of the SISO PI controller can make in comparison to the detuned SISO PI controller. The rotor speed's peak-to-peak amplitude of the Robust SISO is significantly reduced compared to the detuned SISO. This is also evident in the spectral content of its power spectrum, as the rotor speed oscillations are suppressed till 0.1 Hz.

For the SISO controller, the generator torque is kept constant and the generator power in Region 3 is directly related to the generator speed. The reduction in the rotor speed oscillations reflects on the generator power leading to an improved power quality with less fluctuations. However, such an improved performance comes at the cost of actuation. This is to be expected since the increased bandwidth of the Robust SISO means higher control

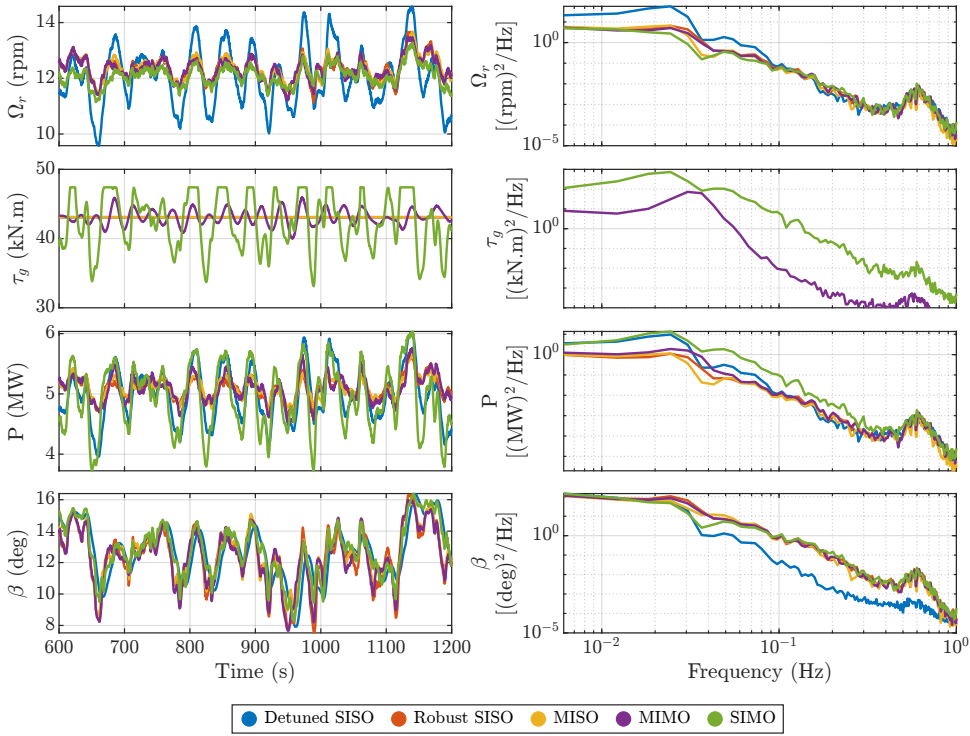


Figure 5.17: Non-linear simulation results for the FOWT system, simulated with each of the controllers described in Section 5.3 at a reference wind speed of 18 m/s.

activity, which can be seen in the blade pitch signal with higher spectral content across the frequency range, leading to an increase in the blade pitch variation.

Regarding the MISO controller in Fig. 5.17, its main objective is to add damping to the closed-loop system, through extra blade pitch action, to compensate for the severe reduction in the overall system damping caused by the negative aerodynamic damping as explained by Eq. (5.18) and Eq. (5.22). In this work, the MISO controller is composed of the Robust SISO controller, and added to it is the inner feedback loop from the platform pitch rate $\dot{\theta}$ to blade pitch as shown in Fig. 5.9. The MISO controller in Fig. 5.17 appears to be doing slightly better than the Robust SISO in a small frequency segment within the low-frequency region before 0.05 Hz, while no significant difference is observed between both controllers at other frequencies. Similar to the detuned and Robust SISO cases, the generator power follows the same trend as the rotor speed since the generator torque is constant in the case of the MISO controller. This explains the absence of the generator torque curves relevant to the three cases in the power spectrum. The MISO controller blade pitch actuation does not change much from the Robust SISO controller. It simply is a bit more active and thus more oscillatory because of the extra blade pitch input added.

As for the MIMO controller in Fig. 5.17, the generator torque is employed as an extra actuator to provide parallel compensation [89] to the FOWT system to deal with the RHPZs.

Implementing the MIMO controller results in a modest enhancement of rotor speed, as the substantial improvement achieved by the Robust SISO controller over the detuned version significantly limits the potential for further error reduction. With the generator torque not constant anymore, the power variation includes contributions from both generator speed and generator torque, showing a clear drawback of the MIMO controller.

Transitioning to the newly proposed control structure, the SIMO controller demonstrates superior performance in generator speed regulation—the primary objective of this controller—particularly when compared to the Detuned SISO controller. While one might expect increased blade pitch activity to achieve better generator speed regulation, this is not the case. Instead, the blade pitch action remains nearly identical to that of the Robust SISO, MISO, and MIMO controllers. This is because, beyond a certain point, generator torque takes over, as previously shown in Fig. 5.15. Consequently, the generator torque response becomes highly aggressive, exhibiting significant variations to maintain a more stable generator speed signal, even reaching saturation. However, this comes at the expense of power quality, similar to the MIMO controller. Notably, the SIMO controller exhibits an even more aggressive generator torque action than the MIMO controller. A less aggressive tuning of the SIMO controller would reduce the actuator usage and improve the power quality. Nevertheless, if the power quality is the main control objective, a controller aimed at that objective could be synthesised, but at the cost of increased drivetrain loads [115].

Across the above-rated wind speed spectrum, the SIMO controller achieves the lowest rotor speed oscillations, as indicated by the standard deviation, without any notable difference in blade pitch action compared to other controllers (see Fig. 5.19). However, the generator torque experiences a large increase with the SIMO controller, even at wind speeds where the RHPZs are expected to disappear (above 16 m/s). This is because, unlike other controllers, the SIMO controller continuously engages the generator torque actuator across all wind speeds, including those without RHPZs. As a result, variations in generator speed have a considerable impact on generator power. In the simulations conducted at reference wind speeds of 12–14 m/s, the system occasionally operates below the rated wind speed, leading to fluctuations in generator torque. This occurs despite the Detuned SISO, Robust SISO, and MIMO controllers being designed to maintain a constant generator torque with zero standard deviation in Region 3—a condition that is fully realised at wind speeds above 14 m/s.

Examining Fig. 5.18 and Fig. 5.19 simultaneously, it is evident that all controllers reduce platform pitch oscillations compared to the fluctuations observed with the Detuned SISO. Among them, the MISO controller achieves the greatest reduction, as it is specifically designed to enhance platform pitch damping—an effect clearly visible in the power spectrum around the platform pitch eigenfrequency (≈ 0.033 Hz) [19].

Although the SIMO controller is primarily designed to mitigate generator speed fluctuations, it also succeeds in reducing platform pitch oscillations below the Detuned SISO level. While its effectiveness in this regard is lower than that of the MISO and MIMO controllers, this reduction remains beneficial.

Furthermore, this improvement extends to the tower base fore-aft moment ($M_{TwrBs,y}$), as there is a strong correlation between platform pitch motion and tower base loading. Consequently, controllers that effectively suppress platform oscillations also contribute to significant tower fatigue reduction.

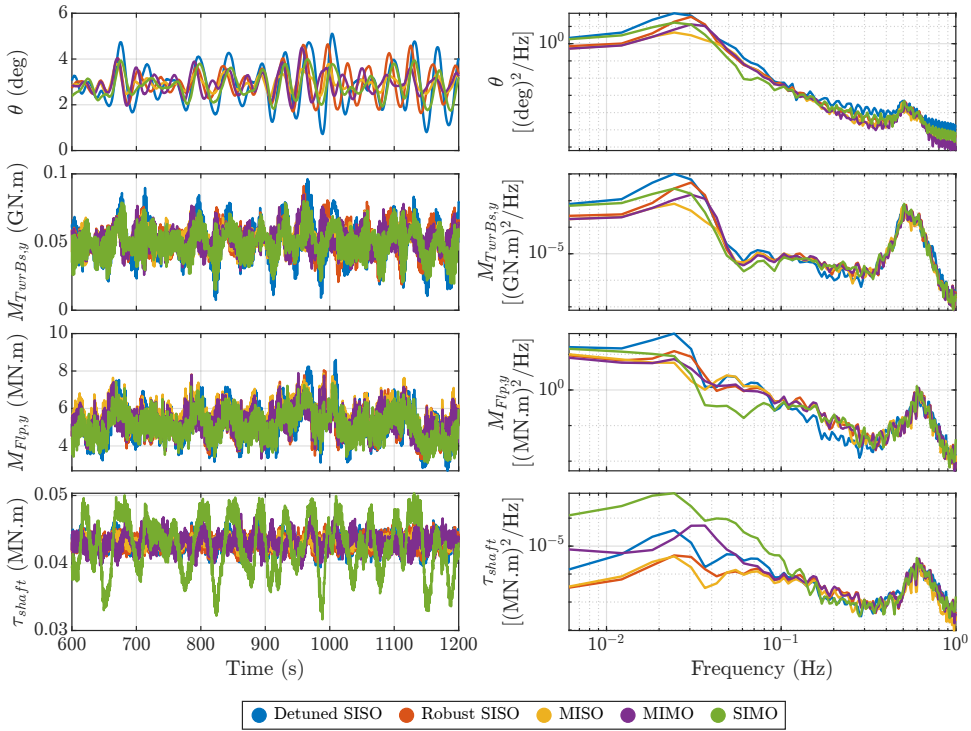


Figure 5.18: Non-linear simulation results for the FOWT system, simulated with each of the controllers described in Section 5.3 at a reference wind speed of 18 m/s.

Regarding the blade-root flapwise moment ($M_{Flp,y}$), all controllers outperform the Detuned SISO across all wind speeds, as shown in Fig. 5.19. This improvement is evident at low frequencies up to 0.1 Hz, after which there is a slight drop in performance, temporarily exceeding the level of the Detuned SISO. Beyond this point, all controllers converge, exhibiting no significant differences, as depicted in Fig. 5.18.

Rotor-shaft torsional loading (τ_{shaft}) is a well-known drawback of torque feedback in wind turbine control systems. While both the Robust SISO and MISO controllers exhibit smaller shaft loading excursions compared to the Detuned SISO, the MIMO and SIMO controllers, which rely on torque feedback, introduce greater fluctuations in shaft torsional loading. As shown in Fig. 5.18, this effect is particularly pronounced in the SIMO controller, which exhibits elevated shaft loading variations across all wind speeds, as further illustrated in Fig. 5.19.

Based on these findings, the authors recommend an adaptive approach, where different proposed controllers are alternated depending on environmental conditions and control objectives. For example, at certain times, the turbine operator may prioritise minimising generator speed oscillations and activate the corresponding controller. At other times, the focus may shift to reducing structural loading, necessitating a different control strategy. Since no single controller can simultaneously optimise all objectives—some of which may

be conflicting—dynamic selection based on operational priorities is advised.

Another recommendation is to incorporate a feedforward control strategy to reduce dependence on reactive feedback control. If an accurate preview of disturbances affecting the FOWT is available, a LiDAR feedforward controller [54] targeting the wind turbulence and a wave feedforward controller [95, 122] targeting the wave forces can be implemented to mitigate the effects of wind and wave disturbances on the FOWT, respectively. This approach alleviates the need for a high-bandwidth feedback controller, as the feedforward controllers would handle most of the disturbance rejection.

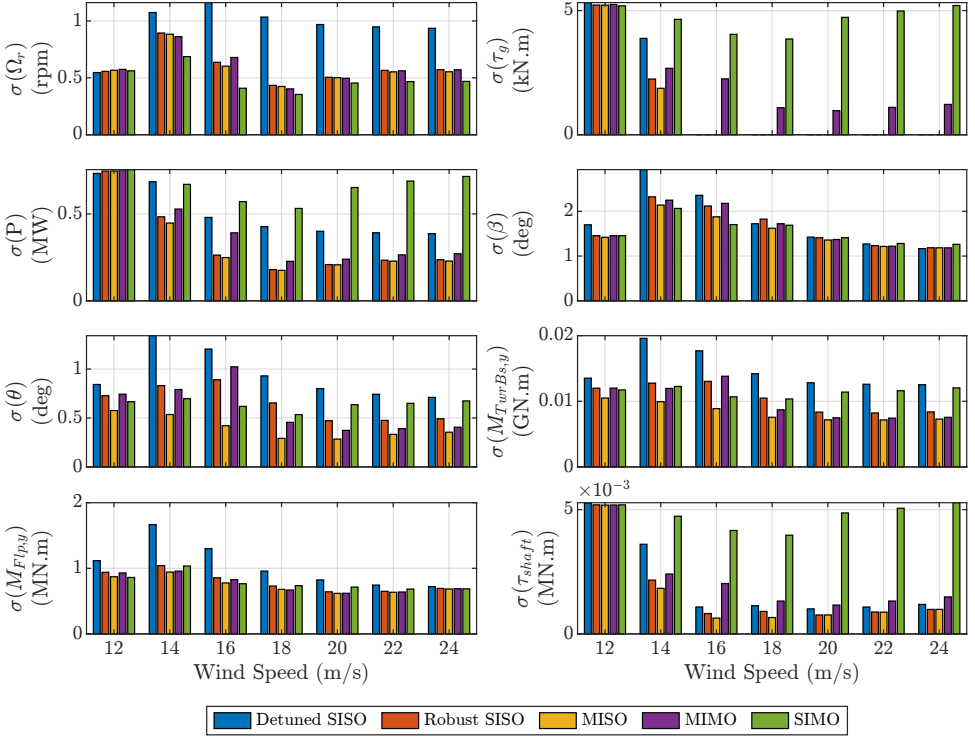


Figure 5.19: Controller performance: Non-linear simulation results for the FOWT, simulated with each of the controllers described in Section 5.3 at a reference wind speed of 18 m/s.

5.5 Conclusion

A new fixed-structure controller has been developed for FOWTs to effectively mitigate the well-known "negative damping" instability and address the non-minimum phase behaviour introduced by the persistent RHPZs in $G_{\Omega,\beta}$. Designed specifically for generator speed regulation, the proposed controller was evaluated through non-linear simulations in OpenFAST, where it outperformed the existing FOWT controllers from the literature. Furthermore, it demonstrated robustness in a high-fidelity simulation environment, effectively handling additional system dynamics.

The primary advantage of the proposed FOWT controller is that it operates without requiring any additional sensors, preserving the conventional SISO configuration by relying exclusively on generator speed measurement. This approach enhances robustness, as incorporating extra signals can increase sensitivity to unmodeled dynamics. Additionally, the controller can be regarded as an artificial SISO controller, as shown in Fig. 5.14 and Fig. 5.15, where the plant transfer function is pre-filtered to achieve the desired control performance.

While the MIMO controller features a simpler control structure compared to the SIMO controller, the SIMO configuration provides built-in redundancy within the FOWT system, ensuring continued operation in the event of floating platform sensor failure. If the wind turbine is equipped with platform pitch sensors and the MIMO controller is in use, a sensor malfunction could compromise performance. In such a scenario, the SIMO controller acts as a backup solution, allowing the system to operate despite the loss of platform pitch measurements.

Incorporating inner loops into the standard control loop $G_{\Omega,\beta}$, whether using MISO, SIMO, or MIMO structures, expands the design space for the SISO PI feedback controller, enabling the achievement of higher bandwidth. However, a well-known drawback of employing generator torque actuation for parallel compensation is the resulting increase in shaft and drivetrain loads [65], along with deteriorated power quality. To mitigate power quality concerns, alternative MIMO feedback architectures, such as a constant-power controller [115], can be integrated.

Furthermore, the cost function in the robust control tuning approach from [115] has been modified to prevent actuator saturation. Without this adjustment, actuator activity could become unbounded, leading to simulation instability. This refinement has enhanced performance in the primary objectives of generator speed regulation and tower load reduction, even in the presence of modelling inaccuracies resulting from dynamic simplifications and omitted degrees of freedom.

6

Conclusions and Recommendations

Conclusions

Floating offshore wind represents a pivotal means for accessing wind resources in deep-water locations, where conventional bottom-fixed solutions are infeasible. Realising its full potential and accelerating its commercial viability requires innovation, particularly in control system design, to drive down costs and enhance operational performance. This thesis is dedicated to advancing the state-of-the-art in control technology for floating wind turbines. The primary research objective, as introduced in Chapter 1, was:

The development of wave feedforward and multivariable feedback control architectures and design methods for floating wind turbines

To fulfil the overarching objective, this thesis tackled two principal control challenges associated with floating wind turbines: the disturbance introduced by wave excitation forces and the bandwidth limitation imposed by the negative damping instability affecting the collective blade pitch feedback controller.

With regard to wave feedforward control, a key question arises: How beneficial is this technology, and is it viable for industrial adoption? The findings indicate that wave feedforward control is effective in mitigating the adverse effects of wave-induced disturbances on floating wind turbines. While it demonstrates greater potential for improving power regulation than for structural load reduction, its adoption in practice may not be economically justifiable. This is due to the trade-off between the control performance gains and the increased actuator activity, as well as the additional costs associated with the installation and maintenance of wave radar systems. Moreover, since wind turbulence typically exerts a more dominant influence on turbine performance than wave excitation, prioritising wind disturbance mitigation may offer a greater overall benefit.

Regarding multivariable feedback control for floating wind turbines, introducing a new control structure to the existing portfolio can enhance turbine operability—particularly when the architecture leverages existing control variables without necessitating additional sensor instrumentation or incurring extra costs. While the proposed control strategy offers distinct advantages, it also presents certain trade-offs, as is the case with all control

solutions reported in the literature. Ultimately, the decision to adopt such an architecture lies with the wind turbine operators, and its practical value will be determined by the industry's assessment of its performance and applicability.

In summary, the implementation of any proposed control technology cannot be universally applied across all operating scenarios. The choice of the most appropriate control strategy depends on the specific operational conditions and the control objectives defined by the turbine operator—whether the focus is on load mitigation, power regulation, or other performance targets. The incorporation of feedforward control, in particular, is contingent on the availability of reliable disturbance preview and the extent to which it proves beneficial under a given set of conditions. In practice, these control strategies should be viewed as complementary tools in the operator's control arsenal, to be selectively deployed based on situational needs and economic feasibility. More detailed conclusions are presented in the remainder of this section.

Chapter 2 presented a wave feedforward control framework for floating wind turbines, aiming to reduce wave-induced disturbances. Two H_∞ -based controllers were designed: one to regulate generator speed and another to reduce platform pitch motion. Linear models identified using the Predictor-Based Subspace Identification (PBSIDopt) algorithm were embedded in a generalised plant, and the resulting high-order controllers were reduced to fixed, low-order structures for practical implementation.

Designed for the DTU 10 MW turbine on the SOFTWIND spar platform, the controllers were evaluated in mid-fidelity nonlinear simulations using QBlade. Results showed improved power quality and reduced blade loading. Notably, the feedforward control complements the industry-standard feedback controller without requiring structural changes, relying on wave preview enabled by mature marine sensing technologies.

Advancing the technology readiness level to support industrial deployment, Chapter 3 presented successful wave tank experiments validating the wave feedforward control strategy developed in Chapter 2, using wave excitation force previews. The wave feedforward control was effective in reducing the impact of wave-induced disturbances on the generator power output of floating wind turbines. However, when targeting platform pitch motion reduction, considerable actuator effort was required, highlighting a trade-off between control performance and actuation requirements.

The experimental campaign also evaluated controller robustness under varying wind turbulence levels, wave heights, and directional spreading. While the wave feedforward strategy proved effective overall, high turbulence diminished its benefit as the response was dominated by wind turbulence. Consequently, it is concluded that wave feedforward control offers tangible improvements in power quality but is less practical for pitch mitigation due to high actuator effort.

Following the exploration of the potential benefits of wave feedforward control, attention was redirected toward feedback control in the above-rated wind speed region—an operating regime where negative damping instability becomes prominent. This prompted the investigation of whether alternative control structures, beyond those proposed in the literature, could effectively mitigate this issue. To address this, Chapter 4 introduced a generalised framework for the H_∞ synthesis of a Single-Input, Multiple-Output (SIMO) feedback controller aimed at rotor speed regulation in floating wind turbines. The control synthesis explicitly incorporated the objective of mitigating rotor speed oscillations. The

resulting \mathcal{H}_∞ SIMO controller was then simplified into a fixed-structure form compatible with industry-standard control practices. This reduced-order controller comprises essential components such as an inverted notch filter and a proportional-integral (PI) controller. However, when employing sequential loop closure for this structure, careful attention must be given to the order of loop implementation, as incorrect sequencing can compromise system stability.

In Chapter 5, a new fixed-structure controller has been developed for floating offshore wind turbines to mitigate negative damping instability and address the non-minimum phase behaviour caused by right-half-plane zeros in the transfer function from the blade pitch to the generator speed. Designed for generator speed regulation, the controller demonstrated superior performance and proved robust in non-linear OpenFAST simulations. The controller retains a traditional SISO architecture, relying solely on generator speed measurements, thus avoiding additional sensor complexity and minimising sensitivity to unmodelled dynamics. It functions as an artificial SISO controller via pre-filtering of the plant. While the MIMO layout offers simplicity, the SIMO controller introduces redundancy, maintaining functionality during sensor failures. Integrating inner feedback loops broadens the PI controller's bandwidth capabilities. However, generator torque-based compensation may elevate drivetrain loads and degrade power quality. Finally, the robust tuning approach was improved by constraining actuator usage within the cost function, preventing instability from excessive control effort. This adjustment enhanced generator speed regulation and tower load reduction despite model simplifications and unmodelled dynamics.

Recommendations

This thesis has presented the work undertaken to mitigate wave-induced disturbances in floating wind turbines, along with the development of a novel approach to address negative damping instability. Nonetheless, there is potential for further enhancement, and to support future research, the following recommendations are proposed:

- A wide range of control strategies have been developed in the literature, each targeting specific, often competing, objectives such as load mitigation, power regulation, platform stabilisation, or wake interaction. As a result, no single controller is currently capable of satisfying all control objectives simultaneously under varying operating conditions. To address this limitation, future work could focus on the development of a high-level supervisory control framework. Such a supervisory controller would dynamically manage a suite of specialised controllers, selecting and activating the most appropriate one based on the prevailing operational state of the turbine or wind farm. This hierarchical control approach has the potential to enhance overall system performance by ensuring that the control strategy adapts in real time to the turbine's operating conditions, environmental inputs, and performance priorities.
- A comprehensive evaluation of the cost-effectiveness of the wave feedforward control strategy is warranted, particularly due to its reliance on an additional wave radar sensor and the associated costs related to hardware, installation, and maintenance.

This assessment should determine whether the achieved performance gains, such as improved load mitigation and power quality, justify the additional investment and whether the approach leads to a net reduction in total system or lifecycle costs. Furthermore, a comparative analysis with the baseline control scheme is necessary to establish the economic viability of adopting this technology in real-world applications.

- An interesting continuation of this work would be to explore the combined implementation of LiDAR and wave feedforward control strategies. Alternatively, a comparative analysis evaluating the effectiveness of each strategy individually—relative to the baseline controller—would provide valuable insights. Such an investigation could help determine the conditions under which it is most beneficial to adopt either or both approaches, thereby supporting more informed decisions regarding their practical deployment in floating wind turbine systems.
- The X-band radar has been identified as a suitable sensing technology for wave measurement. However, the control design has been developed under the assumption of perfect wave information. A natural extension of this work would be to incorporate the effects of measurement uncertainty associated with the radar system. Evaluating how such inaccuracies influence controller performance is essential for assessing the robustness of the proposed strategy. Moreover, integrating measurement uncertainty directly into the control synthesis process represents an important step toward developing more resilient and practically deployable control solutions.
- The wave feedforward controller developed in this work is based on a linear framework and focuses solely on compensating first-order wave excitation forces. However, recent numerical and experimental studies have demonstrated that second-order wave loads can have a significant impact on the dynamic response of floating wind turbines. Consequently, a valuable direction for future research would be the development of advanced control strategies that explicitly account for second-order hydrodynamic effects in the controller design process.
- Despite significant advances in control theory, Single-Input Single-Output (SISO) controllers remain the industry standard for both fixed-bottom and floating wind turbines. While advanced Multi-Input Multi-Output (MIMO) control strategies offer the potential for improved system performance by simultaneously addressing multiple coupled dynamics—such as platform motion, blade pitch, and generator torque—their adoption in commercial wind turbine systems remains limited. This is partly due to the increased complexity in implementation, tuning, and validation, as well as a lack of transparency, as industry players typically do not disclose the structure or logic of their proprietary control systems. Future research should investigate the practical deployment of MIMO controllers and assess their performance benefits under realistic operating conditions. Strengthening collaboration between academia and industry could facilitate this transition and encourage the move toward more advanced, robust, and integrated control strategies. Ultimately, pushing industrial control design beyond the current SISO paradigm will be essential for optimising the performance and reliability of next-generation floating wind turbines.

- Control co-design for floating wind turbines represents a promising direction for future research, as it enables the simultaneous consideration of aerodynamic, hydrodynamic, structural, and control objectives during the design process. However, implementing such an approach is non-trivial, particularly due to the potential divergence in optimisation goals between individual turbines and entire wind farms. For example, while minimising platform motion may be a primary objective at the single-turbine level, allowing controlled motion in a wind farm context could be beneficial for enhancing wake mixing and, consequently, improving overall power capture. Addressing these conflicting objectives within a unified co-design framework remains a significant challenge and an important area for further investigation.
- Wave tank and wind tunnel hybrid experiments offer complementary insights into the behaviour of floating wind turbines. However, it remains unclear whether one of these approaches yields superior value for specific research objectives or whether they can be considered interchangeable depending on the context. Furthermore, in cases where both experimental setups are utilised, there is currently no standardised framework for systematically integrating or comparing their results. Developing such a framework would enhance the consistency, interpretability, and applicability of experimental findings across different testing environments.

Bibliography

References

- [1] United Nations Framework Convention on Climate Change (UNFCCC). The Paris Agreement, 2015. Accessed March 25, 2025. <https://unfccc.int/process-and-meetings/the-paris-agreement>.
- [2] Climate change 2023: Synthesis reports. Technical report, Intergovernmental Panel on Climate Change (IPCC), 2023. doi:10.59327/IPCC/AR6-9789291691647.
- [3] ETIPWind Executive Committee, Alexander Vandenberghe, and Pierre Tardieu. ETIPWind: Road map. Technical report, European Technology and Innovation Platform on Wind Energy (ETIPWind), 2020. Accessed March 22, 2025. <https://etipwind.eu/roadmap/>.
- [4] Wind energy in europe 2024: Statistics and the outlook for 2025-2030. Technical report, WindEurope, 2025. Accessed March 22, 2025. <https://windeurope.org/intelligence-platform/product/wind-energy-in-europe-2024-statistics-and-the-outlook-for-2025-2030/>.
- [5] European Commission. EU wind energy. Accessed February 05, 2023. https://research-and-innovation.ec.europa.eu/research-area/energy/wind-energy_en.
- [6] European Environment Agency. Trends and projections in europe 2024. Technical report, 2024. doi:10.2800/7574066.
- [7] M. Dolores Esteban, J. Javier Diez, Jose S. López, and Vicente Negro. Why offshore wind energy? *Renewable Energy*, 36(2):444–450, 2011. doi:<https://doi.org/10.1016/j.renene.2010.07.009>.
- [8] ETIPWind: Offshore renewables paving the way for a competitive and climate-neutral europe by 2050. Technical report, European Technology and Innovation Platform on Wind Energy (ETIPWind), 2024. Accessed March 25, 2025. <https://etipwind.eu/wp-content/uploads/files/publications/20241025-Etipwind-etip-ocean-joint-study.pdf>.
- [9] J.K. Kaldellis and D. Apostolou. Life cycle energy and carbon footprint of offshore wind energy. comparison with onshore counterpart. *Renewable Energy*, 108:72–84, 2017. doi:<https://doi.org/10.1016/j.renene.2017.02.039>.
- [10] Yun-Jae Kim, Jin Seok Lim, Hae Jong Kim, and Sung-Woong Choi. A comprehensive review of foundation designs for fixed offshore wind turbines. *International Journal of Naval Architecture and Ocean Engineering*, 17:100643, 2025. doi:<https://doi.org/10.1016/j.ijnaoe.2025.100643>.

- [11] Jason M. Jonkman. Dynamics of offshore floating wind turbines—model development and verification. *Wind Energy: An International Journal for Progress and Applications in Wind Power Conversion Technology*, 12(5):459–492, 2009. doi:10.1002/we.347.
- [12] Isaac Van der Hoven. Power spectrum of horizontal wind speed in the frequency range from 0.0007 to 900 cycles per hour. *Journal of Atmospheric Sciences*, 14(2):160 – 164, 1957. doi:10.1175/1520-0469(1957)014<0160:PSOHW>2.0.CO;2.
- [13] Blair Kinsman. *Wind waves: their generation and propagation on the ocean surface*. Courier Corporation, 1984.
- [14] Tony Burton, Nick Jenkins, David Sharpe, and Ervin Bossanyi. *Wind Energy Handbook*. John Wiley Sons, Ltd, 2011. doi:<https://doi.org/10.1002/9781119992714.ch8>.
- [15] J.C. Kaimal, J.C. Wyngaard, Y. Izumi, and O.R. Coté. Spectral characteristics of surface-layer turbulence. *Quarterly Journal of the Royal Meteorological Society*, 98(417):563–589, 1972. doi:<https://doi.org/10.1002/qj.49709841707>.
- [16] Johan M.J. Journée and William W. Massie. Offshore hydromechanics. 2000.
- [17] J. Jonkman, S. Butterfield, W. Musial, and G. Scott. Definition of a 5-MW reference wind turbine for offshore system development, 2009. doi:10.2172/947422.
- [18] Jason Jonkman. Definition of the Floating System for Phase IV of OC3. Technical report, National Renewable Energy Laboratory, 2010. doi:10.2172/979456.
- [19] G.K.V. Ramachandran, A. Robertson, J.M. Jonkman, and M.D. Masciola. Investigation of response amplitude operators for floating offshore wind turbines. In *Proceedings of the 23rd International Offshore and Polar Engineering Conference*, pages ISOPE–I–13–106, June 2013.
- [20] M. Atcheson, A. Garrad, L. Cradden, A. Henderson, D. Matha, J. Nichols, D. Roddier, and J. Sandberg. Floating offshore wind energy. *Springer*, 10(1007):978–3, 2016. doi:10.1007/978-3-319-29398-1.
- [21] WindEurope. Unleashing Europe’s offshore wind potential: A new resource assessment, 2017. Accessed April 08, 2025. <https://windeurope.org/wp-content/uploads/files/about-wind/reports/Unleashing-Europes-offshore-wind-potential.pdf>.
- [22] DNV. Energy transition outlook 2024: A global and regional forecast to 2050. Technical report, Det Norske Veritas (DNV), 2024. Accessed March 25, 2025. <https://www.dnv.com/energy-transition-outlook/>.
- [23] A.D. Wright. *Modern Control Design for Flexible Wind Turbines*. July 2004. doi:10.2172/15011696.
- [24] A.D. Wright and L.J. Fingersh. Advanced control design for wind turbines; part i: Control design, implementation, and initial tests. Technical report, National Renewable Energy Laboratory (NREL), Golden, CO., Feb 2008. doi:10.2172/927269.

- [25] Fernando D Bianchi, Hernán De Battista, and Ricardo J Mantz. *Wind Turbine Control Systems*. 2010. doi:10.1115/1.802601.ch14.
- [26] Unai Gutierrez Santiago. *Measuring dynamic mechanical torque with fiber-optic sensors for geared wind turbines*. PhD thesis, Delft University of Technology, 2025. doi:10.4233/uuid:67ec64b8-c69e-4140-9019-cb33376f3622.
- [27] Paul A. Fleming, Pieter M.O. Gebraad, Sang Lee, Jan-Willem van Wingerden, Kathryn Johnson, Matt Churchfield, John Michalakes, Philippe Spalart, and Patrick Moriarty. Evaluating techniques for redirecting turbine wakes using SOWFA. *Renewable Energy*, 70:211–218, 2014. Special issue on aerodynamics of offshore wind energy systems and wakes. doi:https://doi.org/10.1016/j.renene.2014.02.015.
- [28] D. van der Hoek, J. Frederik, M. Huang, F. Scarano, C. Simao Ferreira, and J.W. van Wingerden. Experimental analysis of the effect of dynamic induction control on a wind turbine wake. *Wind Energy Science*, 7(3):1305–1320, 2022. doi:10.5194/wes-7-1305-2022.
- [29] Daniel van den Berg, Delphine de Tavernier, David Marten, Joseph Saverin, and Jan-Willem van Wingerden. Wake mixing control for floating wind farms: Analysis of the implementation of the helix wake mixing strategy on the iea 15-mw floating wind turbine. *IEEE Control Systems*, 44(5):81–105, 2024. doi:10.1109/MCS.2024.3432341.
- [30] E.A. Bossanyi. The design of closed loop controllers for wind turbines. 3(3):149–163. doi:10.1002/we.34.
- [31] E.A. Bossanyi. Wind turbine control for load reduction. 6(3):229–244. doi:10.1002/we.95.
- [32] L. Brandetti, S.P. Mulders, R. Merino-Martinez, S. Watson, and J.W. van Wingerden. Multi-objective calibration of vertical-axis wind turbine controllers: balancing aero-servo-elastic performance and noise. *Wind Energy Science*, 9(2):471–493, 2024. doi:10.5194/wes-9-471-2024.
- [33] Lucy Y. Pao and Kathryn E. Johnson. A tutorial on the dynamics and control of wind turbines and wind farms. In *2009 American Control Conference*, pages 2076–2089, 2009. doi:10.1109/ACC.2009.5160195.
- [34] Lucy Y. Pao and Kathryn E. Johnson. Control of wind turbines. *IEEE Control Systems Magazine*, 31(2):44–62, 2011. doi:10.1109/MCS.2010.939962.
- [35] Nikhar J. Abbas, Daniel S. Zalkind, Lucy Pao, and Alan Wright. A reference open-source controller for fixed and floating offshore wind turbines. 7(3):53–73, 2022. doi:10.5194/wes-7-53-2022.
- [36] Albert Betz. Das maximum der theoretisch möglichen ausnützung des windes durch windmotoren. *Zeitschrift für das gesamte Turbinenwesen*, 1920.

- [37] James F Manwell, Jon G McGowan, and Anthony L Rogers. *Wind energy explained: theory, design and application*. John Wiley Sons, Ltd, 2009. doi:<https://doi.org/10.1002/9781119994367.ch3>.
- [38] L. Brandetti, Y. Liu, S.P. Mulders, C. Ferreira, S. Watson, and J.W. van Wingerden. On the ill-conditioning of the combined wind speed estimator and tip-speed ratio tracking control scheme. *Journal of Physics: Conference Series*, 2265(3):032085, may 2022. doi:10.1088/1742-6596/2265/3/032085.
- [39] T J Larsen and T D Hanson. A method to avoid negative damped low frequent tower vibrations for a floating, pitch controlled wind turbine. 75:012073, 2007. doi:10.1088/1742-6596/75/1/012073.
- [40] Jason Jonkman. Influence of control on the pitch damping of a floating wind turbine. In *46th AIAA Aerospace Sciences Meeting and Exhibit*. American Institute of Aeronautics and Astronautics, 2008. doi:10.2514/6.2008-1306.
- [41] Morten Hartvig Hansen and Lars Christian Henriksen. *Basic DTU Wind Energy controller*. Number 0028. DTU Wind Energy, Denmark, 2013.
- [42] S.P. Mulders and J.W. van Wingerden. Delft research controller: an open-source and community-driven wind turbine baseline controller. *Journal of Physics: Conference Series*, 1037(3):032009, June 2018. doi:10.1088/1742-6596/1037/3/032009.
- [43] E.L. Van der Hooft, P. Schaak, and T.G. Van Engelen. Wind turbine control algorithms. *DOWEC project-DOWEC-F1W1-EH-03-094/0, Task-3 report*, 2003.
- [44] Zili Zhang, Søren R. K. Nielsen, Frede Blaabjerg, and Dao Zhou. Dynamics and control of lateral tower vibrations in offshore wind turbines by means of active generator torque. *Energies*, 7(11):7746–7772, 2014. doi:10.3390/en7117746.
- [45] Karl A. Stol, Wenxin Zhao, and Alan D. Wright. Individual blade pitch control for the controls advanced research turbine (CART). *Journal of Solar Energy Engineering*, 128(4):498–505, 07 2006. doi:10.1115/1.2349542.
- [46] Daniel Duckwitz and Martin Geyler. Active damping of the side-to-side oscillation of the tower. In *Proceedings of DEWEK*, 2010.
- [47] A.K. Scholbrock, P.A. Fleming, L.J. Fingersh, A.D. Wright, D. Schlipf, F. Haizmann, and F. Belen. Field testing lidar based feed-forward controls on the nrel controls advanced research turbine: Preprint. National Renewable Energy Laboratory (NREL), Golden, CO., 2012. doi:10.2514/6.2013-818.
- [48] David Schlipf, Dominik Johannes Schlipf, and Martin Kühn. Nonlinear model predictive control of wind turbines using lidar. *Wind Energy*, 16(7):1107–1129, 2013. doi:<https://doi.org/10.1002/we.1533>.
- [49] Andrew Scholbrock, Paul Fleming, David Schlipf, Alan Wright, Kathryn Johnson, and Na Wang. Lidar-enhanced wind turbine control: Past, present, and future. In *2016 American Control Conference (ACC)*, pages 1399–1406, 2016. doi:10.1109/ACC.2016.7525113.

- [50] Hazim Namik, Karl Stol, and Jason Jonkman. State-space control of tower motion for deepwater floating offshore wind turbines. In *46th AIAA Aerospace Sciences Meeting and Exhibit*. American Institute of Aeronautics and Astronautics. doi:10.2514/6.2008-1307.
- [51] Yu Ma, Paul D. Scavounos, John Cross-Whiter, and Dhiraj Arora. Wave forecast and its application to the optimal control of offshore floating wind turbine for load mitigation. *Renewable Energy*, 128:163–176, 2018. doi:https://doi.org/10.1016/j.renene.2018.05.059.
- [52] David Schlipf, Paul Fleming, Florian Haizmann, Andrew Scholbrock, Martin Hofsäß, Alan Wright, and Po Wen Cheng. Field testing of feedforward collective pitch control on the cart2 using a nacelle-based lidar scanner. *Journal of Physics: Conference Series*, 555(1):012090, dec 2014. doi:10.1088/1742-6596/555/1/012090.
- [53] S.T. Navalkar, J.W. van Wingerden, P.A. Fleming, and G.A.M. van Kuik. Integrating robust lidar-based feedforward with feedback control to enhance speed regulation of floating wind turbines. In *2015 American Control Conference (ACC)*, pages 3070–3075, 2015. doi:10.1109/ACC.2015.7171804.
- [54] David Schlipf, Frank Lemmer, and Steffen Raach. Multi-variable feedforward control for floating wind turbines using lidar. volume The 30th International Ocean and Polar Engineering Conference of *International Ocean and Polar Engineering Conference*, pages ISOPE–I–20–1174, 10 2020.
- [55] Steffen Raach, David Schlipf, Frank Sandner, Denis Matha, and Po Wen Cheng. Nonlinear model predictive control of floating wind turbines with individual pitch control. In *2014 American Control Conference*, pages 4434–4439, 2014. doi:10.1109/ACC.2014.6858718.
- [56] David Schlipf, Eric Simley, Frank Lemmer, Lucy Pao, and Po Wen Cheng. Collective pitch feedforward control of floating wind turbines using lidar. In *ISOPE International Ocean and Polar Engineering Conference*. ISOPE, 2015. doi:10.17736/jowe.2015.arr04.
- [57] Frank Lemmer, Steffen Raach, David Schlipf, and Po Wen Cheng. Prospects of linear model predictive control on a 10 mw floating wind turbine. In *International Conference on Offshore Mechanics and Arctic Engineering*, volume 56574, page V009T09A071. American Society of Mechanical Engineers, 2015. doi:10.1115/OMAE2015-42267.
- [58] Kamran Ali Shah, Ye Li, Ryoza Nagamune, Yarong Zhou, and Waheed Ur Rehman. Platform motion minimization using model predictive control of a floating offshore wind turbine. *Theoretical and Applied Mechanics Letters*, 11(5):100295, 2021. doi:https://doi.org/10.1016/j.taml.2021.100295.
- [59] Frank Lemmer, Wei Yu, Birger Luhmann, David Schlipf, and Po Wen Cheng. Multi-body modeling for concept-level floating offshore wind turbine design. *Multibody System Dynamics*, 49(2):203–236, 2020. doi:https://doi.org/10.1007/s11044-020-09729-x.

- [60] Frank Lemmer, Wei Yu, David Schlipf, and Po Wen Cheng. Robust gain scheduling baseline controller for floating offshore wind turbines. 23(1):17–30, 2020. doi:10.1002/we.2408.
- [61] Finn Gunnar Nielsen, Tor David Hanson, and Bjørn Skaare. Integrated dynamic analysis of floating offshore wind turbines. pages 671–679. ASMEDC, 2006. doi:10.1115/OMAE2006-92291.
- [62] Herbjørn Haslum, Mathias Marley, Sachin Tejawant Navalkar, Bjørn Skaare, Nico Maljaars, and Haakon S Andersen. Roll–yaw lock: Aerodynamic motion instabilities of floating offshore wind turbines. *Journal of Offshore Mechanics and Arctic Engineering*, 144(4):042002, 2022. doi:10.1115/1.4053697.
- [63] Gijs J van der Veen, Ian J Couchman, and RO Bowyer. Control of floating wind turbines. In *2012 American Control Conference (ACC)*, pages 3148–3153. IEEE, 2012. doi:10.1109/ACC.2012.6315120.
- [64] Frank Lemmer, David Schlipf, and Po Wen Cheng. Control design methods for floating wind turbines for optimal disturbance rejection. In *Journal of Physics: Conference Series*, volume 753, page 092006. IOP Publishing, 2016. doi:10.1088/1742-6596/753/9/092006.
- [65] Boris Fischer. Reducing rotor speed variations of floating wind turbines by compensation of non-minimum phase zeros. *IET Renewable Power Generation*, 7(4):413–419, 2013. doi:https://doi.org/10.1049/iet-rpg.2012.0263.
- [66] David Stockhouse, Mandar Phadnis, Aoife Henry, Nikhar J. Abbas, Michael Sinner, Manuel Pusch, and Lucy Y. Pao. A tutorial on the control of floating offshore wind turbines: Stability challenges and opportunities for power capture. *IEEE Control Systems*, 44(5):28–57, 2024. doi:10.1109/MCS.2024.3433208.
- [67] David Stockhouse, Manuel Pusch, Rick Damiani, Senu Sirmivas, and Lucy Pao. Robust multi-loop control of a floating wind turbine. *Wind Energy*, 27(11):1205–1228, 2024. doi:https://doi.org/10.1002/we.2864.
- [68] Next Ocean. WavePredictor: How Does It Work? Accessed March 30, 2025. <https://www.nextocean.nl/wavepredictor.php#>.
- [69] FLOATGEN: The first offshore wind turbine in France. Accessed April 10, 2025. <https://sem-rev.ec-nantes.fr/english-version/devices-tested/floating-offshore-wind-turbine-flotagen>.
- [70] P. Naaijen, R.R.T. van Dijk, R.H.M. Huijsmans, and A.A. El-Mouhandiz. Real time estimation of ship motions in short crested seas. In *International conference on offshore mechanics and arctic engineering*, volume 43444, pages 243–255, 2009. doi:10.1115/OMAE2009-79366.
- [71] P. Naaijen and A. P. Wijaya. Phase resolved wave prediction from synthetic radar images. In *International Conference on Offshore Mechanics and Arctic Engineering*,

- volume 8A: Ocean Engineering, page V08AT06A045. American Society of Mechanical Engineers, 2014. doi:10.1115/OMAE2014-23470.
- [72] Peter Naaijen, Karsten Truelsen, and Elise Blondel-Couprie. Limits to the extent of the spatio-temporal domain for deterministic wave prediction. *International Shipbuilding Progress*, 61(3-4):203–223, 2014. doi:10.3233/ISP-140113.
- [73] P. Naaijen, D.K. Roozen, and R.H.M. Huijsmans. Reducing operational risks by on-board phase resolved prediction of wave induced ship motions. In *International conference on offshore mechanics and arctic engineering*, volume 7: Ocean Engineering, page V007T06A013. American Society of Mechanical Engineers, 2016. doi:10.1115/OMAE2016-54591.
- [74] Peter Naaijen, Kees Van Oosten, Karel Roozen, and Riaan van't Veer. Validation of a deterministic wave and ship motion prediction system. In *International Conference on Offshore Mechanics and Arctic Engineering*, volume 7B: Ocean Engineering, page V07BT06A032. American Society of Mechanical Engineers, 2018. doi:10.1115/OMAE2018-78037.
- [75] Mees Al, Alessandro Fontanella, Daan van der Hoek, Yichao Liu, Marco Belloli, and Jan-Willem van Wingerden. Feedforward control for wave disturbance rejection on floating offshore wind turbines. In *Journal of Physics: Conference Series*, volume 1618, page 022048. IOP Publishing, 2020. doi:10.1088/1742-6596/1618/2/022048.
- [76] A. Fontanella, M. Al, J.W. van Wingerden, and M. Belloli. Model-based design of a wave-feedforward control strategy in floating wind turbines. *Wind Energy Science*, 6(3):885–901, 2021. doi:10.5194/wes-6-885-2021.
- [77] Florian Dörfler, Jeremy Coulson, and Ivan Markovsky. Bridging direct and indirect data-driven control formulations via regularizations and relaxations. *IEEE Transactions on Automatic Control*, 68(2):883–897, 2023. doi:10.1109/TAC.2022.3148374.
- [78] Rogier Dinkla, Tom Oomen, Jan-Willem van Wingerden, and Sebastiaan P. Mulders. Data-Driven LIDAR Feedforward Predictive Wind Turbine Control. In *2023 IEEE Conference on Control Technology and Applications (CCTA)*, pages 559–565, 2023. doi:10.1109/CCTA54093.2023.10252439.
- [79] Alexandra Ministeru, Amr Hegazy, and Jan-Willem van Wingerden. Data-driven wave feedforward control of floating offshore wind turbines. In *2025 American Control Conference (ACC)*, pages 1500–1507, 2025. doi:10.23919/ACC63710.2025.11108107.
- [80] Office of Aeronautics and Space Technology. Integrated Technology Plan for the Civil Space Program. Technical report, National Aeronautics and Space Administration (NASA), 1991.
- [81] Mees Al. Feedforward control for wave disturbance rejection on floating offshore wind turbines, 2020.

- [82] European Commission. EU renewable energy targets. Accessed February 05, 2023. https://energy.ec.europa.eu/topics/renewable-energy/renewable-energy-directive-targets-and-rules/renewable-energy-targets_en.
- [83] A. Hegazy, P. Naaijen, and J.W. van Wingerden. A novel control architecture for floating wind turbines. *IFAC-PapersOnLine*, 56(2):7644–7649, 2023. 22nd IFAC World Congress. doi:<https://doi.org/10.1016/j.ifacol.2023.10.1163>.
- [84] Gijs van der Veen, Jan-Willem van Wingerden, Marco Bergamasco, Marco Lovera, and Michel Verhaegen. Closed-loop subspace identification methods: an overview. *IET Control Theory & Applications*, 7(10):1339–1358, 2013. doi:<https://doi.org/10.1049/iet-cta.2012.0653>.
- [85] David Marten. Qblade. Accessed February 02, 2023. <http://www.q-blade.org>.
- [86] Christian Bak, Frederik Zahle, Robert Bitsche, Taeseong Kim, Anders Yde, Lars Christian Henriksen, Morten Hartvig Hansen, Jose Pedro Albergaria Amaral Blasques, Mac Gaunaa, and Anand Natarajan. The DTU 10-MW reference wind turbine. In *Danish wind power research*, 2013.
- [87] Vincent Arnal. *Modélisation expérimentale d’une éolienne flottante par une approche software-in-the-loop*. PhD thesis, École Centrale de Nantes, 2020. <http://www.theses.fr/2020ECDN0037>.
- [88] SOFTWIND. Accessed February 02, 2023. <https://www.weamec.fr/en/projects/softwind>.
- [89] S. Skogestad and I. Postlethwaite. *Multivariable Feedback Control: Analysis and Design*. John Wiley & Sons, 2007.
- [90] Daniel van den Berg, Delphine de Tavernier, and Jan-Willem van Wingerden. The dynamic coupling between the pulse wake mixing strategy and floating wind turbines. *Wind Energy Science*, 8(5):849–864, 2023. doi:10.5194/wes-8-849-2023.
- [91] Aitor Saenz-Aguirre, Alain Ulazia, Gabriel Ibarra-Berastegi, and Jon Saenz. Floating wind turbine energy and fatigue loads estimation according to climate period scaled wind and waves. *Energy Conversion and Management*, 271:116303, 2022. doi:<https://doi.org/10.1016/j.enconman.2022.116303>.
- [92] I.C. Kim, G. Ducrozet, F. Bonnefoy, V. Leroy, and Y. Perignon. Real-time phase-resolved ocean wave prediction in directional wave fields: Enhanced algorithm and experimental validation. *Ocean Engineering*, 276:114212, 2023. doi:<https://doi.org/10.1016/j.oceaneng.2023.114212>.
- [93] I.C. Kim, G. Ducrozet, V. Leroy, F. Bonnefoy, Y. Perignon, and S. Bourguignon. A real-time wave prediction in directional wave fields: Strategies for accurate continuous prediction in time. *Ocean Engineering*, 291:116445, 2024. doi:<https://doi.org/10.1016/j.oceaneng.2023.116445>.

- [94] I.C. Kim, G. Ducrozet, V. Leroy, F. Bonnefoy, Y. Perignon, and S. Delacroix. Numerical and experimental investigation on deterministic prediction of ocean surface wave and wave excitation force. *Applied Ocean Research*, 142:103834, 2024. doi:<https://doi.org/10.1016/j.apor.2023.103834>.
- [95] Amr Hegazy, Peter Naaijen, and Jan-Willem van Wingerden. Wave feed-forward control for large floating wind turbines. In *2023 IEEE Conference on Control Technology and Applications (CCTA)*, pages 593–598. IEEE, 2023. doi:[10.1109/CCTA54093.2023.10252529](https://doi.org/10.1109/CCTA54093.2023.10252529).
- [96] Alessandro Fontanella, Alan Facchinetti, Elio Daka, and Marco Belloli. Modeling the coupled aero-hydro-servo-dynamic response of 15 mw floating wind turbines with wind tunnel hardware in the loop. *Renewable Energy*, 219:119442, 2023. doi:<https://doi.org/10.1016/j.renene.2023.119442>.
- [97] Chaohe Chen, Yuan Ma, and Tianhui Fan. Review of model experimental methods focusing on aerodynamic simulation of floating offshore wind turbines. *Renewable and Sustainable Energy Reviews*, 157:112036, 2022. doi:<https://doi.org/10.1016/j.rser.2021.112036>.
- [98] Mohammad Rasool Mojallizadeh, Félicien Bonnefoy, Franck Plestan, Mohamed Asaad Hamida, and Jérémy Ohana. Euler implicit time-discretization of multivariable sliding-mode controllers. *ISA Transactions*, 147:140–152, 2024. doi:<https://doi.org/10.1016/j.isatra.2024.01.031>.
- [99] Mohammad Rasool Mojallizadeh, Félicien Bonnefoy, Vincent Leroy, Franck Plestan, Sylvain Delacroix, Jérémy Ohana, and Benjamin Bouscasse. Control design for thrust generators with application to wind turbine wave-tank testing: A sliding-mode control approach with euler backward time-discretization. *Control Engineering Practice*, 146:105894, 2024. doi:<https://doi.org/10.1016/j.conengprac.2024.105894>.
- [100] Félicien Bonnefoy, Vincent Leroy, Mohammad Rasool Mojallizadeh, Sylvain Delacroix, Vincent Arnal, and Jean-Christophe Gilloteaux. Multidimensional hybrid software-in-the-loop modeling approach for experimental analysis of a floating offshore wind turbine in wave tank experiments. *Ocean Engineering*, 309:118390, 2024. doi:<https://doi.org/10.1016/j.oceaneng.2024.118390>.
- [101] Sebastian Becker, Joseph Saverin, Robert Behrens de Luna, Francesco Papi, Cyril Combreau, Marie-Laure Ducasse, David Marten, and Alessandro Bianchini. Floatech d2.2. validation report of qblade-ocean. Technical report, 08 2022.
- [102] Finn Gunnar Nielsen, Tor David Hanson, and Bjørn Skaare. Integrated dynamic analysis of floating offshore wind turbines. pages 671–679. ASMEDC, 2006. doi:[10.1115/OMAE2006-92291](https://doi.org/10.1115/OMAE2006-92291).
- [103] Paul A. Fleming, Isaac Pineda, Michele Rossetti, Alan D. Wright, and Dhiraj Arora. Evaluating methods for control of an offshore floating turbine. volume 9B: Ocean Renewable Energy of *International Conference on Offshore Mechanics and Arctic Engineering*, page V09BT09A019, June 2014. doi:[10.1115/OMAE2014-24107](https://doi.org/10.1115/OMAE2014-24107).

- [104] John Nicholas Newman. *Marine hydrodynamics*. The MIT press, 2018.
- [105] William E Leithead and Sergio Dominguez. Coordinated control design for wind turbine control systems. 2006.
- [106] Boris Fischer and Peter Loepelmann. Balancing rotor speed regulation and drive train loads of floating wind turbines. In *Journal of Physics: Conference Series*, volume 753, page 052016. IOP Publishing, 2016. doi:10.1088/1742-6596/753/5/052016.
- [107] Lucy Y. Pao, Manuel Pusch, and Daniel S. Zalkind. Control co-design of wind turbines. *Annual Review of Control, Robotics, and Autonomous Systems*, 7(Volume 7, 2024):201–226, 2024. doi:https://doi.org/10.1146/annurev-control-061423-101708.
- [108] Wei Yu, Frank Lemmer, David Schlipf, Po Wen Cheng, Bart Visser, Harmen Links, Neelabh Gupta, Sabrina Dankemann, Bernardino Counago, and Jose Serna. Evaluation of control methods for floating offshore wind turbines. *Journal of Physics: Conference Series*, 1104(1):012033, Oct 2018. doi:10.1088/1742-6596/1104/1/012033.
- [109] Wei Yu, Frank Lemmer, David Schlipf, and Po Wen Cheng. Loop shaping based robust control for floating offshore wind turbines. volume 1618, page 022066. IOP Publishing, Sep 2020. doi:10.1088/1742-6596/1618/2/022066.
- [110] Paul Fleming, Jan-Willem Wingerden, and Alan Wright. *Comparing State-Space Multivariable Controls to Multi-SISO Controls for Load Reduction of Drivetrain-Coupled Modes on Wind Turbines through Field-Testing*. 2012.
- [111] Asier Diaz De Corcuera, Aron Pujana-Arrese, Jose M. Ezquerro, Edurne Seguro, and Joseba Landaluze. H_∞ based control for load mitigation in wind turbines. *Energies*, 5(4):938–967, 2012. doi:10.3390/en5040938.
- [112] NREL. National renewable energy laboratory: OpenFAST. Accessed. January 30, 2025. <https://www.nrel.gov/wind/nwtc/openfast.html>.
- [113] L. Brandetti, S. P. Mulders, Y. Liu, S. Watson, and J.W. van Wingerden. Analysis and multi-objective optimisation of wind turbine torque control strategies. *Wind Energy Science*, 8(10):1553–1573, 2023. doi:10.5194/wes-8-1553-2023.
- [114] Karl Johan Åström and Richard M Murray. *Feedback systems: an introduction for scientists and engineers*. Princeton university press, 2021.
- [115] David Stockhouse and Lucy Y. Pao. Multiloop control of floating wind turbines: Tradeoffs in performance and stability. *IEEE Control Systems*, 44(5):63–80, 2024. doi:10.1109/MCS.2024.3432340.
- [116] Tristan Perez and Thor I. Fossen. A matlab toolbox for parametric identification of radiation-force models of ships and offshore structures. 2009. doi:10.4173/mic.2009.1.1.
- [117] A. Fontanella, M. Al, D. Van Der Hoek, Y. Liu, J.W. Van Wingerden, and M. Belloli. A control-oriented wave-excited linear model for offshore floating wind turbines. *Journal of Physics: Conference Series*, 1618(2), 2020. doi:10.1088/1742-6596/1618/2/022038.

- [118] W. Cummins. The impulse response function and ship motion. Technical report, 1961.
- [119] John C. Doyle, Bruce A. Francis, and Allen R. Tannenbaum. *Feedback control theory*. Courier Corporation, 2013.
- [120] Mina Konakovic Lukovic, Yunsheng Tian, and Wojciech Matusik. Diversity-guided multi-objective bayesian optimization with batch evaluations. In H. Larochelle, M. Ranzato, R. Hadsell, M.F. Balcan, and H. Lin, editors, *Advances in Neural Information Processing Systems*, volume 33, pages 17708–17720. Curran Associates, Inc., 2020.
- [121] NREL. National renewable energy laboratory: TurbSim. Accessed January 30, 2025. <https://www.nrel.gov/wind/nwtc/turbsim.html>.
- [122] A. Hegazy, P. Naaijen, V. Leroy, F. Bonnefoy, M. R. Mojallizadeh, Y. Pérignon, and J.-W. van Wingerden. The potential of wave feedforward control for floating wind turbines: a wave tank experiment. *Wind Energy Science*, 9(8):1669–1688, 2024. doi:10.5194/wes-9-1669-2024.

Curriculum Vitæ

Amr Raafat Mohamed Hegazy

1993	Born on 8 November, 1993 Alexandria, Egypt
2010-2013	El-Nasr High School Alexandria, Egypt
2013-2018	Bachelor of Science in Mechanical Engineering Alexandria University, Alexandria, Egypt
2018-2020	Joint Master of Science in Renewable Offshore Energy Systems University of Strathclyde, Glasgow, UK University of the Basque Country, Bilbao, Spain École Centrale de Nantes, Nantes, France
2019-2020	Master of Science in Marine Technology École Centrale de Nantes, Nantes, France <i>Thesis: LiDAR and SCADA Data Processing for Interacting Wind Turbine Wakes with Comparison to Analytical Wake Models.</i> Supervisor: Prof. dr. S. Aubrun
2021-2025	Doctor of Philosophy in Systems and Control Engineering Delft University of Technology, Delft, The Netherlands <i>Thesis: Wave Feedforward and Multivariable Feedback Control Architectures and Design Methods for Floating Wind Turbines.</i> Promotor: Prof. dr. ir. J. W. van Wingerden Copromotor: Dr. ir. P. Naaijen

List of Publications

Journal publications

- 3. **A. Hegazy**, P. Naaijen, and J.W. van Wingerden: Control design of floating wind turbines, *Wind Energy Science Discussions*, doi: 10.5194/wes-2025-68, in review, 2025.
- 2. **A. Hegazy**, P. Naaijen, V. Leroy, F. Bonnefoy, M. R. Mojallizadeh, Y. Pérignon, and J.W. van Wingerden: The potential of wave feedforward control for floating wind turbines: a wave tank experiment, *Wind Energy Science*, 9:1669–1688, 2024, doi: 10.5194/wes-9-1669-2024.
- 1. **A. Hegazy**, F. Blondel, M. Cathelain, and S. Aubrun: LiDAR and SCADA data processing for interacting wind turbine wakes with comparison to analytical wake models, *Renewable Energy*, 181:457–471, 2021, doi: 10.1016/j.renene.2021.09.019

Conferences

- 6. A. Ministeru, **A. Hegazy** and J.W. van Wingerden: Data-driven Wave Feedforward Control of Floating Offshore Wind Turbines. 2025 American Control Conference (ACC), Denver, CO, USA, 2025, pp. 1500–1507, doi: 10.23919/ACC63710.2025.11108107.
- 5. **A. Hegazy**, P. Naaijen and J.W. van Wingerden: Wave Feedforward Control for Large Floating Wind Turbines. 2023 IEEE Conference on Control Technology and Applications (CCTA). Bridgetown, Barbados, 2023, pp. 593–598, doi: 10.1109/CCTA54093.2023.10252529.
- 4. **A. Hegazy**, P. Naaijen and J.W. van Wingerden: A novel control architecture for floating wind turbines. 2023 International Federation of Automatic Control (IFAC) World Congress, Yokohama, Japan, IFAC-PapersOnLine, Volume 56, Issue 2, 2023, Pages 7644–7649, ISSN 2405-8963, doi:10.1016/j.ifacol.2023.10.1163.
- 3. **A. Hegazy**, P. Naaijen and J.W. van Wingerden: Mitigation of wave disturbance on floating wind turbines. Oral presentation at the Wind Energy Science Conference 2023. Glasgow, Scotland, UK.
- 2. **A. Hegazy**, P. Naaijen and J.W. van Wingerden: Rejecting wave disturbances on floating wind turbines. Oral presentation at the Floating Offshore Wind Turbines Conference 2023. Nantes, France.
- 1. **A. Hegazy**, P. Naaijen and J.W. van Wingerden: Negative damping in floating wind turbines: an overview of solutions. Oral presentation at NAWEA/WindTech Conference 2022. Newark, Delaware, USA.

Included in this thesis.

Published in conference proceedings.

Further publications

2. **A. Hegazy**, P. Naaijen, J.W. van Wingerden: FLOATECH Deliverable 3.2: Controller development, findings and validation against numerical simulations
1. **A. Hegazy**, P. Naaijen, J.W. van Wingerden: FLOATECH Deliverable 3.1: An advanced open source wind turbine controller for power generation and load mitigation using real-time feedforward wave information.

